学位論文

Study of VLBI astrometry toward the Galactic center with VERA

(VERA による銀河系中心方向の
VLBI アストロメトリに関する研究)

平成２９年１２月博士（理学）申請

東京大学大学院理学系研究科
天文学専攻
酒井　大裕

Abstract

In this thesis, we present astrometric study of water maser sources toward the Galactic center region with the VLBI Exploration of Radio Astrometry (VERA). The central 300 pc of the Galaxy, which is called as the Central molecular zone (CMZ), has a remarkable non-circular motion compared with the Galactic disk. To explain the origin of the non-circular motion, a number of kinematic models are proposed using spectroscopic observations of interstellar medium. Proper motion measurement of a number of sources in the CMZ will enable us to constrain these models because most of models are constructed based on line-of-sight velocity observations. However, we cannot conduct astrometric observations for sufficient number of sources with the standard phase referencing observations of VLBI because position reference sources like QSOs and most of target maser sources toward the Galactic center are weak so that we cannot detect those signal within a short coherent time of about 1 minute. On the other hand, we have to measure the parallaxes of these target sources as well as the proper motions because the confusion of nearby foreground sources located along the same line-of-sight to the Galactic center is also problematic. We overviewed the problems in understanding the kinematics of the CMZ, and basic theories of interferometer and data reduction of VLBI in Chapter 1 and 2.

In Chapter 3, we developed a new observation technique, the triangle phase referencing observations, which enable us to detect weak maser sources which cannot be detected by the standard phase referencing technique. The triangle phase referencing uses a strong phase reference maser (PRM) in addition to a position reference QSO (PRQ) and a target maser (TM) of which we want to obtain the parallax and proper motion. We conducted test observations of the triangle phase referencing for W3OH region to evaluate the accuracy of the astrometric results obtained by the triangle phase referencing technique. As a result, we obtained the systematic position error in the triangle phase referencing technique of 37 μas. This was smaller than the position error caused by the thermal noise (38–95 μas). Parallax and proper motion fitting also indicated that the fitted values of the parallax and proper motions obtained by the triangle phase referencing were consistent with those by the normal phase referencing within errors. Thus, the triangle phase referencing can be applied without a significant error increase. It makes possible to measure the proper motions and to distinguish between nearby sources and the Galactic center sources by parallax measurement.

Chapter 4 and 5 show astrometric observations for water maser sources associated with the Sgr D HII region and the Sgr B2 complex, respectively. These two sources have relatively strong flux densities toward the Galactic center region, and the triangle phase referencing is not required. We obtained the parallax of the Sgr D to be $\pi = 0.423 \pm 0.083$ mas, corresponding to $d = 2.36^{+0.58}_{-0.39}$ kpc. Our results are the first accurate distance measurement of the Sgr D HII region, suggesting that the Sgr D HII region is located at the foreground of the Galactic center and the Scutum arm of the Galaxy. For the Sgr B2 complex, we measured detailed three dimentional motions of water masers associated with Sgr B2M, N, and S in the Sgr B2 complex for the first time. Our results of the parallax and proper motions, $\pi = 0.133 \pm 0.038$ mas and $(\mu_l \cos b, \mu_b) = (-3.72 \pm 0.22, -0.49 \pm 0.23)$ mas/yr prefer open-orbit model of the CMZ although the predicted proper motions for the open-orbit at this position contain large errors.

In Chapter 6, we conduct the triangle phase referencing observations for two weak maser sources toward the Galactic center region. As a phase reference maser (PRM), we used a strong maser spot in Sgr B2M. The target masers are water maser sources associated with G359.94-00.14 and G000.16-00.44. G359.94-00.14 is a Young stellar object (YSO) located at very vicinity of Sgr A* in the projection, and G000.16-00.44 is a star-forming region. Both of water maser sources are so weak that we cannot detect the maser spot with the standard phase referencing technique. Using the triangle phase referencing, we succeeded to detect maser spots, and to measure their absolute positions. For G000.16-00.44, we measured the parallax and proper motions as $\pi = 0.645 \pm 0.074$ mas, $(\mu_l \cos b, \mu_b) = (-0.51 \pm 0.13, -0.77 \pm 0.15)$ mas/yr, and it suggested that G000.16-00.44 is located at the Sagittarius arm. For G359.94-00.14, unfortunately, the flux of the maser source decreased under the detection limit of the triangle phase referencing (< 1 Jy) after mid 2016. The parallax for G000.16-00.44 can be measured for the first time by detecting weak maser spots using the triangle phase referencing.

In summary, we developed a new phase referencing technique, the triangle phase referencing, to measure parallaxes and proper motions for weaker maser sources which could not be detected by the standard phase referencing toward the Galactic center. The new technique successfully detected weak maser sources down to about 1 Jy. This enabled us to increase the number of sources for which we can conduct astrometric observations with VLBI, and to distinguish between the nearby and the Galactic center sources located at the same line-of-sight direction. Our works in this thesis demonstrate that the future VLBI observations toward the Galactic center enable us to constrain the kinematics model of the CMZ.

Contents

Chapter 1 General introduction

1.1 The review of the dynamics of the Galactic center region

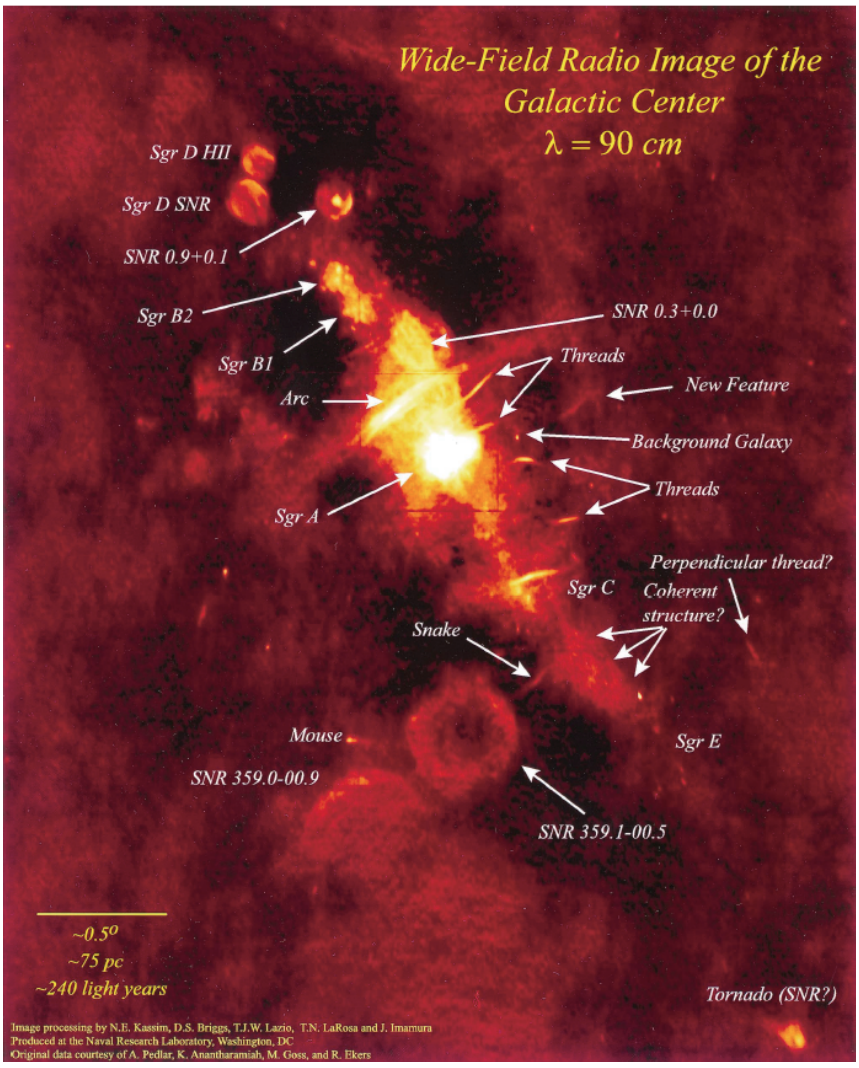

Figure 1.1: Radio continuum image of the Galactic center region (Figure 1 of Larosa et al. 2000)

The relationship between the central massive black hole and the overall structure of the hosting galaxy is a key subject to be revealed. Especially, how central black holes are fed in the forming period of galaxies and how the activities of these black holes affect the outer part of galaxies are important to understand the galaxy formation.

In this point of view, it is important to investigate the environment of the molecular component in central parts of galaxies because the central a few hundred parsec of galaxies contains a plenty of molecular clouds of approximately $10\,M_\odot$ and has complex kinematics losing the angular momentum to transport them inward (Morris & Serabyn 1996). Our Galaxy is the most suitable candidate to investigate its central region because we are inside the Galaxy. We can obtain the larger information for the center of our Galaxy with the higher spatial resolution thanks to its proximity.

1.1.1 Central molecular zone

Our Galaxy is a barred spiral galaxy. In the outer part of the Galaxy ($R > 5\,\mathrm{kpc}$), the interstellar medium associated with the spiral structure moving along the circle loci relative to the center of the Galaxy . However, the inner part of the Galaxy ($R < 5\,\mathrm{kpc}$) is known to be relatively large velocity displacement from the circular rotation (Morris & Serabyn 1996). This non-circular motion is discovered by the line-of-sight velocity distribution of the molecular cloud observed in the ^{13}CO $J = 1$–0 and CS $J = 2$–1 lines (Bally et al. 1987).

Especially, the central 300 pc of the Galaxy, which is called as the Central molecular zone (hereafter CMZ), has a remarkable non-circular motion compared with the Galactic disk. In the CMZ, the density of molecular gas is high ($n > 10^4\,\mathrm{cm}^{-3}$), and its mass is $5 \times 10^7\,M_\odot$ (Bally et al. 1987, Tsuboi et al. 1989). The temperature of the molecular cloud in CMZ is 50–400 K, which is relatively higher than the typical temperature in the Galactic disk of 10–20 K (Morris et al. 1983, Mills & Morris 2013). The velocity dispersions ($\sim$ 15–50 $\mathrm{km\,s}^{-1}$) is also large, and this high velocity dispersion could be responsible for gas heating (Wilson et al. 1982). The star formation activity in the CMZ is suppressed relative to the Galactic disk because there are unusually strong tidal fields which can overcome a self-gravity of a collapsing gas (Güsten & Downes 1980).

Figure 1.1 is the radio continuum image of the CMZ observed with the VLA at 90 cm wavelength (Larosa et al. 2000). The most intense part on the center of the image is Sgr A, which contains a super massive blackhole (SMBH) with the mass of about $4 \times 10^6\,M_\odot$ (Scho"odel et al. 2002). The plane of the Galaxy ranges from top-left to bottom-right of the image. There are a lot of peculiar radio sources along the disk. Sgr B2 and Sgr C are known as massive star-forming regions in the CMZ region, and they suffer strong shocks

which trigger the formation of massive molecular clouds. This shock focusing mechanism is suggested by Kenney & Lord (1991) for M83. Filament-like structures referred as "Threads" are thought to be emitted by synchrotron radiation due to strong magnetic field generated at the surfaces of dense molecular clumps moving through a diffuse ambient medium (Morris & Serabyn 1996; Yusef-Zadeh 2003). It is difficult to measure the distance to these Galactic center sources even whether these are located in the Galactic center because dynamical distance using line-of-sight velocities could not be precisely obtained toward the Galactic longitude of $l \sim 0°$.

1.1.2 The origin of the non-circular motion in the Galactic center

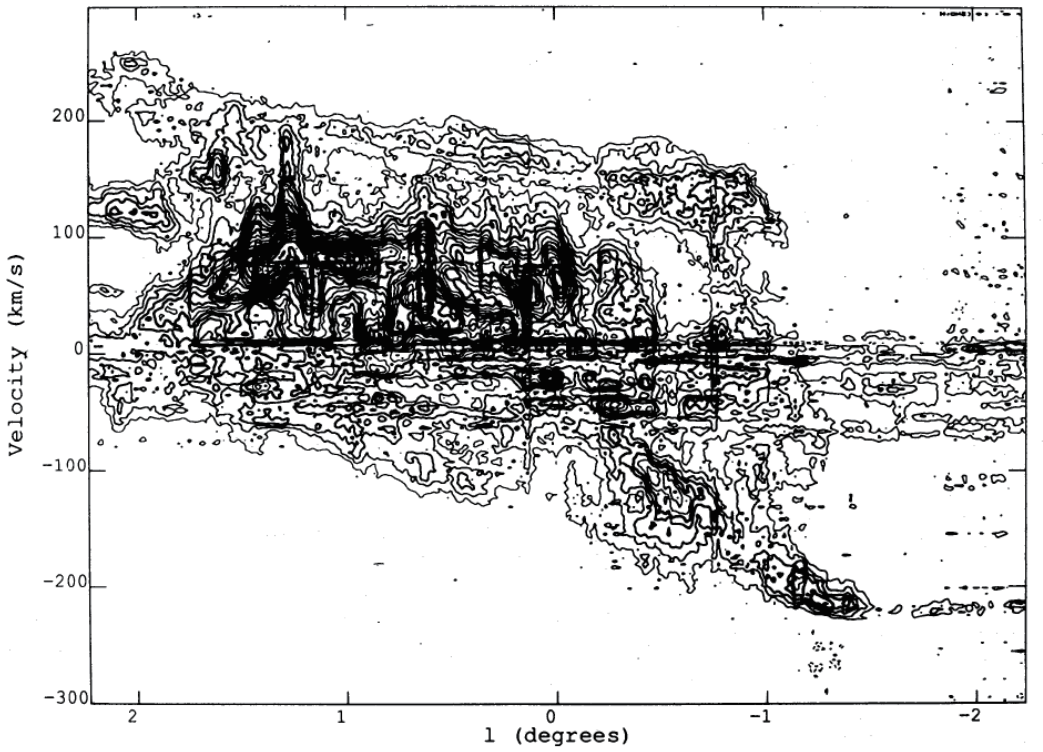

Figure 1.2: (l, v) diagram of the ^{12}CO $J = 1$–0 averaged in b over the range $|b| < 0.1°$. Figure 2 of Binney et al. (1991).

The dynamical environment of the CMZ is significantly different from that of the Galactic disk region which trace almost circular loci around the center of the Galaxy. Figure 1.2 shows the $l - v$ diagram of the ^{12}CO $J = 1$–0 within 2 degrees of the galactic longitude presented in Binney et al. (1991). The molecular line emission in this region distributes in terms of a parallelogram slightly shifted to positive l and v whose vertices are located at

$(l, v) = (1.8°, 200\,\mathrm{km\,s^{-1}}), (1.8°, -40\,\mathrm{km\,s^{-1}}), (-1.1°, -200\,\mathrm{km\,s^{-1}}), (-0.8°, 140\,\mathrm{km\,s^{-1}})$. If its orbit is a circularly rotating ring, the (l, v) diagram should become a linear line through $0\,\mathrm{km\,s^{-1}}$ which ends at the velocity of rotation. Thus, Figure 1.2 clearly indicates that the orbit and motion of molecular gas in the CMZ different from those of a circular ring with a constant velocity of rotation.

The origin of the non-circular motion as well as the accurate motion of the gas in the Galactic center region is one of the major open questions in the field of astronomy, because it directly relates to feeding SMBHs through the gas losing angular momentum and moving inward (Morris & Serabyn 1996).

Historically, a number of scenarios which can explain observational fact were proposed. In this part, we introduce some major candidates of dynamical scenarios proposed by observations from radio to X-ray.

Expanding ring model

In early 1970s, the expanding ring model was proposed to explain the line-of-sight velocity structure observed by the molecular line observations (Kaifu et al. 1972, Scoville 1972). They suggested that non-circular motion of the CMZ was originated from the expansion event which has occurred about 10^7 to 10^8 years ago. This expanding ring shows a shape of an 'ellipse' in the (l, v) diagram. They fitted the velocities of expansion and rotation to the (l, v) diagram of OH 1667 MHz absorption, and obtained $V_{\mathrm{ex}} = 130 \pm 5\,\mathrm{km\,s^{-1}}$, $V_{\mathrm{rot}} = 50 \pm 20\,\mathrm{km\,s^{-1}}$, and $R = 270 \pm 30\,\mathrm{pc}$. V_{ex}, V_{rot}, and R are the velocities of expansion and rotation, and the radius of the ring, respectively. Sofue (1995) extended this expanding ring model to expanding shell from the vertical extent detected by ^{13}CO $J = 1$–0 observations. In their model, the shell has vertical extent of $\sim 50\,\mathrm{pc}$, and the thickness of $\sim 15\,\mathrm{pc}$. They estimated that coherent star formation containing 10^3 super novae explosions occurred for a short period in the past $\sim 10^6\,\mathrm{yr}$.

The weakness of this scenario is that the extreme high energy being order of $\sim 10^{55}\,\mathrm{erg}$ is required to explain this ring. However, we have to point out that the recent discovery of *Fermi* bubbles require a similar energy of $E \sim 10^{55}\,\mathrm{erg}$ on a similar time scale of $\sim 10^7\,\mathrm{yr}$ ago if it is originated from Sgr A*.

Recent X-ray observations with *Suzaku* satellite discovered the X-ray reflection nebula emission (XRNE) toward giant molecular clouds in the Galactic center region. This emission consists of a fluorescence line of neutral and low-ionised iron at 6.4 keV (Fe K)from molecular cloud irradiated by external X-rays (Koyama et al. 2007, Ryu et al. 2009). In this decades, *Suzaku*, *XMM-Newton* and *Chandra* detected the XRNEs from Sgr B2 (Terrier et al. 2010,

Nobukawa et al. 2011), Sgr C (Ryu et al. 2013, Chuard et al. 2017), and the Sgr A complex (Ponti et al. 2010). The origin of the external emission irradiating the molecular cloud is interpreted as the past large flare of Sgr A*. This large flare has occurred a few hundred years ago. This fact also suggests that Sgr A* had high activity at least a few hundred years ago. The concept of the XRNE is illustrated on Figure 1.3 (Nobukawa et al. 2011)

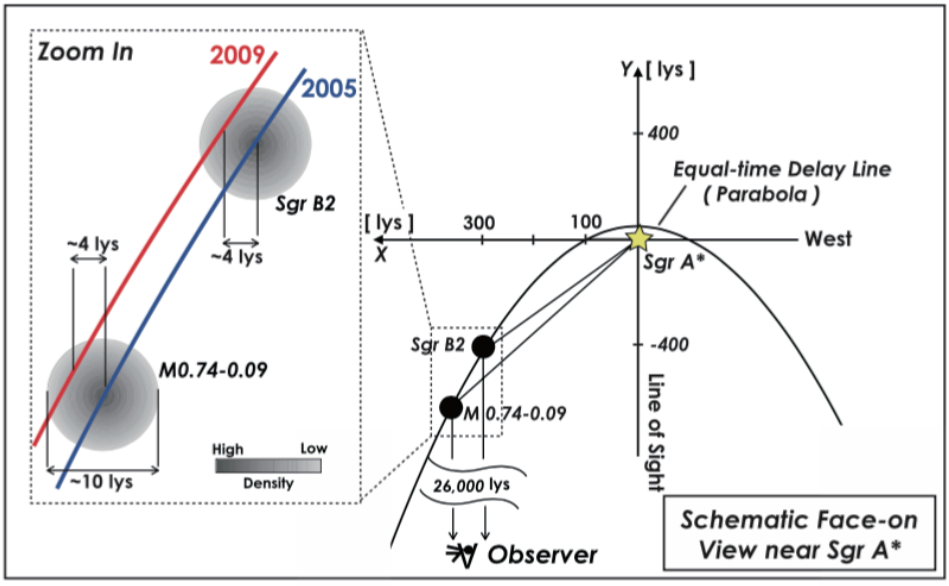

Figure 1.3: Schematic view of XRNE in the direction of the Sgr B region (Figure 3 of Nobukawa et al. 2011).

Resonance orbit model

One of the most accepted scenario of the origin of the non-circular motions is that the molecular clouds in the inner part of the Galaxy suffer the effect of the potential produced by the bar structure of the Galaxy. This scenario is first proposed by Binney et al. (1991), and this model well reproduced the line-of-sight features obtained by molecular line observations (Fig 1.2; Bally et al. 1988).

They reproduced the model orbits of molecular gas by assuming that the orbits are in terms of closed orbits. This assumption was set from an idea that gas clouds in a potential settle onto closed orbits because these clouds collide with each other and dissipate their energy (Schwarzschild 1979, Binney et al. 1991). This scenario suggested that molecular clouds in the CMZ are associated with the inner Lindblad resonance orbit produced from the bar potential of the Galaxy (Contopoulos and Mertzanides 1977). Its orbit model of

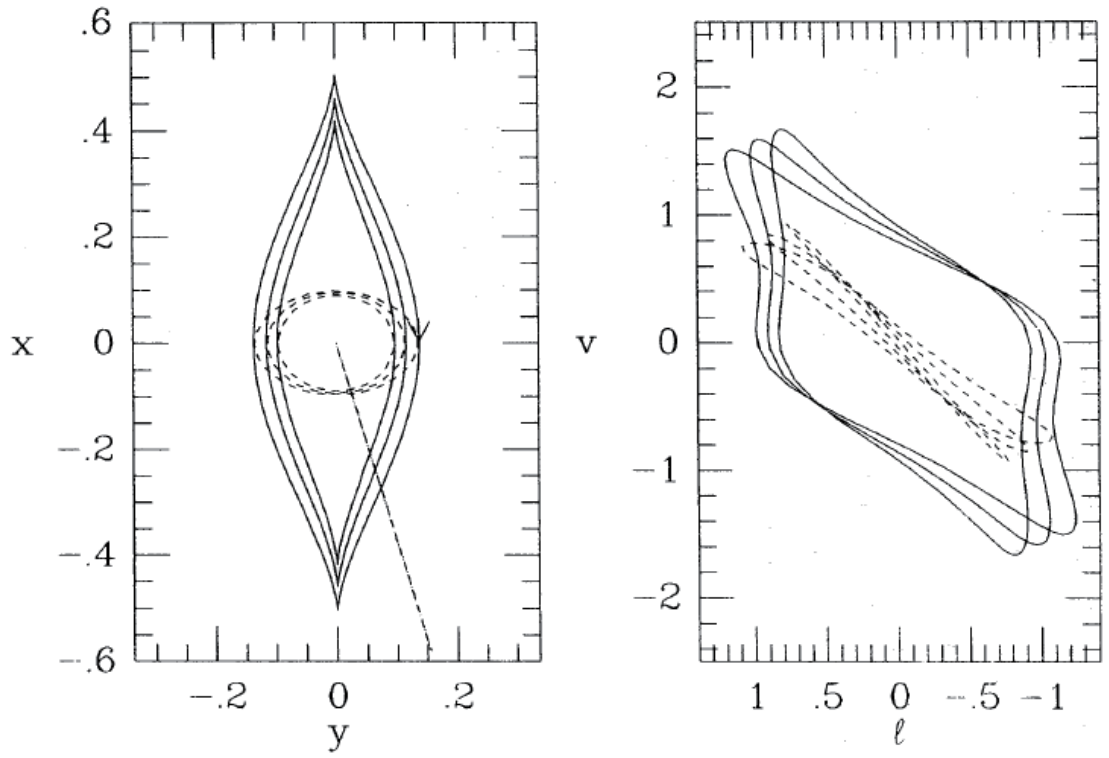

Figure 1.4: (Left) Face-on view and (Right) (l, v) diagram of the modeled orbits by Binney et al. (1991). The solid line and dotted line represent outer x_1 orbits and inner x_2 orbits, respectively. Tye dashed line in the left figure indicates the direction of the observers. Figure 3 of Binney et al. (1991).

molecular gas is shown in Figure 1.4. These orbits consist of outer x_1 orbits and inner x_2 orbits. The model orbits were calculated in a potential

$$\Phi = \frac{1}{2} v_0^2 \ln(x^2 + y^2/q^2). \quad (1.1)$$

Here, v_0 is the circular rotation speed, and q is a parameter which determines the elongation of the potential. On this decades, this model has been modified by several papers as the quality improvement of the observation data. Sawada et al. (2004) derived the relative position of giant molecular clouds in the CMZ using the ratio of OH absorption and CO emission. They suggested that CMZ is elongated, and that the eastern side of the CMZ is closer to us. Molinari et al. (2011) proposed the twisted ring model by using the infrared observations with *Herschel* and molecular line data to extract the radial velocities of the clouds by Tsuboi et al. (1999). Their model is assuming that the molecular gas in the CMZ is orbiting along ∞-shaped elliptical orbit with a constant orbital speed $v_{\rm orb}$. As parameters

of elliptical orbit, they set semi-axis $[a, b]$, major-axis position angle θ_p, and a vertical frequency ν_z and phase θ_z for vertical oscillation components. Using these parameters, they modeled the position and radial velocity of each point along the orbit as a function of the polar angle θ_t as

$$\begin{cases} x &= a\cos\theta_t\cos\theta_p - b\sin\theta_t\sin\theta_p \\ y &= a\cos\theta_t\sin\theta_p + b\sin\theta_t\cos\theta_p \\ z &= z_0\sin\nu_z(\theta_p - \theta_z) \\ v_r &= -v_{\rm orb}\cos(\theta_p + \theta_t). \end{cases}$$

In their model, average position in vertical axis z_0 is fixed to 15 pc. The frequency in vertical oscillation is also fixed to $\nu_z = 2$. The best fit parameters are a half major axis $a = 100$ pc, a half minor axis $b = 60$ pc position angle of a minor axis between line-of-sight $\theta_p = 40$ pc, and orbital velocity $v_{\rm orb} = 80\,{\rm km\,s^{-1}}$. They obtained $\theta_z \sim 0$ which indicated that the ring crosses the mid-plane along X-axis.

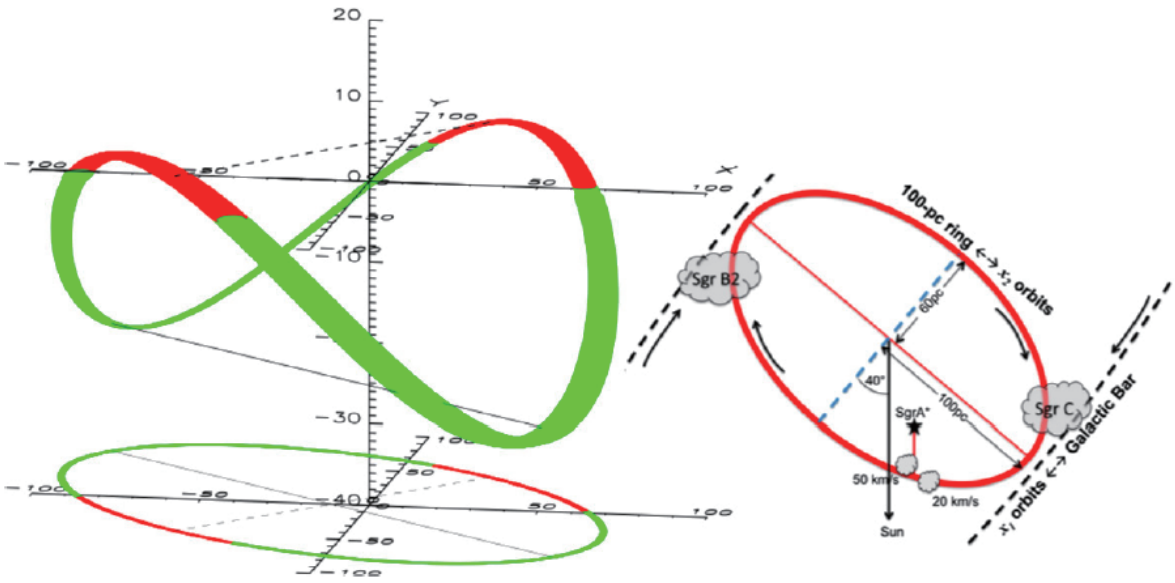

Figure 1.5: Sketch of the proposed three-dimensional structure and placement of the 100 pc ring. Left: the ring is represented by the color line. The line-of-sight to the Sun is along the Y-axis. Right: top view of the ring. The thick black dashed lines represent the innermost x_1 orbits. Figure 5 of Molinari et al. (2011).

Recently, Kruijssen et al. (2015) presented a new orbital model by assuming a open-orbit unlike the closed-orbit suggested by Molinari et al. (2011). They considered there is

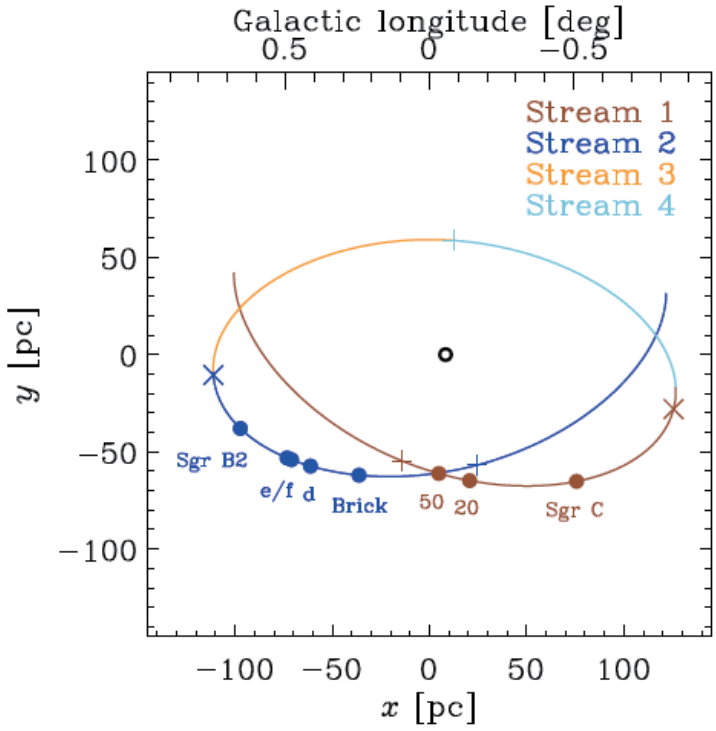

Figure 1.6: Top-down view of the open-orbit model. The observer is located in the negative-y direction. The colors represent the four coherent streams seen in the (l, v) diagram. The plus and cross symbols indicate pericenters and apocenters, respectively. The open black circle denotes the position of Sgr A*. Figure 6 of Kruijssen et al. (2014).

no evidence that the orbit is closed on scale as small as 100 pc, because the mass distribution in the CMZ is extended. Their model adopted a gravitational potential presented by Launhardt et al. (2002). Figure 1.6 shows face-on view of their model. The orbital velocity is changed by the phase of the orbit while the constant velocity is assumed in Molinari et al. (2011). Then, they obtained the orbital velocity at the pericenter is $207\,\mathrm{km\,s^{-1}}$, and the velocity at the apocenter is $101\,\mathrm{km\,s^{-1}}$. These velocities are much higher than the orbital velocity obtained by Molinari et al. (2011) ($v_{\mathrm{orb}} = 80\,\mathrm{km\,s^{-1}}$).

1.2 The basic of trigonometric parallax

When the earth rotates around the Sun with the period of one year, sources at relatively near distances move with respect to background source such as QSOs whose distances are quite far. The amplitude of the motion is larger for sources whose distance is small, and is

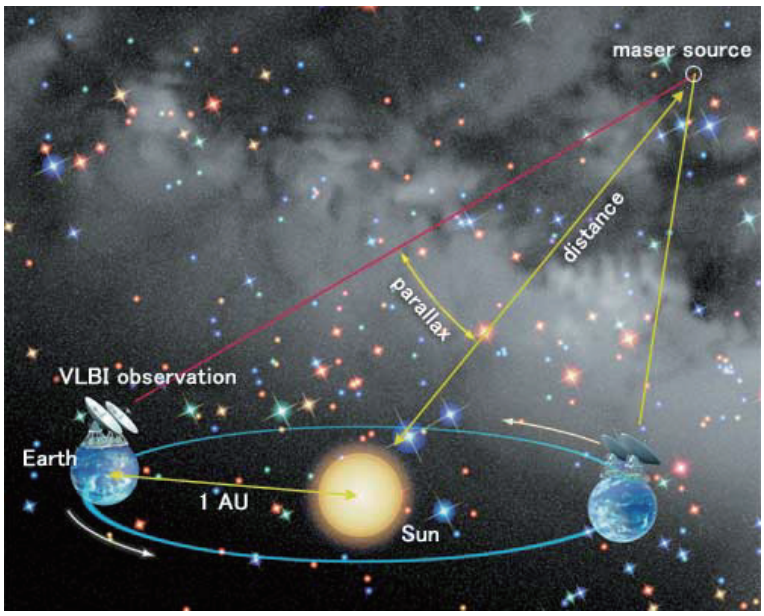

Figure 1.7: Schematic picture of the parallax measurement with VLBI observations. (http://veraserver.mtk.nao.ac.jp)

defined as the parallax π. Then, the distance D is obtained as

$$D\,[\mathrm{pc}] = \frac{1}{\pi\,[\mathrm{arcsec}]} \qquad (1.2)$$

This is called as trigonometric parallax, and this is the most robust method to measure distances in the filed of astrophysics because the parallax measurement needs no assumptions. However, measuring parallax is very difficult because its value is very small. For example, the parallax amplitude for a source whose distance is 1 kpc corresponds to 1 milli-arcsecond (mas) from the equation above. *Hipparcos* satellite has measured a number of trigonometric parallaxes of stars around the Sun. It achieved an accuracy of $\sim 10\%$ at the distance of about 100 pc (Perryman et al. 1995).

When we aim to measure the accurate distance up to the Galactic center region whose distance is about 8 kpc, parallaxes of sources at the distance are 0.125 mas. VLBI (Very Long Baseline Interferometry) is the best tool to measure the parallax due to very high angular resolution. Figure 1.7 illustrates the concept of the trigonometric parallax measurement.

1.3 22 GHz water maser

In thermal equilibrium state, energy state of interstellar particles are given by the Bolzmann relation.

$$n(\mathcal{E}) = n_0 e^{-\mathcal{E}/kT}. \quad (1.3)$$

If the number of particles in the upper state exceed that in the lower state, this is called a population inversion, the probability of stimulated emission overcomes that of absorption. Thus, the radiation from stimulated emission induces another radiation, and is dramatically amplified. In this situation, the absorption coefficient α_ν has a negative value. Then, the optical depth defined as

$$\tau_\nu(s) = \int_{s_0}^{s} \alpha_\nu(s')\,\mathrm{d}s' \quad (1.4)$$

also becomes negative. Thus, when we consider the radiative transfer equation (Rybicki & Lightman 1979)

$$I_\nu(\tau_\nu) = S_\nu + e^{-\tau_\nu}(I_\nu(0) - S_\nu), \quad (1.5)$$

the incident emission $I_\nu(0)$ is exponentially amplified by $e^{-\tau_\nu}$. S_ν is defined as

$$S_\nu \equiv \frac{j_\nu}{\alpha_\nu}, \quad (1.6)$$

where j_ν is the emission coefficient which has a positive value. Thus, S_ν is also negative.

This sort of radiation process in radio wavelength is referred as *maser* (Microwave Amplification by Stimulated Emission of Radiation). Similar emission mechanism operated at optical is called a *laser*. A remarkable feature of maser is a coherency because the emitted photons have the same characteristics as the stimulating photons.

There are several pumping mechanisms to create a population of inversion. Radiational pumping and collisional pumping are the major candidates. If there are very energetic photons, the photons excite particles into higher state. Then, the population of states gets inverse. Similarly, when a molecule is formed in the collision of atoms, that molecule is formed with a high energy state.

H_2O masers at 22 GHz were observed at star-forming region in the Galaxy. These masers are thought to be excited by collisional pumping, and associated with outflows emitted from young stellar objects (YSOs) in the star-forming region.

The 22 GHz H_2O maser is suitable as an object for astrometric observation because (1) the maser emission is significantly intense and (2) the emission is quite compact and point-like.

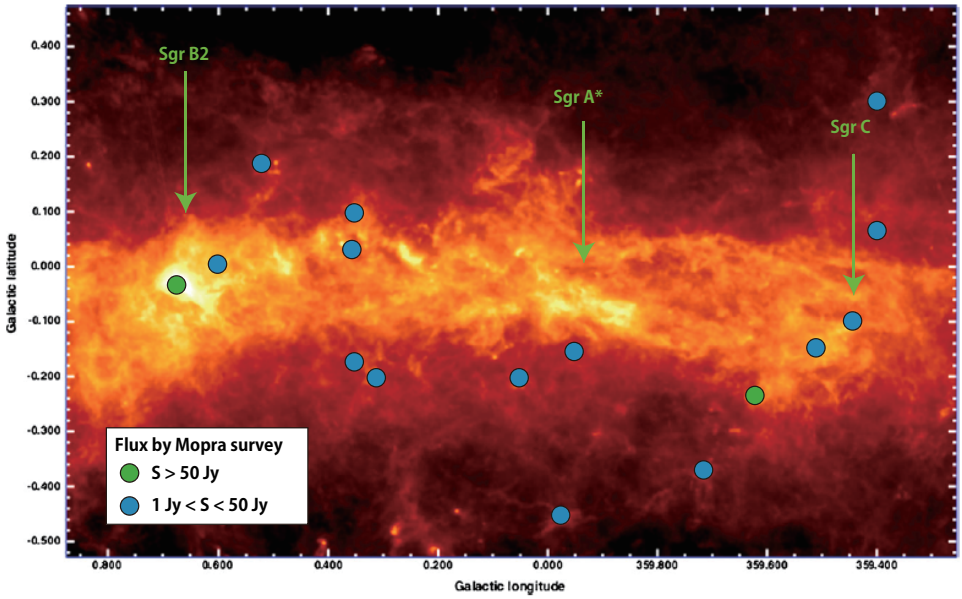

Figure 1.8: The distribution of 22 GHz water maser sources in the Galactic center region superposed on *Herschel* SPIRE 250 μm image (Molinari et al. 2011). Green filled-circle is strong ($S > 50\,\mathrm{Jy}$), and blue filled-circle is relatively weak ($1\,\mathrm{Jy} < S < 50\,\mathrm{Jy}$).

1.4 Water maser survey in the Galactic center region

A survey of 22 GHz water maser sources toward the Galactic center is conducted with Mopra 22-m telescope in Australia (Walsh et al. 2011). They detected 16 water masers within $-1^\circ < l < 1^\circ$. In their survey, G0.67-0.04 (Sgr B2) and G359.62-0.25 have large flux density ($> 50\,\mathrm{Jy}$), while other 14 sources have moderate flux ($1\,\mathrm{Jy} < S < 50\,\mathrm{Jy}$). The positions of the maser sources are presented on Figure 1.8 superposed on *Herschel* SPIRE 250 μm image (Molinari et al. 2011).

Caswell et al. (2011) also made a water maser survey within $-0.5^\circ < l < 0.5^\circ$ region in the Galactic center with the ATCA array. Then, they detected 27 maser sources in this region. Most of these sources have flux around 1 Jy. Note that the fluxes of some maser sources detected in ATCA survey are different from those in Mopra survey. The reason should be that the fluxes vary between these two observations due to the short life-time of the 22 GHz water masers. For example, G0.38+0.03 has 31.8 Jy with Mopra survey while this source has 3.3 Jy with ATCA survey.

1.5 Astrometric observations in the Galactic center

As described in Chapter 1.1, revealing the complete orbit of the CMZ is important to understand the physical property of the Galactic center region as well as property of SMBH in the center of the CMZ. To explain this, a number of orbital models and dynamical scenarios are proposed by a number of authors. However, most of these studies described are based on the information of line-of-sight velocities obtained by spectroscopic observations of interstellar medium. Such one dimension velocity information cannot distinguish these different models properly because all models can be fitted to (l, v) diagram of spectral line emission in a certain degree.

Thus, proper motion measurement of the molecular clouds can directly constrain these previous models by obtain the information of three dimensional velocity. For example, the difference of proper motion between the expanding ring model and the resonance orbit scale at 200 pc scale appears remarkably at the tangental point of the CMZ with the line-of-sight direction ($l \sim \pm 1^\circ$). This is because the expanding ring model has large proper motion of $\sim 130\,\mathrm{km\,s^{-1}}$ at that point due to the expanding component while the resonance orbit model doesn't have such large proper motions since we see the tangential point of the orbit at $l \sim \pm 1^\circ$. On the other hand, we will see the difference between the closed orbit model by Binney et al. (1991) and Molinari et al. (2011) and the open orbit model by Kruijssen et al. (2015) by measuring sufficient number of proper motions at $l \sim 0$ because the closed orbit has the proper motion of about $\pm 80\,\mathrm{km\,s^{-1}}$ at this direction while the open orbit has about $\pm 200\,\mathrm{km\,s^{-1}}$ as the proper motion.

Thanks to the high accuracy of astrometric observation with VLBI, now we are ready to measure proper motions of astronomical masers associated with molecular clouds if appropriate requirements for astrometric observations are satisfied. However, there are kinds of difficulties to measure the parallax and proper motions accurately. First, no strong position reference QSO exists toward the CMZ. In VERA observations, required flux density of the QSO is more than about 100 mJy at 22 GHz band observations when we conduct normal phase referencing observations (Chapter 2.3). On the other hand, if we use another phase referencing technique which is referred as inverse phase-referencing, the required flux density falls into 10–30 mJy (Imai et al. 2012). With this condition, there are some candidates of position reference QSO. However, the flux density of maser source for which we want to measure the parallax and proper motions has to be enough strong to obtain sufficient fringe solutions within short integration time of ~ 1 min. Typically, the maser source has to be stronger than the flux density of 10 Jy to conduct the inverse phase referencing observations. In Chapter 2.4, we introduce this method in detail.

From this reason, we conduct inverse phase referencing observations to measure the parallax and proper motions toward maser sources in the Galactic center region. Then, second difficulty is the small number of maser sources whose flux density is more than 10 Jy. Although a water maser survey using single-dish telescope detected tens of maser sources toward the CMZ (Walsh et al. 2011), most of detected sources are not enough strong to conduct inverse phase referencing observations except for a few sources such as Sgr B2. Thus, a new phase referencing technique is required to overcome these limitations of intensity.

From earlier sections, the main problems to conduct proper motion measurements for the CMZ is follows :

- We can conduct astrometric observations toward the Galactic center only for strong 22 GHz water maser sources whose flux density is over 10 Jy by using standard phase referencing technique with VERA. The number of sources satisfying that flux is limited (Sgr B2, Sgr D, and a few other sources).

- Proper motions for weaker sources less than 10 Jy is required to constrain the kinematic model of the CMZ. It is necessary to develop a new phase referencing technique to overcome such a limitation of the flux density.

1.6 Purpose of this thesis

Although there are tens of water maser sources toward the Galactic center, we don't know whether these masers are actually located at the CMZ or located at the Galactic disk. In this thesis, we aim to measure the parallaxes and proper motions of several maser sources and to distinguish the sources in the Galactic center or not. This can be regarded as a step before constraining the models of the CMZ by observing a number of proper motions in the Galactic center.

We introduce the basic theory of interferometer and the technique of astrometric observations using VLBI in Chapter 2. In Chapter 3, we present the development of a new observation technique using a strong reference maser to obtain the parallaxes and proper motions for weak maser sources which cannot be detected using the standard phase referencing technique. Also, we conducted test observations to evaluate the accuracy of astrometric results obtained by this new technique for W3OH region. Chapter 4 and 5 show the astrometric results for water maser sources associated with Sgr D and Sgr B2. These two sources can be detected using the inverse phase referencing technique because they are strong enough to detect their emission within the short coherence time of about 1 minute

which is explained in Chapter 2 and 3. In Chapter 6, finally, we conducted astrometric observations for two weak maser sources toward the Galactic center using our new observation technique introduced on Chapter 3.

Chapter 2 Instruments and methods

2.1 The principle of interferometer

In this section, we summarize the principle of interferometer based on Thompson, Moran, and Swenson (2017; 3rd edition). Radio interferometers are ensembles of antennas pairs. The most remarkable property of interferometers is the high angular resolution. This enables us to investigate detail structures of sources and to measure accurate positions and annual parallaxes.

Figure 2.1 illustrates the geometry of an interferometer. Radiation from a radio source arrives at two antennas with a time lag of τ_g. τ_g is referred as the geometric delay. In observations of the interferometer, the measured signals at each antenna are processed at the correlator. If the signal voltages for antenna 1 and 2 are V_1 and V_2, the output from the correlator can be described as :

$$C(\tau) = \frac{1}{2T}\int_{-T}^{T} V_1(t-\tau_i)V_2(t-\tau_g)\,\mathrm{d}t. \qquad (2.1)$$

Here, 2T is the integration time for each data, typically the order of seconds. τ_i is the artificial delay inserted into an antenna to correct the geometric delay to be zero. τ is the time delay of the received signals between antennas. This contains various contributions of delays from such as atmosphere and ionosphere as well as the geometric delay. When an array which has a baseline vector $\boldsymbol{D}$ observes a source toward the direction of $\mathbf{s}$, the geometric delay τ_g between the two antennas is obtained as :

$$\tau_g = \frac{\boldsymbol{D}\cdot\boldsymbol{s}}{c}. \qquad (2.2)$$

The Fourier transform of $C(\tau)$ about τ becomes $\hat{C}(\nu)$, which is called a cross power spectrum. When $I(\nu, l) = V^2(\nu, l)$, the cross power spectrum has the relationship :

$$\hat{C}(\nu) = \int_{-\infty}^{\infty} \mathrm{d}l\,\mathrm{d}m\, I(l.m)\exp(2\pi i(ul+vm)) \qquad (2.3)$$

This is identical to the visibility $\mathcal{V}(u, v)$. Here, (u, v) is defined as $u = \frac{D_x}{\lambda}$ and $v = \frac{D_y}{\lambda}$, and referred as the spatial frequency. D_x and D_y are the components of the baseline vector to the direction of east-west and north-south, respectively. λ is the observational frequency. Two dimension intensity distribution $I(l, m)$ obtained from the observation of an interferometer

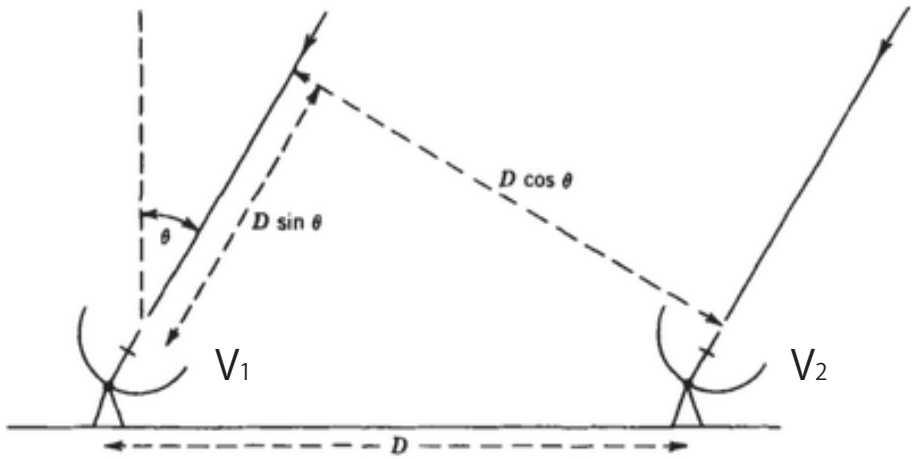

Figure 2.1: Geometry of an elementary interferometer (Figure 2.1 of Thompson, Moran, and Swenson 2017)

can be calculated from $\mathcal{V}(u,v)$ by two dimensional Fourier transform about (u,v) and (l,m).

$$I(l,m) = \int_{\infty}^{\infty}\int_{-\infty}^{\infty} \mathrm{d}u\,\mathrm{d}v\,\mathcal{V}(u,v)\exp(2\pi i(ul+vm)), \quad (2.4)$$

where l and m are the dimension of spatial angle. From the characteristic of Fourier transform, the large spatial frequencies u and v correspond to the small spatial scales. Thus, the longer the baseline length D is, the finer image we can obtain. The spatial resolution of the interferometer, $\Delta\theta$, can be defined as the width of half maximum (FWHM) of the synthesized beam. For simplicity, when we suppose a uv-coverage

$$\begin{aligned} \mathcal{V}(u,v) &= 1 \text{ for } |u| < u_{\max}\, |v| < v_{\max} \quad (2.5)\\ &= 0 \text{ for others,} \end{aligned}$$

the synthesized beam size becomes

$$\begin{aligned} B(l,m) &= \frac{1}{4u_{\max}v_{\max}}\int_{-u_{\max}}^{u_{\max}}\int_{-v_{\max}}^{v_{\max}} \mathrm{d}u\,\mathrm{d}v\exp(2\pi i(ul+vm)) \quad (2.6)\\ &= \frac{\sin 2\pi u_{\max}l}{2\pi u_{\max}l}\frac{\sin 2\pi v_{\max}m}{2\pi v_{\max}m}. \end{aligned}$$

This function is a two-dimension Sinc function, whose FWHM is approximately $1/u_{\max}$, $1/v_{\max}$. Therefore, the angular resolution for interferometer is provided as

$$\Delta\theta \sim 1/u_{\max} = \lambda/D. \quad (2.7)$$

VLBI (Very Long Baseline interferometry) is a technique of interferometry in which the antenna elements are separated by large distance. The basic principles involved in VLBI

are the same as interferometers with connected elements whose baselines are relatively short (less than 1,000 km). In the VLBI observations, the data is recorded at each station, and delivered to central correlator. Since independent frequency standards and clocks are used at each antenna station, instrumental timing errors exist in each data delivered from the antenna stations. Thus, two-dimensional search in delay and fringe rate is required to find the peak of the correlation function. This is referred as fringe fitting.

The output from the correlator can be represented as

$$\hat{\mathcal{V}}_{mn} = g_m g_n^* \mathcal{V}_{mn}, \tag{2.8}$$

where $\mathcal{V}_{mn}$ is the true visibility for baseline mn. g_m and g_n are referred as the complex gain term for antenna m and n, and these can be written as

$$g_m = |g_m| e^{j\psi_m} \tag{2.9}$$

If we assume that the gain and the amplitude of the visibility are constant for the range of (t, ν) space, we can write the output from the correlator at time and frequency (t_0, ν_0) to first order as

$$\begin{aligned} \hat{\mathcal{V}}_{mn}(t_k, \nu_l) &= |g_m||g_n||\mathcal{V}| \exp[j(\psi_m - \psi_n)(t_0, \nu_0)] \\ &\quad \times \exp\left[j \left(\left. \frac{\partial(\psi_m - \psi_n + \phi_{mn})}{\partial t} \right|_{(t_0,\nu_0)} (t_k - t_0) \right.\right. \\ &\quad \left.\left. + \left. \frac{\partial(\psi_m - \psi_n + \phi_{mn})}{\partial \nu} \right|_{(t_0,\nu_0)} (\nu_l - \nu_0) \right) \right], \end{aligned} \tag{2.10}$$

where ϕ_{mn} is the phase of the true visibility. t_k represents a time-integrated sample of the correlator output for frequency of ν_l. Delay and fringe rate are represented as

$$r_{mn} = \left. \frac{\partial(\psi_m - \psi_n + \phi_{mn})}{\partial t} \right|_{(t_0,\nu_0)} \tag{2.11}$$

and

$$\tau_{mn} = \left. \frac{\partial(\psi_m - \psi_n + \phi_{mn})}{\partial \nu} \right|_{(t_0,\nu_0)}, \tag{2.12}$$

respectively. The amplitudes of the gains are calibrated separately as described in Chapter 2.3. Then, if we use one antenna as the reference of the phase, the number of parameters to be determined is $3(n_a - 1)$. n_a is the number of antennas. Thus, the fringe solution can be obtained by least squares fitting when we assume the simple model of the source visibility $\mathcal{V}_{mn}$.

2.2 Astrometric observations

2.2.1 Phase referencing technique

For astrometric observations using VLBI, we need to conduct phase referencing observations to reduce the phase fluctuation contained in observed visibility data. This is also called as relative astrometry, and observe a phase reference source as well as a target source that we want to obtain its absolute position (Reid & Honma 2014).

From the definition of delay in Equation (2.1), position errors from VLBI can be estimated as

$$\Delta\theta \approx \frac{c\Delta\tau}{|D|}. \tag{2.13}$$

The position error, $\Delta\theta$ is controlled by the delay error in the calibration, $\Delta\tau$ and the baseline length, D. If we can reduce the delay error, the accuracy of the astrometric position is improved.

The delay measured by interferometer consists of several terms in addition to the geometric delay $\tau_{\rm geo}$.

$$\tau_{\rm obs} = \tau_{\rm geo} + \tau_{\rm tropo} + \tau_{\rm iono} + \tau_{\rm ant} + \tau_{\rm inst} + \tau_{\rm struc} + \tau_{\rm therm}, \tag{2.14}$$

where $\tau_{\rm tropo}$ and $\tau_{\rm iono}$ are the delays generated in the troposphere and ionosphere, respectively. $\tau_{\rm ant}$ is the delay error caused by position errors of antenna positions. $\tau_{\rm inst}$ is the delay generated in the instruments of antennas. $\tau_{\rm struc}$ is the delay error due to unmodeled structure of the source. And, $\tau_{\rm therm}$ is the thermal error of the delay.

In the relative astrometry, we obtain the difference of delays between the target and reference source:

$$\begin{aligned} \Delta\tau_{\rm obs} \;=\; & (\tau_{\rm geo,1} - \tau_{\rm geo,2}) \\ & +(\tau_{\rm tropo,1} - \tau_{\rm tropo,2}) + (\tau_{\rm iono,1} - \tau_{\rm iono,2}) \\ & +(\tau_{\rm ant,1} - \tau_{\rm ant,2}) + (\tau_{\rm inst,1} - \tau_{\rm inst,2}) \\ & +(\tau_{\rm struc,1} - \tau_{\rm struc,2}) + (\tau_{\rm therm,1} - \tau_{\rm therm,2}) \end{aligned} \tag{2.15}$$

$\tau_{\rm tropo}$, $\tau_{\rm iono}$, $\tau_{\rm ant}$, and $\tau_{\rm inst}$ are antenna-based delays. Thus, these quantities are reduced by using phase referencing.

Dominant source of the phase fluctuation in relative astrometry is known as tropospheric delays from wet atmosphere at 22 GHz band (Honma et al. 2008). If the tropospheric delay toward the phase reference source is identical to that toward the maser source, the effect of the tropospheric delay is canceled out. In practice, the difference in these tropospheric

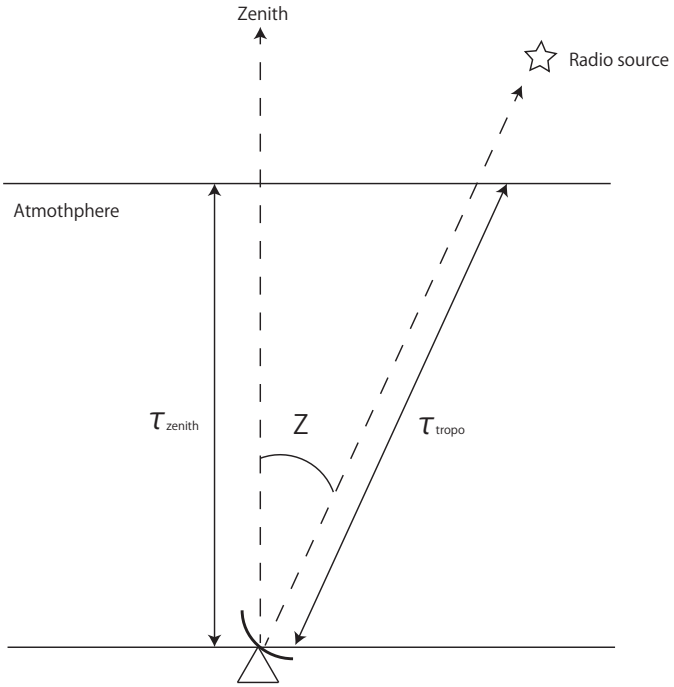

Figure 2.2: Schematic model of parallel plane atmosphere.

delays becomes large when the separation angle between these two sources are large. If we assume a plane parallel model for the troposphere (Figure 2.2), $\tau_{\rm tropo}$ can be written as

$$\tau_{\rm tropo} = \tau_{\rm zenith} \sec Z \qquad (2.16)$$

Here $\tau_{\rm zenith}$ is the tropospheric zenith delay.

The tropospheric delay between two sources are given by

$$\tau_{\rm tropo,1} - \tau_{\rm tropo,2} = \tau_{\rm zenith}(\sec Z_1 - \sec Z_2). \qquad (2.17)$$

Z_1 and Z_2 are the source zenith angles for the target source and the phase reference source, respectively.

The tropospheric delay caused by the water vapor rapidly changes on the timescale of about 100 sec at 22 GHz. Thus, we must measure the phase variations on a timescale shorter than that. Rapid switching between target and reference sources is usually applied to satisfy this condition. However, there are a lot of time loss through switching sources, and it cannot calibrate rapid fluctuation of phase within the timescale of switching.

2.2.2 Dual-beam observations with VERA

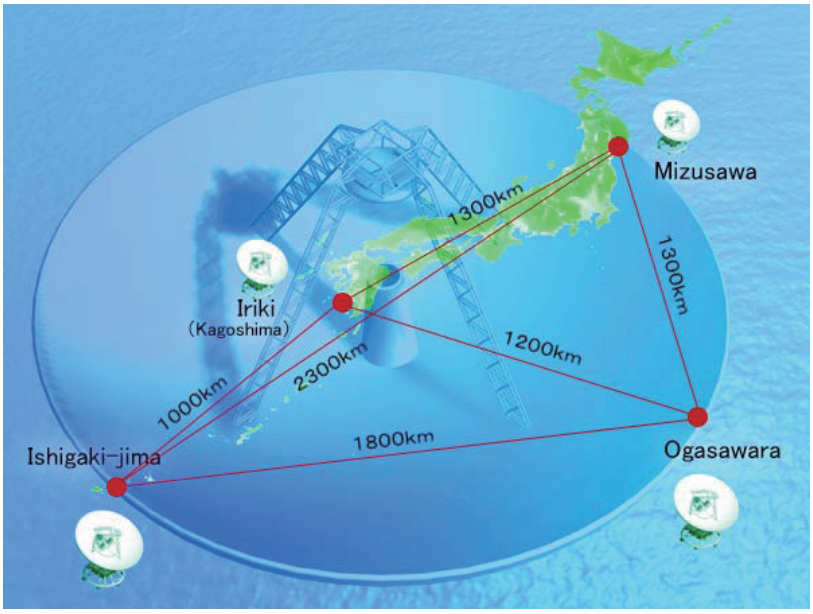

Figure 2.3: VERA array. Locations and baseline lengths are expressed (http://veraserver.mtk.nao.ac.jp).

VERA (VLBI Exploration of Radio Astrometry) is a VLBI array specially developed for astrometric observations of the Milky Way Galaxy. VERA array consists of four antennas in Mizusawa, Iriki, Ogasawara, and Ishigaki shown in Figure 2.3. All of them are 20-m parabola antennas. The longest baseline is Mizusawa-Ishigaki baseline with a baseline of about 2,300 km while the shortest is Iriki-Ishigaki baseline with 1,000 km. The angular resolution obtained with the longest baseline can be expected to be $\sim$ 1.2 mas (milli-arcsecond) at 22 GHz band.

The most remarkable point of VERA is the dual-beam receiver to observe the target source and the phase reference source, simultaneously. Figure 2.4 illustrates the concept of dual-beam system. Two receivers are mounted on rotation table for each antenna. The separation between two receivers is variable from 0.3 to 2.2 degrees. This dual-beam system can reduce the phase fluctuation of the troposphere more efficiently than a fast switching observation, which has been usually applied for earlier VLBI arrays. In addition, this system can achieve longer integration time for a target source because there is no loss due to switching target to reference sources.

Figure 2.5 shows residual fringe phase with dual-beam system of VERA for W49N and OH 43.8-0.1. These sources are separated by 0.°65 on the projected sky. Although

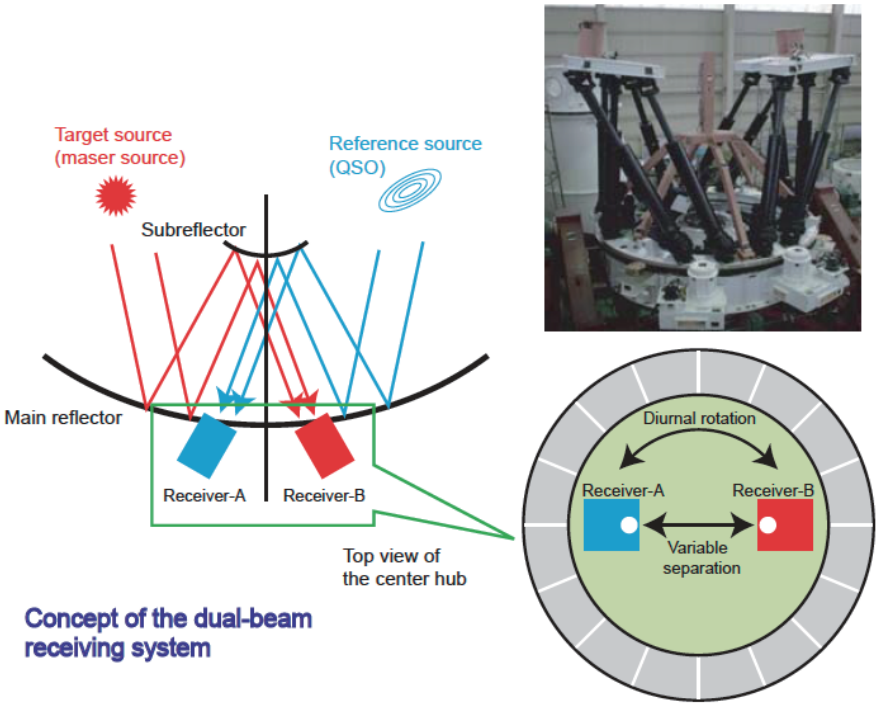

Figure 2.4: Dual beam system of VERA. Left panel shows concept of the dual-beam observations from a view of side. Right top shows a picture of dual-beam system. Right bottom is the dual-beam system when it is looked from top of antenna.

the residual fringe phases shown in the top panel have large fluctuations, we can see that the fluctuations coincide well with each other. The bottom panel clearly indicates that dual-beam system can reduce the phase fluctuation to 8 degree (rms). If we focus on the time from 1,100 s to 1,300 s on Figure 2.5, we can see that the phases rotate by 180 degree within 200 sec. It suggests that the dual-beam system on VERA can calibrate these very rapid phase rotation .

Hirota et al. (2007) measured trigonometric parallax of the Orion KL within the Orion Nebula (Fig. 2.6). The distance to the Orion Nebula from their study was $d = 437 \pm 19$ pc. The VERA project measured about 50 parallaxes for maser sources associated with star-forming regions.

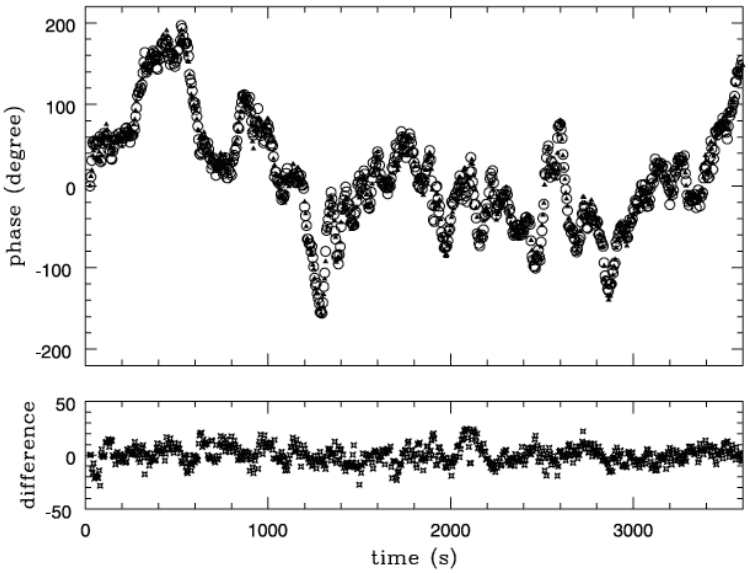

Figure 2.5: (Top) Residual fringe phases for W49N (open circle) and OH43.8-0.1 (triangle). (Bottom) Difference of fringe phase. Fig.1 of Honma et al. (2003).

2.3 Data reduction of phase reference observations for VERA

Throughout this thesis, data reduction for VERA data is conducted with the Astronomical Image Processing System (AIPS) developed by the National Radio Astronomical Observatory (NRAO). In the standard procedure of phase reference observation, Fringe search is conducted for phase reference continuum source. An extra-galactic QSO is usually selected as the phase reference source because QSOs are almost point sources. The radiation from QSOs are continuum emission from synchrotron radiation. Thus, the fringe search for the QSO can solve the solution of delay, rate, and phase. We refer this method as "normal" phase reference throughout this thesis.

In Figure 2.7, we summarized the typical process of data reduction for this observations with AIPS tasks.

1. Load visibility FITS data using task "FITLD".

2. Correct amplitudes in the visibility data by using measurements of auto-correlation using task "ACCOR". Normalization of the cross-correlation data, $C_{ij}(\tau)$, can be conducted by

$$\rho_{ij}(\tau) = \frac{C_{ij}(\tau)}{\sqrt{C_{ii}(\tau=0) \cdot C_{jj}(\tau=0)}}. \quad (2.18)$$

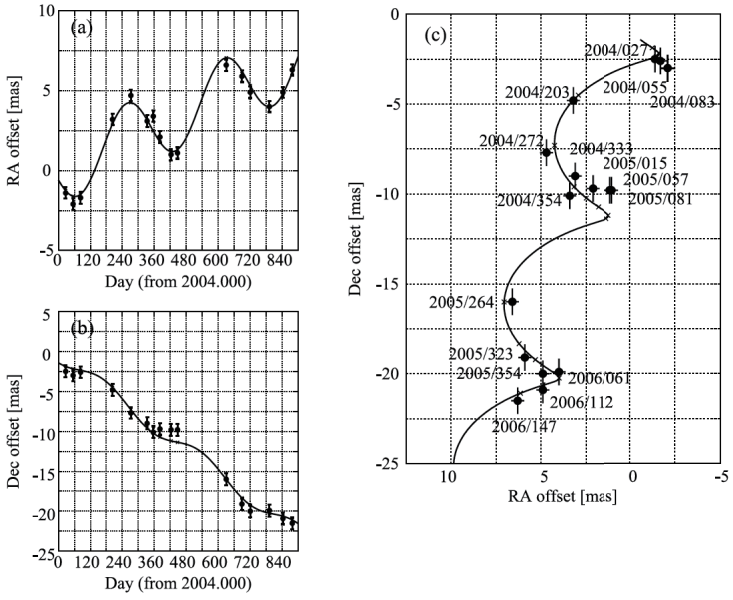

Figure 2.6: Parallax measurement for water maser source associated with Orion KL region. (a) Positions of the maser feature as a function of time in the direction of right ascension. (b) Same as (a) in the direction of declination. (c) Positions of the maser feature on the projected sky. Figure 3 of Hirota et al. (2007).

Here, $\rho_{ij}(\tau)$ is the normalized correlation function, and $C_{ij}(\tau)$ is the cross-correlation function presented at Equation (2.1), and C_{ii} and C_{jj} are the auto-correlation function for antenna i and j, respectively.

3. Correct gain table by using $T_{\rm sys}$ measurement and antenna gain information using task "APCAL". Strength of emission from a radio source received with a radio telescope is often represented with antenna temperature, T_A. This is defined as

$$T_A = \frac{SA_e}{2k}. \qquad (2.19)$$

Here, S is the flux density of the emission, A_e is effective aperture of the antenna, and k is the Boltzmann efficiency. When we define SEFD (System Equivalent Flux Density) as

$$\mathrm{SEFD} = \frac{2k(T_A + T_{\rm sys})}{A_e}, \qquad (2.20)$$

the visibility amplitude, S_{ij}, can be expressed as

$$S_{ij} = \rho_{ij}\sqrt{\mathrm{SEFD}_i \cdot \mathrm{SEFD}_j}, \qquad (2.21)$$

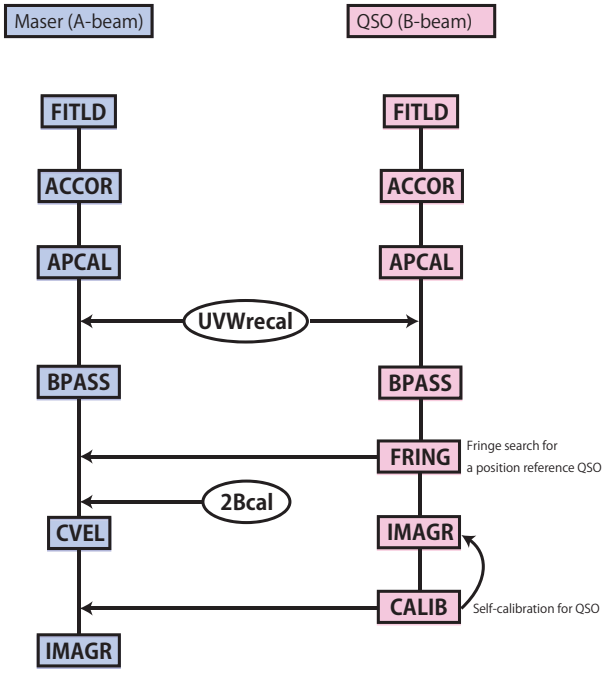

Figure 2.7: The flow of the data reduction in normal phase-reference observation. Left stream represents the reduction for maser source received with A-beam receiver. Right the reduction for QSO with B-beam receiver.

where subscripts of SEFD correspond to different antennas (Thompson et al. 2017). In VERA observations, $T_{\rm sys}$ is measured by Chopper-Wheel method.

4. UVW recalculation data is applied for the phase-referencing. The a-priori delay with the accuracy of $\sim$ 1 nsec in the correlation is not accurate enough for the phase-referencing, because the accurate source position and station position are unknown in the correlation. The accurate delay with the accuracy of $\sim$ 0.01–0.1 nsec is recalculated using the latest models and parameters such as the source position, the station position, the Earth orientation parameter, and the troposphere and the ionosphere calibration method.

5. Calibrate band character by using the auto-correlation data using task "BPASS".

6. Fringe search for a phase-reference QSO in B-beam to obtain residual delay, rate and phase offset using task "FRING". Then, Apply it to A-beam.

7. Calibrate instrumental delay and phase between two beams. They are measured by injecting the artificial signal using the noise source installed in the antenna.

8. Image and conduct self-calibration for the QSO using task "IMAGR" and "CALIB", respectively. Copy the correction table to A-beam. Even in this time, there are residual amplitude and phase on the visibility data mainly due to the effect from source structure. In the self-calibration process, we first assume the model structure of the source. When we apply gain function $\boldsymbol{g}$ for model visibility $\mathcal{V}^{i,j}_{\rm model}(t)$ calculated from the model structure, this should be observed as $\boldsymbol{g}_i\boldsymbol{g}^*_j\mathcal{V}^{i,j}_{\rm model}(t)$. Comparing observed visibility $\hat{\mathcal{V}}^{i,j}(t)$ and the model visibility plus gain function $\boldsymbol{g}_i\boldsymbol{g}^*_j\tilde{\mathcal{V}}^{i,j}(t)$, we evaluate χ^2 as
$$\chi^2 = \sum_{i,j}\int_t w_{i,j}(t)| \qquad (2.22)$$

9. Obtain Final phase-referenced image of the target maser spot relative to the position reference QSO using task "IMAGR".

2.4 Inverse phase reference

In normal phase reference observations described above fringe search was conducted for the position reference QSO to obtain the residual offset of delay, rate, and phase. This is capable for the situation in which the phase reference QSO is enough intense to solve the fringe solutions. The inverse phase reference technique solves the fringe solution for the maser spot instead of the phase reference QSO. Then, we can measure the relative position of the maser spot to the QSO for the case that the QSO is not strong. The detailed procedure of the data reduction for inverse phase reference with VERA is followed to that in Imai et al. (2012). The required condition for the inverse phase reference is that the maser spot is intense to obtain the fringe solution. In the case of the standard setup with VERA observations, the flux density required for the maser spots is typically higher than 10 Jy. By using the inverse phase reference technique, we can conduct phase referencing for weak QSOs of down to about 30 mJy. Figure 2.8 shows the flow of the data reduction for inverse phase reference. The major difference between normal phase reference and inverse phase reference is following :

- Residual offset of the delay is solved for strong delay calibrator like NRAO530 and 3C84 because the maser emission has line spectra, and can't obtain delay solution.

- Fringe search for the maser spot can obtain the residual offset of rate and phase. Then, these solutions are applied to B-beam QSO data.

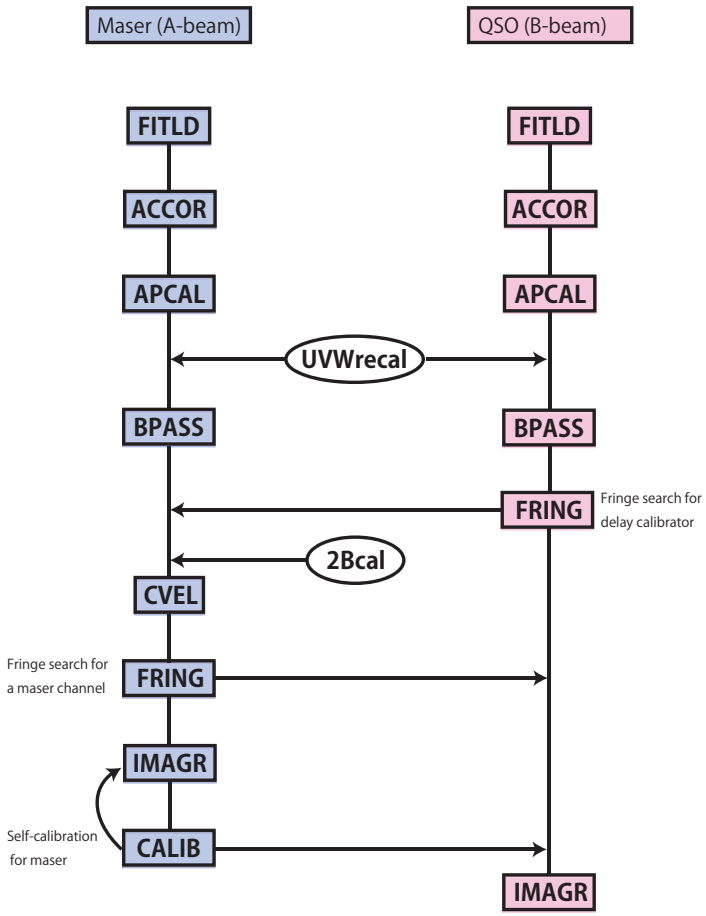

Figure 2.8: The flow of data reduction for inverse phase-reference observation. Left stream represents the reduction for maser source received with A-beam receiver. Right the reduction for QSO with B-beam receiver.

- The relative position of QSO with respect to the maser spot is obtained from the final image. The sign inversion of the position is required to obtain the position of the maser spot.

Chapter 3 Triangle phase referencing

3.1 Introduction of the triangle phase referencing

3.1.1 Purpose

To describe the complete three dimension velocities of molecular gas clouds in the CMZ, we have to measure proper motions for several sources spread in the whole area of CMZ. However, As already mentioned at Chapter 1.3, the normal phase referencing and inverse phase referencing observations require strong QSOs and maser source enough to obtain fringe solutions, respectively. The number of such strong sources are limited. Thus, we have to seek other ways involving new facilities and techniques to proceed this study.

Here, we show a new technique of observation using strong maser sources. In a situation that there is no strong background QSO around a target maser source, we cannot conduct phase referencing observations because no fringe solutions could be obtained from the QSO. If there is strong maser sources instead of QSO, we can use the maser source as a phase reference source, and obtain the absolute position of the target maser sources relative to the position reference QSO. Note that this phase reference maser source is not the target maser source which we want to measure the proper motion and parallax. In this thesis, we refer the phase reference maser, position reference QSO, and target maser as PRM, PRQ, and TM, respectively.

3.1.2 Principle of the triangle phase referencing

Figure 3.1 shows the schematic illustration comparing the techniques of phase referencing. Normal phase reference shown in the left panel uses a background QSO as a phase reference source, and measure the relative position offset of a target maser source to the QSO by applying its phase solution. Inverse phase reference observation in the middle panel uses a target maser as a phase reference source. Then, the position of a background QSO relative to the target maser is obtained. This inverse phase reference technique was applied in the data reduction described in Chapter 4 and 5. The right panel in Figure 3.1 and Figure 3.2 show the concept of our new phase referencing technique. In this new technique, we use a PRM in addition to a PRQ and TM which is included in normal and inverse phase referencing observations. We can measure the relative positions of a target maser source (TM) and a position reference QSO (PRQ) to the phase reference maser. We can obtain the relative position of the TM to the PRQ by comparing these position offsets. In RPM–TM

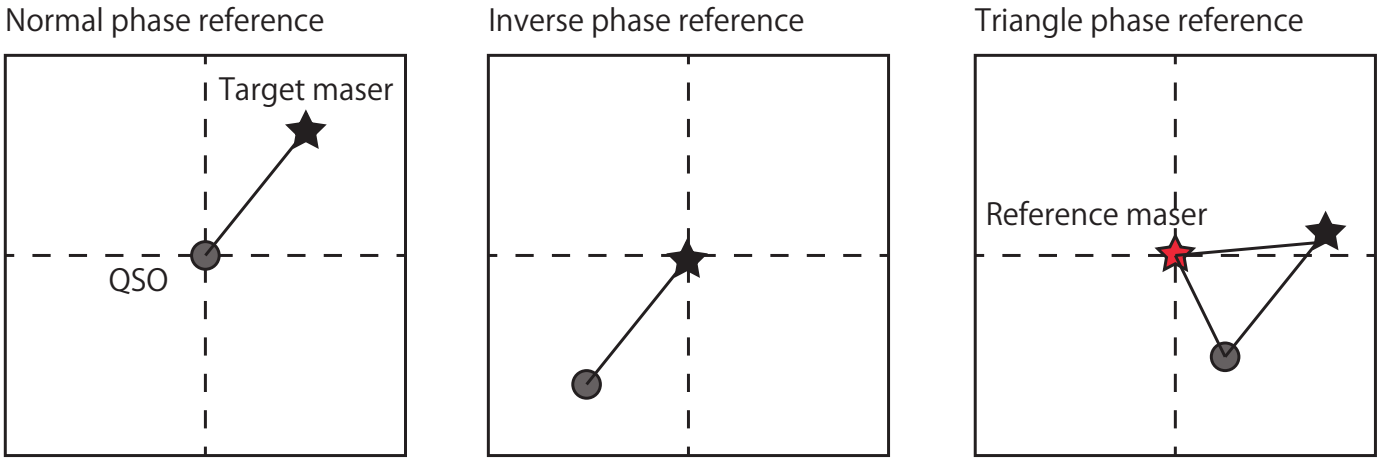

Figure 3.1: The schematic illustration of the phase referencing techniques. (Left) : the normal phase referencing observations. (Middle) : the inverse phase referencing observations. (Right) : the triangle phase referencing observations. In each panel, filled circle indicates the position reference QSO, star is the target maser of which we want to obtain its astrometric position, and red star is the phase reference maser source we use in the triangle phase reference observations.

pair phase referencing, we can obtain the delay difference between PRM and TM. However, the PRM as well as the TM have proper motion and parallax because the PRM is also the Galactic source. Thus, the relative delay obtained from PRM–TM pair phase referencing contains the information related to both the PRM and TM.

$$\Delta\tau_{\mathrm{PRM-TM}} = \tau_{\mathrm{TM}} - \tau_{\mathrm{PRM}}. \quad (3.1)$$

We can obtain delay difference of PRM relative to PRQ by conducting PRM–PRQ phase referencing simultaneously.

$$\Delta\tau_{\mathrm{PRM-PRQ}} = \tau_{\mathrm{PRQ}} - \tau_{\mathrm{PRM}} \quad (3.2)$$

Subtracting Eq.(3.2) from Eq.(3.1), we finally obtain the relative delay of the TM to PRQ whose position is accuratelly determined.

$$\Delta\tau_{\mathrm{PRM-TM}} - \Delta\tau_{\mathrm{PRM-PRQ}} = \tau_{\mathrm{TM}} - \tau_{\mathrm{PRQ}} \quad (3.3)$$

From the relationship of Eq.(2.2), this corresponds to a position offset between the TM and PRM. We name this new phase referencing technique as the triangle phase referencing because this technique uses three sources.

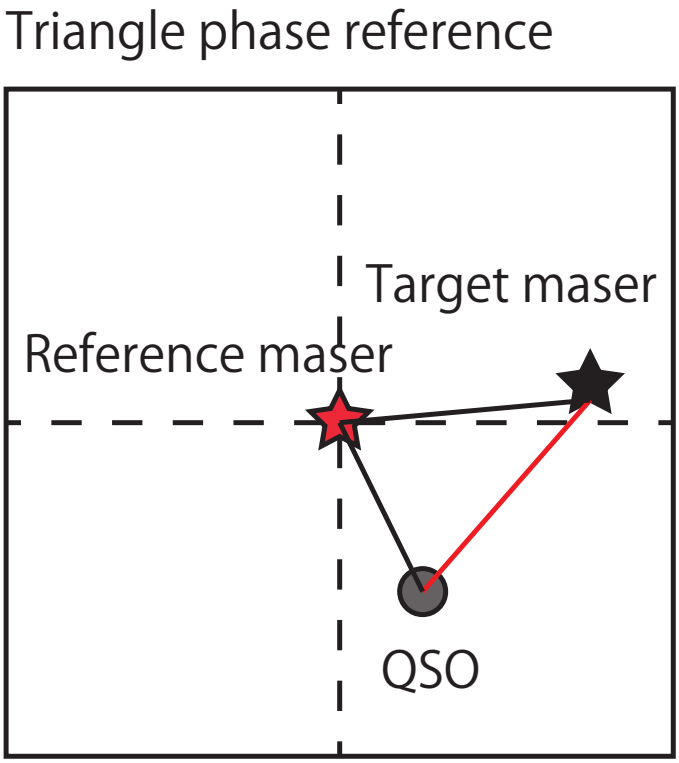

Figure 3.2: Concept of the triangle phase referencing observations. Filled circle indicates a position reference QSO, a black star is a target maser of which we want to obtain the astrometric position, and a red star is a phase reference maser source we use in the triangle phase referencing observations. The red line is the relative position of the target maser to position reference QSO.

The required conditions for the PRM are following :

- These intensities are strong enough to obtain the PRM image whose signal-to-noise ratio (SNR) is more than seven by conducting fringe search for the maser spot itself within the coherence time.
- PRM–PRQ and PRM–TM pairs have a separation angles within the limit of the dual-beam system (2.2 degree).

If these requirements are satisfied, we can observe weak maser sources whose fringe solutions could not be obtained in the condition that there are no strong QSO in the vicinity. When we observe a source, the noise level σ for each baseline can be expressed as

$$\sigma = \frac{2k}{\eta} \frac{\sqrt{T_{\mathrm{sys},1} T_{\mathrm{sys},2}}}{\sqrt{A_{e1} A_{e2}} \sqrt{2B\tau}}, \qquad (3.4)$$

where k is Boltzmann constant, η is quantization efficiency (~ 0.88), $T_{\rm sys}$ is system noise temperature, A_e is antenna effective aperture area, B is the bandwidth, and τ is on-source integration time. When we conduct the phase referencing observations with the dual-beam system of VERA, 15 spectral IFs σ are assigned for a continuum source and one IF for a maser source. Thus, the total bandwidth for the continuum source is 240 MHz because each IF has 16 MHz. The noise level is calculated to be $\sigma = 24$ mJy from the 20-m antenna dish, the aperture efficiency $\eta_A = 50\%$, $B = 240$ MHz, $\tau = 1$ min, and $T_{\rm sys} = 200$ K. Thus, the flux density of the continuum source which can be detected for each baseline is 168 mJy with signal-to-noise ratio $SNR = 7$. $SNR = 7$ is generally required for detecting fringe solutions for VLBI observations. On the other hand, the noise level for of the maser source is calculated to be 2.1 Jy from the bandwidth $B = 31.25$ kHz which is the bandwidth of a spectral channel in 512 spectral channels with 16 MHz bandwidth, and the flux density of the maser source is obtained to be 14.5 Jy for $SNR = 7$. These flux densities are the detection limits of the reference sources which can be detected within the coherence timescale ($\sim$ 100 sec for 22 GHz). Then, we can integrate for all on-source time of the paired source (a maser source for the normal and a continuum source for the inverse phase referencing), after the phase solutions are transferred from the reference source to the paired source. Thus, the normal phase referencing observations can detect a target maser down to 1.3 Jy assuming the on-source time of 120 min when a continuum source is strong enough to detect within the integration time of 1 min (168 mJy). On the other hand, the inverse phase referencing can detect a continuum source down to 15 mJy when a maser source is strong (14.5 Jy).

In the triangle phase referencing, we can integrate a TM and a PRQ for all on-source time by transferring the phase solutions solved for a PRM within the coherent time, and can detect a weak TM down to 1.3 Jy and a weak PRQ down to 15 mJy.

Table 3.1 summarizes the typical conditions required for each phase-referencing technique in VERA observations. The detection limits are roughly written because the limits vary on the system noise temperature, $T_{\rm sys}$, and the integration time, τ.

- The normal phase referencing requires a strong PRQ which can obtain fringe solution within the coherence time, and can obtain phase referenced image of a weak TM down to about 1 Jy.

- The inverse phase-referencing requires a strong maser spot (> 10 Jy) for fringe search. This technique is usually applied for the situation in which there are only weak PRQ (~ 10 mJy) in the vicinity of the TM.

Table 3.1: Requirement for the normal, inverse, and triangle phase referencing.

	Target maser	Position reference QSO	Phase reference maser
Normal	1 Jy	100 mJy	–
Inverse	10 Jy	10 mJy	–
Triangle	1 Jy	10 mJy	10 Jy

- The triangle phase reference, which is our new technique, is a useful method for the situation in which the TM ($\sim$ 1 Jy) and PRQ ($\sim$ 10 mJy) are weak but detectable by using a strong PRM whose intensity is more than 10 Jy over years close to these sources.

3.2 Observational process

Here, we show the observational process of our triangle phase referencing observations. In this observation technique, we have to observe two different pairs of sources including TM, PRM, and PRQ. Figure 3.3 shows the example of time schedule for the triangle phase referencing observations. First, we observe a strong delay calibrator (e.g. 3C84, NRAO530, etc.) in both A- and B-beam. This The strong delay calibrator is observed every 90 minutes in the observation. On-source time for the delay calibrator is about 5 minute for each scan. Second, a pair of the PRM and the PRQ is scheduled. Then, a pair of the PRM and a TM follows. The duration time for each scan is about 15 minutes. If the duration time is too long, the observations lose some part of uv-coverage in another pair. On the other hand, These three kinds of scans are repeated in the allocated time for the observations.

3.3 Data reduction process

Reduction process of the triangle phase referencing observations is summarized in Figure 3.4. The data splits into three parts. These were consists of a PRM in A-beam, a PRQ in B-beam, and a TM in B-beam. The solution of fringe search for a delay calibrator in PRQ data was applied to both maser data same as the data reduction for inverse phase referencing described above. Then, phase and rate solutions from fringe search for the PRM were applied to both the PRQ and TM. The obtained images are (i) the PRQ image relative to the PRM and (ii) the TM image relative to the PRM. Finally, the position of the TM spot relative to the PRQ was obtained by comparing the positions of sources in the two images.

We conducted the triangle phase referencing observations for several sources toward the

Figure 3.3: Schedule of the triangle phase referencing observations. Orange color shows the observations of delay calibrator. Dummy source means that no source is observed at that beam. Red, green, and blue represent the observations for PRM, PRQ, and TM, respectively.

Galactic center region. These results are described in Chapter 6. Before preceding to main results of astrometric observations toward the Galactic center region, since this technique is developed in this thesis at the first time, we show the verification of the accuracy obtained from the triangle phase referencing observation.

3.4 Test observations of triangle phase referencing toward W3OH region

3.4.1 Purpose

To evaluate the accuracy this new technique which we call as a triangle phase referencing, we have conducted test observations for sources whose intensities are enough strong to detect fringe solutions for all three sources including TM, PRM, and PRQ.

Target sources for this test observations were selected under a condition that all three sources including TM, PRM, and PRQ were intense enough to obtain the fringe solutions for theirselves within the short coherent time of about 1 minute. This condition was required to verify the accuracy of the position obtained by the triangle phase referencing through a comparison of the astrometric results between the normal and triangle phase referencing. Based on these conditions, we conducted test observations of triangle phase referencing technique toward the W3OH region. The purpose of this test observations is to obtain position accuracy attained from triangle phase referencing, and to verify the availability of the parallax and proper motion measurement.

3.4.2 Observations

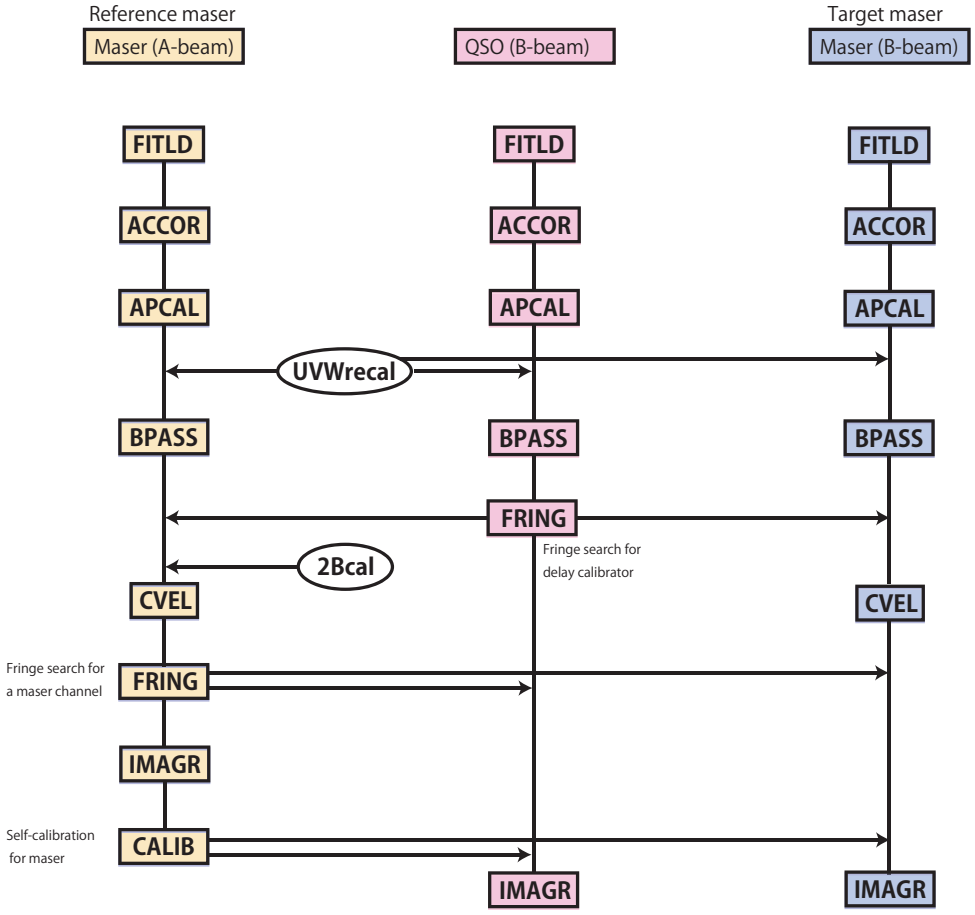

Figure 3.4: The process of data reduction for the triangle phase referencing observations. Left stream represents the reduction for the PRM received with A-beam receiver. Center is the reduction for the PRQ with B-beam receiver. Right is for the TM received with B-beam.

We conducted VLBI observations of water maser sources associated with the W3OH region at a rest frequency of 22.235080 GHz using VERA during the period from 2016 to 2017. The number of observation epochs was eight. G135.28+02.80 was observed as TM which we want to measure the absolute position. PRM was W3OH, and PRQ was J0244+6228. As noted in the previous section, the triangle phase reference observation contains two kinds of pairs in each observation using dual-beam system of VERA. One is a PRM–TM pair, and another is a PRM–PRQ pair. In each epoch, the on-source time of the W3OH–G135.28+02.80 pair was 2 hour, while that for the W3OH–J0244+6228 was 1 hour 45 min. Another pair of G135.28+02.80–J0244+6228 pair was observed to obtain astrometric results from normal phase-reference. J0244+6228 was an extragalactic radio source,

Table 3.2: The coordinates of sources in the test observations.

Source	R.A. position	Dec. position	description	Separation angle
W3OH	2h27m4.6071s	+61d52m24.731s	Reference maser	–
J0244+6228	2h44m57.696681s	+62d28m6.51550s	Position reference QSO	2.170 deg.
G135.28+02.80	2h43m28.5825s	+62d57m8.390s	Target maser	2.183 deg.

Table 3.3: Summary of observations and detected features. $V_{\rm TM}$ indicates the velocity of the spot that we measured the parallax and proper motions. $V_{\rm PRM}$ indicates the velocity of the spot that we used as a reference spot for W3OH.

Epoch	Date	$V_{\rm TM}$ ($\rm km\,s^{-1}$)	$V_{\rm PRM}$ ($\rm km\,s^{-1}$)
1	2015 December 24	-73.28	-47.24
2	2016 September 6	-73.28	-47.24
3	2016 September 14	-73.28	-47.24
4	2016 September 15	-73.28	-47.24
5	2016 December 26	-73.28	-47.24
6	2017 January 31	-73.28	-47.24
7	2017 February 28	-73.28	-47.24
8	2017 April 4	-73.28	-47.24
9	2017 May 2	-73.28	-47.24

and its projected separation to the W3OH was 2.17°. Table 3.2 lists the sources in this test observation. Separation angle to W3OH was described in the last row of J0244+6228 and G135.28+02.80. Figure 3.5 shows the position of sources in this observations on the sky.

3C84 was also observed for 10 min per every 90 min to calibrate group-delay residuals. The tracking center positions for W3OH, J0244+6228, and G135.28+02.80 were summarized on Table 3.3. Table 3.3 also lists the dates of observations and the detected features.

In Figure 3.6, we showed the UV-coverages of W3OH and G135.28+02.80 at epoch 1. These UV-coverages were almost circularly distributed because of high elevation of these sources from VERA stations. The synthesized beam size is $1.36\,\rm mas \times 0.72\,\rm mas$ with the position angle of $-44°$ from north. The positive value of the position angle refers counter-clockwise rotation. The delay error occurred from atmospheric effects were small.

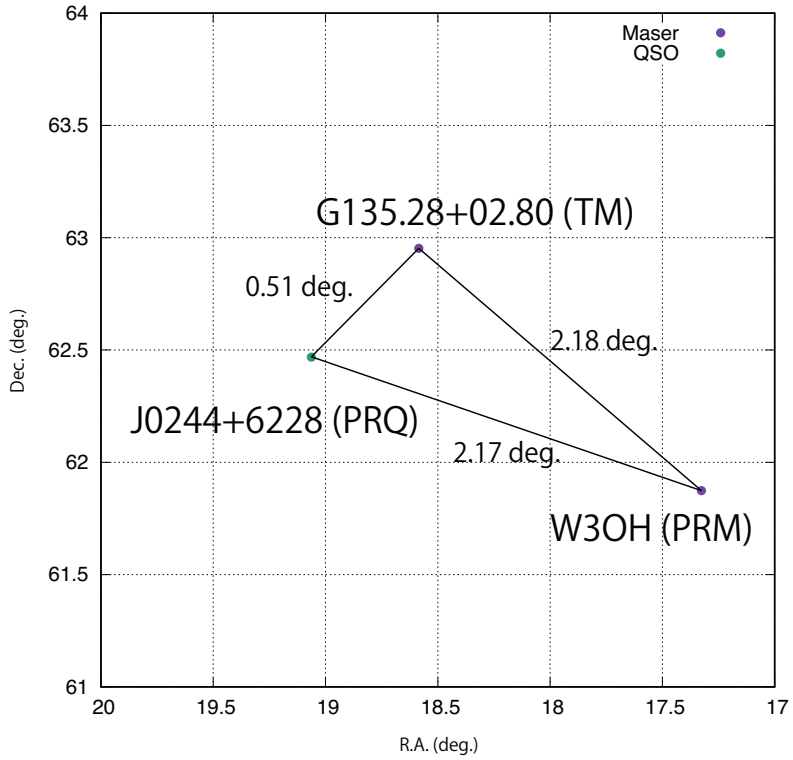

Figure 3.5: Coordinate and distribution of sources in the test observations. Purple circle indicates maser sources. Green circle is QSO.

3.4.3 Results and discussion

In this part, we show the results of test observations toward W3OH region. The evaluation of the triangle phase referencing is conducted based on three points of view by comparing with normal phase reference.

1. Thermal errors occurred from reduction process in the triangle phase referencing.

2. The differences of astrometric position obtained from each phase referencing technique.

3. Comparison of annual parallax and proper motions between normal and triangle phase referencing.

We used a maser spot of W3OH at $V_{\rm lsr} = -47.24\,{\rm km\,s^{-1}}$ as the PRM, and conducted phase referencing to a spot of G135.28+02.80 at $V_{\rm lsr} = -73.28\,{\rm km\,s^{-1}}$ as the TM.

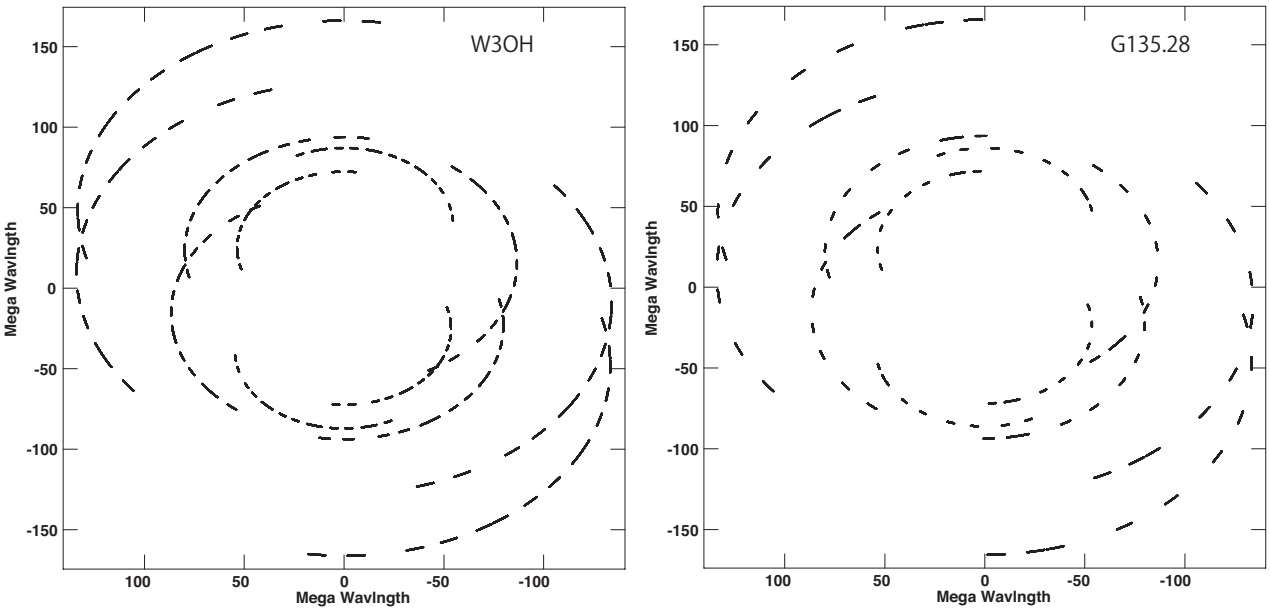

Figure 3.6: UV coverage for (left) W3OH and (right) G135.28+02.80 in observations epoch 1.

Thermal error

First, we will estimate the position error caused by the thermal noise (thermal error) contained in each phase referencing technique by showing the each phase referenced images. We expect the thermal error in the triangle phase referencing is less than twice the thermal error in the normal phase referencing. Because the relative position offset of TM to PRQ, which is the goal of the triangle phase referencing, is obtained from the combination of the phase referenced positions for the PRM–PRQ and PRM–TM pairs in the triangle phase referencing, the thermal errors associated with this observation is also the combination of those in each image:

$$\sigma_{\mathrm{thermal,triangle}} = \sqrt{\sigma^2_{\mathrm{thermal,PRM-TM}} + \sigma^2_{\mathrm{thermal,PRM-PRQ}}}. \quad (3.5)$$

The triangle phase referencing observations have to observe two pairs within a schedule. Thus, on-source time for each pair is less than half of that for normal phase referencing observations which contain only a TM–QSO pair except for delay calibrator. According to the relationship between noise level σ_{theo} and on-source time τ_a (Anantharamaiah et al. 1989):

$$\sigma_{\mathrm{theo}} \propto \tau_a^{-1/2}, \quad (3.6)$$

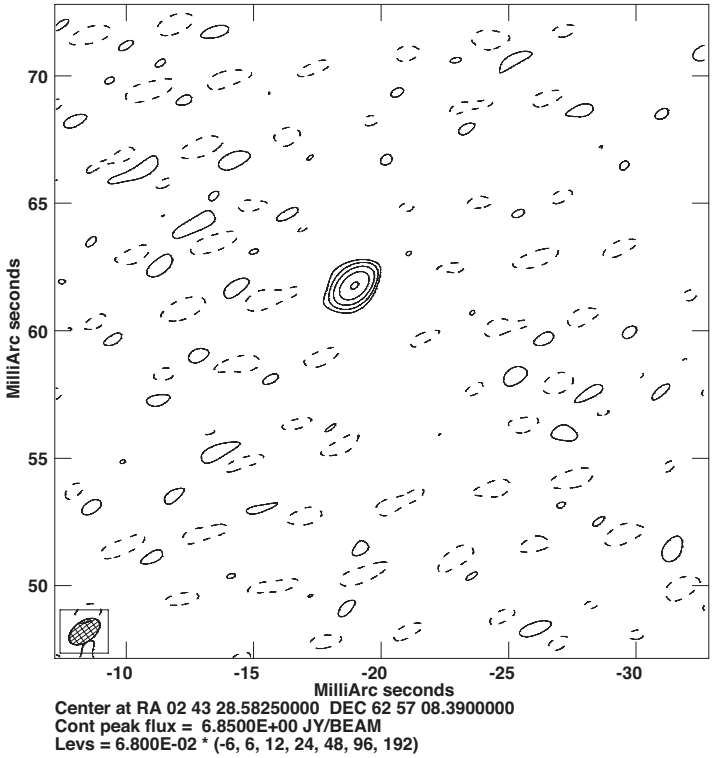

Figure 3.7: Phase referenced image obtained of G135.28+02.80 from the normal phase reference observations at epoch 6. Contours are drawn at $68 \times (-6, 6, 12, 24, 48, 96, 192)$ mJy.

the level of the thermal noise in each phase referenced image of the triangle phase referencing becomes larger by $\sqrt{2}$ than the maser–QSO only observations.

Thus, if we roughly assume $\sigma_{\rm thermal,normal} \approx \sqrt{2}\sigma_{\rm thermal,PRM-TM} = \sigma_{\rm thermal,PRM-PRQ}$, we can obtain

$$\sigma_{\rm thermal,triangle} \approx \sqrt{2}\sigma_{\rm thermal,normal}. \quad (3.7)$$

Here, we demonstrate it using the observation data at epoch 6. The thermal error can be calculated from signal-to-noise ratio (SNR) as

$$\sigma_{\rm thermal} = \frac{\theta_{\rm beam}}{2 \times SNR}, \quad (3.8)$$

where, $\theta_{\rm beam}$ is the synthesized beam (FWHM) size (Reid et al. 1988; Reid & Honma 2014).

Figure 3.7 shows the phase referenced image of a maser spot of G135.28+02.80 reduced by the normal procedure of phase referencing explained at Chapter 2.3, which conducts fringe search for J0244+6228 (PRQ). The line-of-sight velocity of the maser spot is $V_{\rm lsr} = -73.28\,{\rm km\,s^{-1}}$. In this image, the peak intensity of the maser spot is 6.85 Jy/beam while

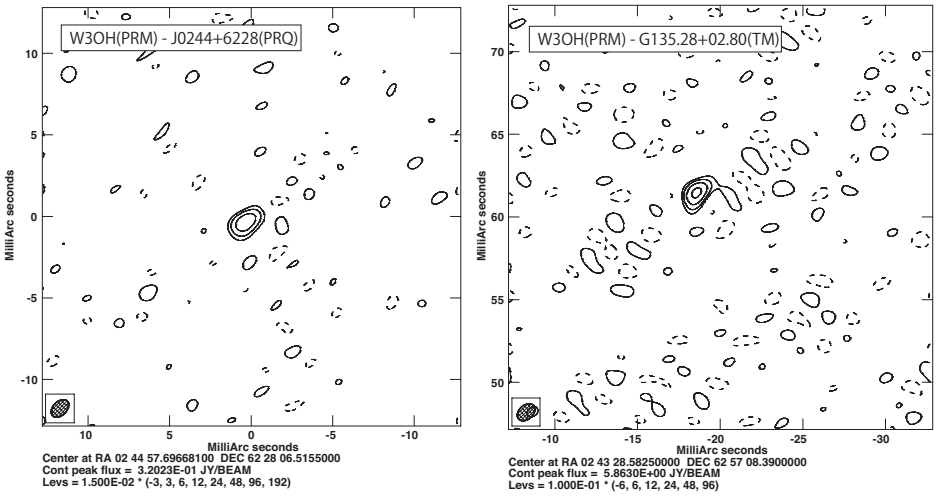

Figure 3.8: Images obtained through the triangle phase reference observations at epoch 6. (Left) Phase referenced image of J0244+6228 (PRQ) relative to W3OH (PRM). Contours are drawn at $15 \times (-3, 3, 6, 12, 24, 48, 96, 192)$ mJy. (Right) Phase referenced image of G135.28+02.80 (TM) relative to W3OH (PRM). Contours are drawn at $100 \times (-6, 6, 12, 24, 48, 96)$ mJy.

the rms noise level is 0.21 Jy/beam. Thus, The SNR achieved in this image is 33. The thermal error is about 15 μas for this image according to Equation (3.8).

On the other hand, Figure 3.8 shows the phase referenced image involved in the triangle phase referencing technique. As mentioned at Chapter 3.3, there are two images including the TM image relative to PRM (PRM–TM image), and the PRQ image relative to PRM (PRM–PRQ image).

The SNR for PRM–TM pair is calculated to be 25 because the peak intensity of 0.32 Jy/beam and the rms noise level of 0.013 Jy/beam. Similarly, the SNR for PRM-PRQ pair is calculated to be 15 from the peak intensity of 5.9 Jy/beam and the rms of 0.38 Jy/beam. The thermal errors for each image are $(\sigma_{\mathrm{thermal,PRM-TM}}, \sigma_{\mathrm{thermal,PRM-PRA}}) = (20, 33)$ μas from Equation (3.8), . The thermal error involved in astrometric results from triangle phase reference is calculated as 39 μas from Eq.(3.5).

Therefore, the the thermal error of the triangle phase referencing is larger than that of the normal phase referencing by twice. The thermal errors levels vary on epoch by epoch depending on intensities of sources and the thermal noise level in observations. Their values

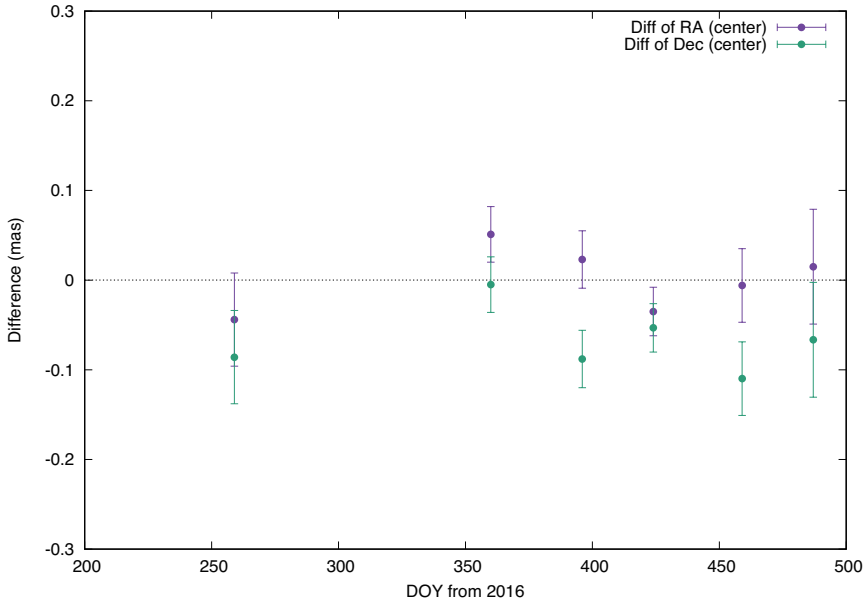

Figure 3.9: The difference of position between the normal and triangle phase referencing for G135.28+02.80. Purple and green circle represent differences for the direction of R.A. and Dec., respectively. Error bars are obtained from the thermal errors.

of each epoch are summarized on Table 3.5.

Position difference between phase-reference techniques

Next, we compare the absolute position of G135.28+02.80 obtained from normal and triangle phase referencing technique.

Figure 3.9 is the difference of position obtained from the normal and triangle phase referencing technique for a maser spot in G135.28+02.80.

Averages of the position differences over epochs are $1 \pm 15\,\mu$as and $-70 \pm 15\,\mu$as for the direction of R.A. and Dec., respectively, where the error is the standard error. Error bars in the plot are calculated from the combined thermal noise obtained by signal-to-noise ratio of the phase referenced images. These values are listed no Table 3.6. Table 3.7 summarizes the average differences between different phase referencing techniques.

Although there is the systematic position shift between the normal and triangle phase referencing, the shift identical for all epochs does not affect to the parallax and proper motion measurements because we only require the relative positions between epochs in the astrometric fitting. Indeed, there is systematic offset between phase referencing techniques. However, since this offset is attributed to the difference of uv-coverages between sources in

Table 3.4: Positions and errors of a maser source G135.28+02.80 at $V_{\rm lsr} = -73.28\,{\rm km\,s^{-1}}$ with the normal phase referencing observations.

DOY	Normal phase referenecing		Thermal error	Systematic error		Total error	
from 2016	$\Delta\alpha_{\rm nor}$ (mas)	$\Delta\delta_{\rm nor}$ (mas)	$\sigma_{\rm thermal}$ (μas)	$\sigma_{\rm sys,ra}$ (μas)	$\sigma_{\rm sys,dec}$ (μ as)	$\sigma_{\rm tot,ra}$ (μas)	$\sigma_{\rm tot,dec}$ (μas)
259	-18.593	61.964	43	33	33	53	53
360	-18.849	61.884	12	33	33	33	33
396	-18.910	61.802	15	33	33	34	34
424	-18.930	61.726	23	33	33	36	36
459	-18.836	61.611	27	33	33	41	41
487	-18.687	61.597	51	33	33	60	60

Table 3.5: Positions and errors of a maser source G135.28+02.80 at $V_{\rm lsr} = -73.28\,{\rm km\,s^{-1}}$ with the triangle phase referencing observations.

DOY	Triangle phase referenecing		Thermal error	Systematic error		Total error	
from 2016	$\Delta\alpha_{\rm tri}$ (mas)	$\Delta\delta_{\rm tri}$ (mas)	$\sigma_{\rm thermal}$ (μas)	$\sigma_{\rm sys,ra}$ (μas)	$\sigma_{\rm sys,dec}$ (μ as)	$\sigma_{\rm tot,ra}$ (μas)	$\sigma_{\rm tot,dec}$ (μas)
259	-18.549	62.049	60	10	10	61	61
360	-18.900	61.889	44	10	10	45	45
396	-18.933	61.890	48	10	10	49	49
424	-18.895	61.779	38	10	10	39	39
459	-18.830	61.721	51	10	10	52	52
487	-18.702	61.663	95	10	10	96	96

dual-beam system, the offset should be almost identical over epochs.

The specific errors in the triangle phase referencing technique is calculated to be 37 μas from the standard deviation of the position differences in Figure 3.9. This is smaller than thermal errors contained in the triangle phase referencing ($\sigma_{\rm thermal}$ = 38–95; Table 3.5). This fact indicates that the dominant source of error in the triangle phase referencing observations is thermal error due to weak flux densities of TM and PRQ.

Comparison of astrometric result

Finally, we demonstrate that the parallax and proper motions obtained by the triangle phase referencing observation is same as those by the normal phase referencing within their errors. Figure 3.10 shows the comparison of the astrometric results for the normal and triangle

Table 3.6: Comparison of the phase referenced position between "Normal" and "Triangle" phase referencing reduction for a maser source G135.28+02.80.

DOY from 2016	Differences	
	$\Delta\alpha_{\rm nor} - \Delta\alpha_{\rm tri}$ (mas)	$\Delta\delta_{\rm nor} - \Delta\delta_{\rm tri}$ (mas)
259	-0.044	-0.086
360	0.051	-0.005
396	0.023	-0.088
424	-0.035	-0.053
459	-0.006	-0.110
487	0.015	-0.067

Table 3.7: Comparison of the phase referenced position between normal and triangle phase referencing reduction for a maser source G135.28+02.80.

Target source	Comparison	Average differences		Standard errors	
		R.A.(μas)	Dec.(μas)	R.A.(μas)	Dec.(μas)
G135.28+02.80	Normal–Triangle	1	-70	15	15

phase referencing observations of G135.28+02.80. We succeeded to measure a maser spot over six epochs at $-73.28\,{\rm km\,s^{-1}}$. In this figure, both parallax and proper motions are the parameter for fitting. The fitting results are listed on Table 3.8. We can see both parallax and proper motions for the triangle phase referencing observations are consistent with those for the normal phase referencing within these errors. The error of Figure 3.10 was calculated by combination of the thermal error and the systematic error.

$$\sigma_{\rm tot} = \sqrt{\sigma^2_{\rm thermal} + \sigma^2_{\rm sys}} \qquad (3.9)$$

$\sigma_{\rm thermal}$ was obtained from signal-to-noise ratio of the phase referenced image for each epoch. $\sigma_{\rm tot}$ was calculated to achieve the reduced χ^2 value to be unity by applying identical $\sigma_{\rm sys}$ for all epochs. This systematic error was 33 μas in right ascension and 33 μas in declination for normal phase referencing, respectively. For the triangle phase referencing, $\sigma_{\rm thermal}$ is the combination of thermal errors for two phase referenced image. The systematic error for the triangle phase referencing was 15 μas in right ascension and 46 μas in declination.

3.4.4 Summary of this chapter

We summarized the results of test observations for the triangle phase referencing toward W3OH region.

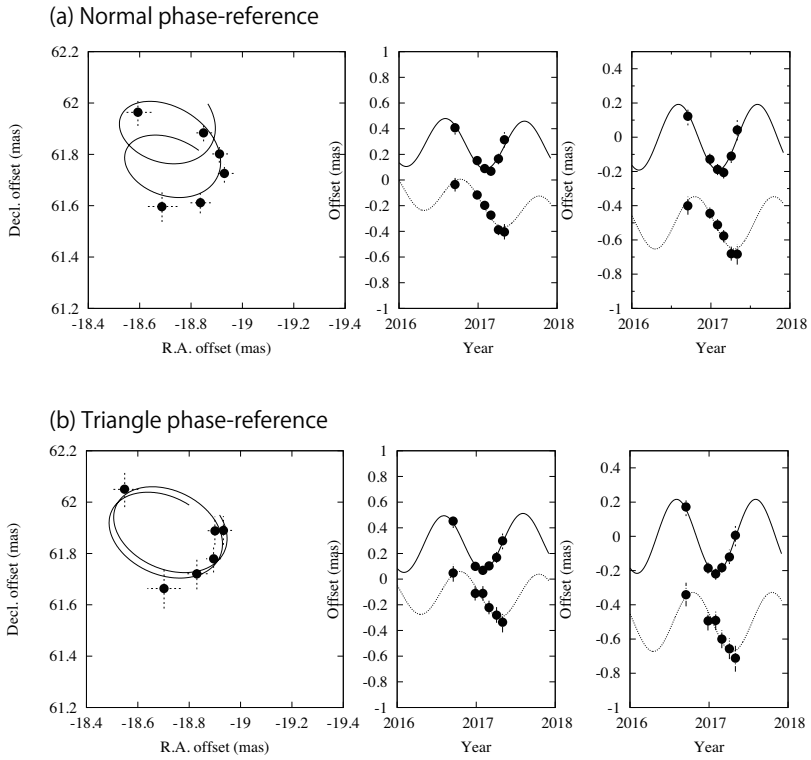

Figure 3.10: Comparison of the phase referencing observations. (a) the astrometric result for the normal and (b) the triangle phase referencing observations, respectively. (Left) : the position of G135.28+02.80 on the projected sky. (Center) : position of right ascension and declination as a function of time. (Right) : same as the center but with the proper motion subtracted.

- The systematic error specific in the triangle phase referencing is 37 μas from the standard deviation of the differences between positions obtained from the normal and triangle phase referencing observations. This is smaller than thermal errors of $\sim 50\,\mu$as which arise from weak flux densities of TM and PRQ relative to PRM.

- Fitting results of the parallax and proper motions obtained by the triangle phase referencing observations are consistent with those by the normal phase referencing within errors.

- The triangle phase referencing has an accuracy to measure parallaxes of sources whose distances are up to 5 kpc with errors of about 10%. We can distinguish the foreground and the Galactic center sources (8 kpc) with this accuracy in the Galactic center direction.

Table 3.8: Comparison of the phase referenced position between the normal and triangle phase referencing reduction for a maser source G135.28+02.80.

Source	Phase reference	Parallax (mas)	Proper motion $\mathrm{mas\,yr^{-1}}$	
G135.28+02.80	Normal	0.201 ± 0.029	-0.02 ± 0.09	-0.13 ± 0.11
	Triangle	0.227 ± 0.024	0.02 ± 0.07	-0.02 ± 0.11

Chapter 4 Astrometry of the Sgr D HII region

4.1 Introduction of the Sgr D HII region

4.1.1 Historical background

The Sgr D region is one of the largest radio continuum sources discovered through early radio observations in the direction of the Galactic center region. Very Large Array (VLA) radio continuum observations at 18 cm wavelength showed the detailed morphology of this source (Liszt 1992). Figure 4.1 shows a 6 cm radio continuum image of the Sgr D region taken with VLA (Mehringer et al. 1998). The Sgr D region consists of a compact source which is surrounded by diffuse emission extended with a diameter of $5'$. In addition to this compact source, they also detected another extended source located $5'$ to the south of this source. From the spectrum information, the northern source is an HII region which has weakly falling spectrum, while the southern source is a SNR which has a steep spectrum gradient. These sources were named as the Sgr D HII region (G1.13–0.10) to the north and the Sgr D SNR region (G1.05–0.15) to the south.

Recent X-ray observations obtained from *Suzaku* satellite have revealed another SNR behind the HII region (Sawada et al. 2009). It has been argued that the new SNR is located in or behind the Galactic center, because the feature of X-ray absorption was detected against a giant molecular cloud (GMC) in the Galactic center region, whose radial velocity is $\sim +100\,\mathrm{km\,s^{-1}}$.

4.1.2 Distance estimation for the Sgr D HII region

Although various observations have hinted at the distance to the Sgr D complex, no consistent agreement has been reached. In fact, the Sgr D HII region, the Sgr D SNR region, and the new SNR detected using *Suzaku* are probably just chance projections, and thus their distances differ. CS $J = 1$–0 molecular line emission has been detected towards the Sgr D HI I region with a line-of-sight velocity of $-16\,\mathrm{km\,s^{-1}}$ (Lis 1991). The detection of H91α radio recombination line emission at a similar line-of-sight velocity ($-21\,\mathrm{km\,s^{-1}}$) to that of the CS line emission indicates that the Sgr D HII region is physically associated with the CS core at $V_{\mathrm{lsr}} = -16\,\mathrm{km\,s^{-1}}$ (Anantharamaiah & Yusef-Zadeh 1989). Liszt (1992) also detected H70α recombination line emission towards the Sgr D HII region at $V_{\mathrm{lsr}} = -19.6\,\mathrm{km\,s^{-1}}$. Assuming that the Galaxy rotates circularly around the center, the line-of-sight velocity of the Sgr D HII region should be positive if it is located inside the solar circle. From this fact, some

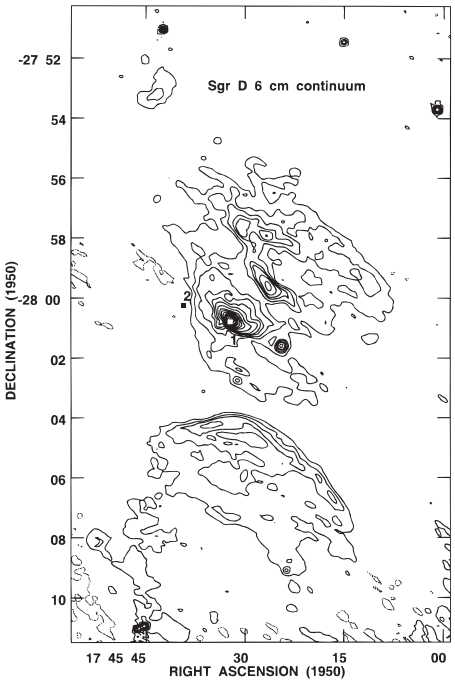

Figure 4.1: Radio continuum image toward the Sgr D region from Figure 9 of Mehringer et al. 1998.

studies concerning early observations have located Sgr D on the Galactic center, which has much more complex orbits than the disk (Kazes & Aubry 1973, Whiteoak & Gardner 1974). On the other hand, the narrow line width of the CS emission ($3.7\,\mathrm{km\,s^{-1}}$) suggests this is unlikely to be in the Galactic center region, because GMCs in the Galactic center region generally have a large velocity dispersion ($10 - 20\,\mathrm{km\,s^{-1}}$ FWHM) (Güsten 1989).

Mehringer et al. (1998) argued that the Sgr D HII region could be located in or beyond the Galactic center, based on the observed H_2CO absorption between +50 and $+100\,\mathrm{km\,s^{-1}}$ at the line-of-sight velocity. However, the $2\,\mu$m star count study showed a deficit of stars around the Sgr D HII region, indicating that the Sgr D HII region is located on the near side of the Galactic center, at a distance of approximately 3 kpc (Blum & Damineli 1999).

22 GHz H_2O maser emission has been detected towards the Sgr D HII region, with a velocity of $-20\,\mathrm{km\,s^{-1}}$ (Mehringer et al. 1998). It has been suggested that this water maser emission is associated with the Sgr D HII region.

In Chapter 4 and 5, we conducted astrometric observations using the inverse phase

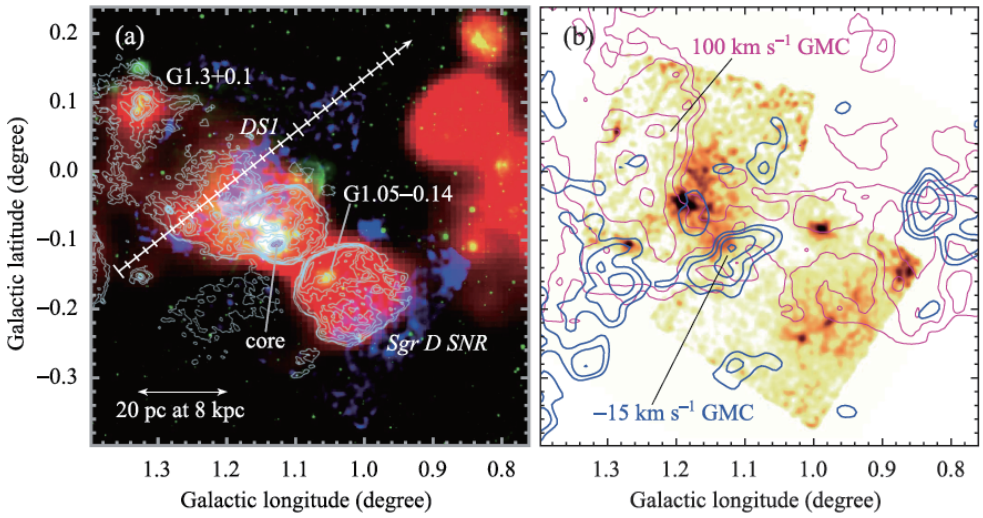

Figure 4.2: (a) Color image with *Suzaku* X-ray in blue, Spitzer MIR in green, and GBT radio in red. (b) X-ray image with CO (J = 3–2) emission in red contours and CS (J =1–0) emission in blue contours (Figure 6 of Sawada et al. (2009)).

referencing technique which could be applied to intense maser sources enough to detect their emission within short coherence time of about 1 minute. In this chapter, we report on astrometric observations of a water maser source towards the Sgr D HII region, obtained using VLBI Exploration of Radio Astrometry (VERA). Section 4.3 describes the maser distribution for this source, and astrometric results measured using the phase reference technique. In Section 4.4, we discuss the position and motions of this maser source in the Galaxy, based on the measured parallax and the absolute proper motions. Finally, we summarize our results in Section 4.5.

4.2 Observations

We conducted VLBI observations of water maser sources associated with the Sgr D HII region at a rest frequency of 22.235080 GHz using VERA, from 2008 to 2011. The number of observation epochs was three in 2008, one in 2009, four in 2010, and one in 2011. After the last epoch in 2011, the water maser source weakened, and cross correlation could not be detected. In each epoch, the on-source time for the Sgr D HII region was about 4.5 hours. In Figure 4.3, we showed the UV-coverage of the Sgr D HII region for Epoch 2. The UV-coverages for other observational epochs were similar to this. As a position

reference source, we observed J1745-2820 concurrently with the target maser source, using the dual-beam system of VERA. J1745-2820 was an extragalactic radio source, and its projected separation to Sgr D was 0.8°. NRAO530 was also observed for 10 min per every 45 min, to calibrate group-delay residuals. The phase tracking center positions for Sgr D and J1745-2820 were set to $(\alpha_{\rm J2000}, \delta_{\rm J2000}) = (17^{\rm h}48^{\rm m}48\overset{\rm s}{.}5450, -28°01'26.290'')$ and $(\alpha_{\rm J2000}, \delta_{\rm J2000}) = (17^{\rm h}45^{\rm m}52\overset{\rm s}{.}4968, -28°20'26.294'')$, respectively. These corresponded to $(l, b) = (1.14°, -0.13°)$ and $(0.54°, 0.26°)$ in the Galactic coordinates, respectively. Table 4.1 lists the dates of observations and the detected maser features. Among all nine epochs, we used five epochs to measure the parallax and absolute proper motions.

A data-recording rate of 1024 Mbps was adopted for the VERA DIR2000 recording system. The total bandwidth was 256 MHz, consisting of 16 IFs, which each had a bandwidth of 16 MHz. One IF was assigned to receive the maser emission, and the other 15 IFs were used to receive the continuum emission from J1745-2820. In our observations, the IF assigned to the target maser was divided into 512 spectral channels, which corresponded to a velocity resolution of $0.42\,{\rm km\,s^{-1}}$. For the continuum source, the IF bands were divided into 64 channels per 16 MHz sub-band. The correlation was carried out using the Mitaka FX correlator (Shibata et al. 1998) at the National Astronomical Observatory of Japan (NAOJ).

4.3 Data reduction

We analyzed our VLBI data using the Astronomical Image Processing System (AIPS) developed by the National Radio Astronomical Observatory (NRAO). For the bandpass calibration, a task BPASS was used on the bright calibrator NRAO530. The instrumental delay caused by the two different paths in the dual-beam system was calibrated by continuously measuring the phase difference from artificial noise sources into both beams (Honma et al. 2008). To calibrate the group delay, rate, and clock offset, a fringe search was conducted on NRAO530, and the solution was applied to both the target source and the position reference source. For the phase calibration, the solution of the fringe search for one maser spot of the target maser was applied to the position reference source (J1745-2820), because J1745-2820 was too weak (<100 mJy) to detect a solution of the fringe fitting. This procedure is referred to as *inverse* phase referencing, and followed Imai et al. (2012). The detailed process was summarized on Chapter 2. A spot at $-19.06\,{\rm km\,s^{-1}}$ was used as a reference spot for the epochs 5, 6, 7, 8, and 9. In the epochs 1, 2, 3, and 4, we could not obtain absolute positions of the maser spot at $-19.06\,{\rm km\,s^{-1}}$, because the spot was not bright at these epochs.

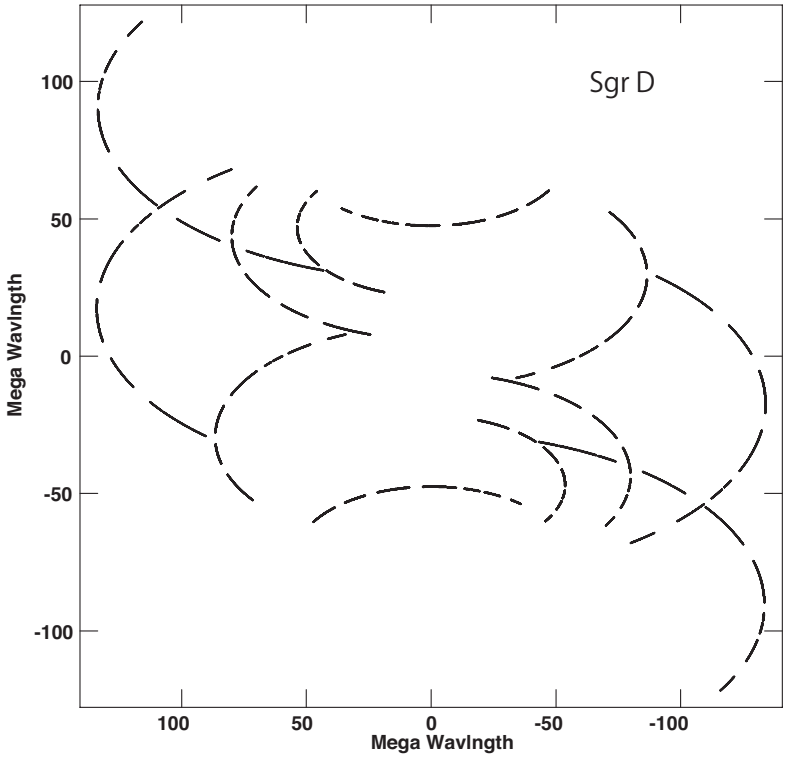

Figure 4.3: UV coverage for Sgr D in observations epoch 2.

For the single-beam imaging of Sgr D, the same solution of the fringe fitting for the spot at $-19.06\,\mathrm{km\,s^{-1}}$ was applied to all velocity channels. Thus, the relative positions of all maser spots were determined with respect to this reference spot. To estimate the relative motion of each spot, a linear least-squares analysis was applied to the spot as seen at the same velocity channel.

4.4 Results

4.4.1 Maser distribution

Figure 4.5 depicts the 22 GHz water maser distribution towards the Sgr D HII region at epoch 2, obtained from the single-beam imaging. The colors represent the line-of-sight velocities of each maser spot. The velocities of the maser spots range from $-26\,\mathrm{km\,s^{-1}}$ to $-6\,\mathrm{km\,s^{-1}}$. The projected scale of the maser distribution is about 100 mas from east to west, and about 30 mas from north to south. The systematic velocity of this source is $-16\,\mathrm{km\,s^{-1}}$ from the CS molecular line emission (Lis 1991). The blue-shifted feature group A is located on the west side of the maser distribution, while the red-shifted feature groups

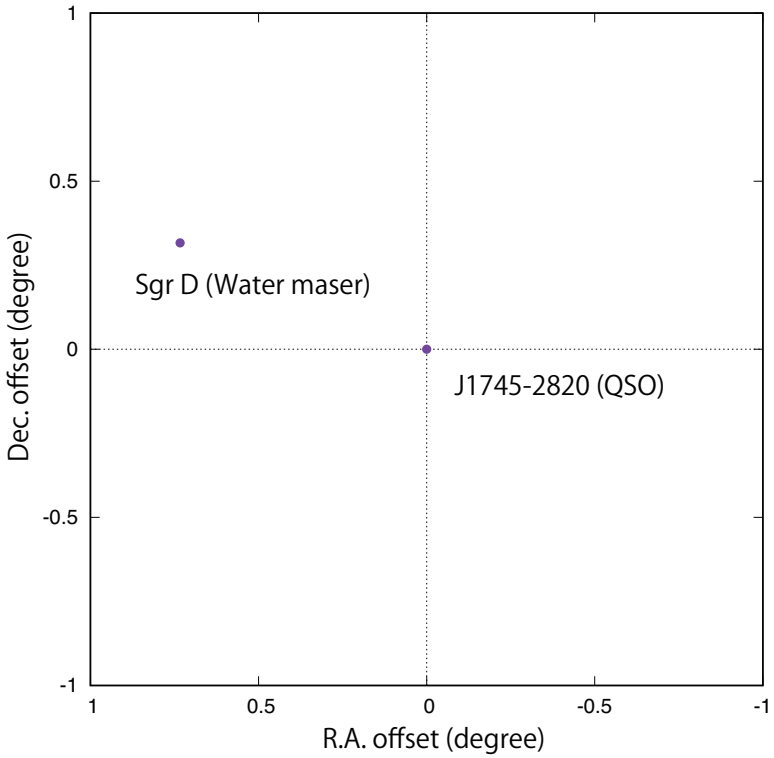

Figure 4.4: Relative position of a water maser in the Sgr D region with the position reference QSO.

B and C lie on the east side. The westernmost maser spot D exhibited a time variation, and was only detected at the epochs 1, 2, 8, and 9. The top two figures in Figure 4.5 are close-ups of the maser groups A, and B and C, respectively. In these figures, we see that the maser features are aligned on an arc-like morphology.

Figure 4.6 illustrates the internal proper motions for each maser feature. For the feature identification, we adopted a criterion in which spots coinciding in position ($\Delta\theta \leq 0.1\,\mathrm{mas}$) and velocity ($\Delta v \leq 1\,\mathrm{km\,s^{-1}}$) belong to the same maser feature. We identified 15 maser features under this condition. Internal motions were measured for features detected at more than three epochs by using least-squares fitting. The errors were then obtained from the least-squares analysis. The internal motions measured for each maser spot are summarized in Table 4.2. The colors of the arrows indicate line-of-sight velocity of each maser spot. Note that the internal motion of A5 was corrected in Figure 4.6, using the method described in Section 4.5.1. Features A, B, and C are moving away from each other, suggesting the existence of a jet from a star-forming region. Feature D was not detected in more than three

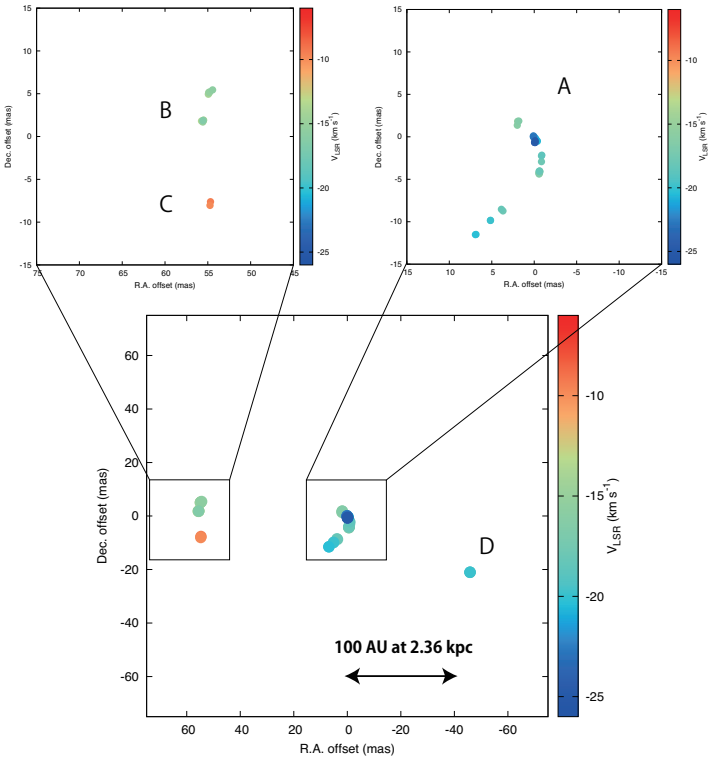

Figure 4.5: Distributions of water masers at epoch 2. Colors represent line-of-sight velocities of each maser spot. Top two panels are close up maps on feature group A, B, and C. 100 AU is corresponding to 42 mas at a distance of 2.36 kpc.

epochs with the same velocity channels. In feature group A, in particular, the direction of the internal motion of each feature is perpendicular to arc-like configuration of the feature group. Feature group C, which has the reddest features, moves towards the south. The outward velocity of the maser features in Figure 4.6 is 0.97 mas yr^{-1}. This gives 10.9 km s^{-1} upon adopting a distance of 2.36 kpc from the parallax measurement.

4.4.2 Annual parallax and proper motions

From phase-reference observations, we measured the parallax and absolute proper motions relative to the extragalactic source J1745-2820. The maser spot A5 at $V_{\rm LSR} = -19.06$ km s^{-1} was detected over five successive epochs between 2010 and 2011. The other spots could not be detected at more than four epochs by phase-reference observations. The positions of the maser spots in the phase-referenced map are affected by linear motions and the annual parallax. The detected positions are listed on Table 4.3. Then, we could derive the proper motions in right ascension, $\mu_\alpha \cos\delta$, and in declination, μ_δ, initial positions in

Table 4.1: Summary of observations and detected features. $V_{\rm ref}$ indicates the velocity of the spot that we use as a reference spot.

Epoch	Date	Beam (mas)	Detected features	$V_{\rm ref}$ ($\rm km\,s^{-1}$)
1	2008 May 27	1.96×0.71	A, B, D	–
2	2008 July 5	1.84×0.66	A, B C, D	–
3	2008 November 7	1.89×0.67	A	–
4	2009 September 21	2.17×0.67	A	–
5	2010 January 28	1.97×0.68	A, B, C	-19.06
6	2010 May 5	1.59×0.81	A, B, C	-19.06
7	2010 September 29	1.95×0.67	A, C	-19.06
8	2010 November 28	1.88×0.70	A, B, C, D	-19.06
9	2011 February 4	1.87×0.68	A, B, C, D	-19.06

right ascension ,α_0, and in declination ,δ_0, and the parallax, π, for the maser spot by using least-squares fitting. Figure 4.7(a) shows the projected motion of the maser spot. The direction of absolute proper motion goes from northeast to southwest. This is almost parallel to the Galactic plane. In Figure 4.7(b), the motion in the directions of R.A. and Dec. are shown as a function of time. By subtracting the expected linear motions from Figure 4.7(b), we obtained the parallax information shown in Figure 4.7(c).

The fitting results for this spot are listed in Table 4.4. The absolute proper motions towards R.A. and Dec. are $-1.32 \pm 0.15\,\rm mas\,yr^{-1}$ and $-2.86 \pm 0.34\,\rm mas\,yr^{-1}$, respectively. The large error in the direction of Dec. is due to the low elevation of the source, because the largest source of errors for phase-reference observations is the residual of the atmospheric zenith delay, and the amount of residual in the direction of Dec. is larger than in the direction of R.A. (Honma et al. 2008).

The obtained parallax value was 0.423±0.083 mas. This corresponds to $d = 2.36^{+0.58}_{-0.39}\,\rm kpc$ in the distance domain. The error bars of Figure 4.7 are 0.11 mas in right ascension and 0.26 mas in declination, respectively. This is derived by setting χ^2 per degree to be unity for both the right ascension and declination data.

4.5 Discussion

4.5.1 Peculiar motions

We converted the absolute proper motions to three-dimensional velocities with respect to the LSR by using the solar motion $(U_\odot, V_\odot, W_\odot) = (11.1, 12.24, 7.25)\,\rm km\,s^{-1}$ and the Galactic constants $(R_0, \Theta_0) = (8.34\,\rm kpc, 240\,km\,s^{-1})$, based on Schönrich, Binney, and Dehnen

Table 4.2: Positions and proper motions relative to the reference spot A5

Spot	$\Delta\alpha$ (mas)	$\Delta\delta$ (mas)	μ_α (mas/yr)	$\delta\mu_\alpha$	μ_δ (mas/yr)	$\delta\mu_\delta$	V_r ($\mathrm{km\,s^{-1}}$)
A1	−0.06	−0.06	0.38	0.07	0.37	0.07	−22.00
A2	−0.11	−0.09	0.40	0.09	0.31	0.06	−21.16
A3	0.14	−0.50	0.14	0.03	0.03	0.15	−20.32
A4	−0.06	−0.22	0.12	0.09	0.12	0.09	−19.48
A5	0.00	0.00	0.00	0.00	0.00	0.00	−19.06
A6	−0.30	−3.24	0.11	0.06	1.49	0.40	−18.64
A7	−0.91	−3.06	0.33	0.16	1.27	0.35	−18.22
A8	−0.66	−4.06	−0.13	0.12	−1.52	0.09	−16.54
A9	−0.67	−4.25	−0.31	0.28	−0.75	0.07	−15.91
B1	54.60	5.22	1.61	0.15	0.24	0.05	−15.70
B2	54.77	5.27	1.53	0.02	0.09	0.17	−15.28
B3	54.84	5.31	1.52	0.06	0.04	0.13	−14.86
C1	57.74	−8.03	0.89	0.04	−0.64	0.20	−7.30
C2	57.76	−8.17	0.99	0.03	−0.62	0.05	−6.88
C3	57.83	−8.17	0.82	0.07	−0.78	0.69	−6.04

Table 4.3: Absolute position measured by phase reference observation.

Epoch	R.A. position (mas)	Dec. position (mas)	$V_{\mathrm{ref}}\,\mathrm{km\,s^{-1}}$
5	-2.157	0.331	-19.06
6	-2.434	-0.834	-19.06
7	-3.814	-1.825	-19.06
8	-3.539	-1.856	-19.06
9	-3.548	-2.876	-19.06

(2010), Gillessen et al. (2009), Honma et al. (2012), and Reid et al. (2014). The absolute proper motion is the motion of the spot A5 with respect to the position reference source, J1745-2820, determined using dual-beam observations. The absolute proper motion consists of the solar motion, Galactic rotation, non-circular motion of the source, and internal motion of the spot A5. To illustrate the systematic motion of the source, we subtracted the internal motion of the maser feature from the absolute proper motion that we measured. The internal motion of the reference spot A5 was calculated by averaging the proper motions of all maser features. As a result, the internal motion was found to be $(\mu_\alpha \cos\delta, \mu_\delta) = (-0.56, 0.02)\,\mathrm{mas\,yr^{-1}}$. Thus, the systematic proper motion of the source in the Galactic system could be obtained as $(\mu_\alpha \cos\delta, \mu_\delta) = (-0.76, -2.88)\,\mathrm{mas\,yr^{-1}}$. Here, the

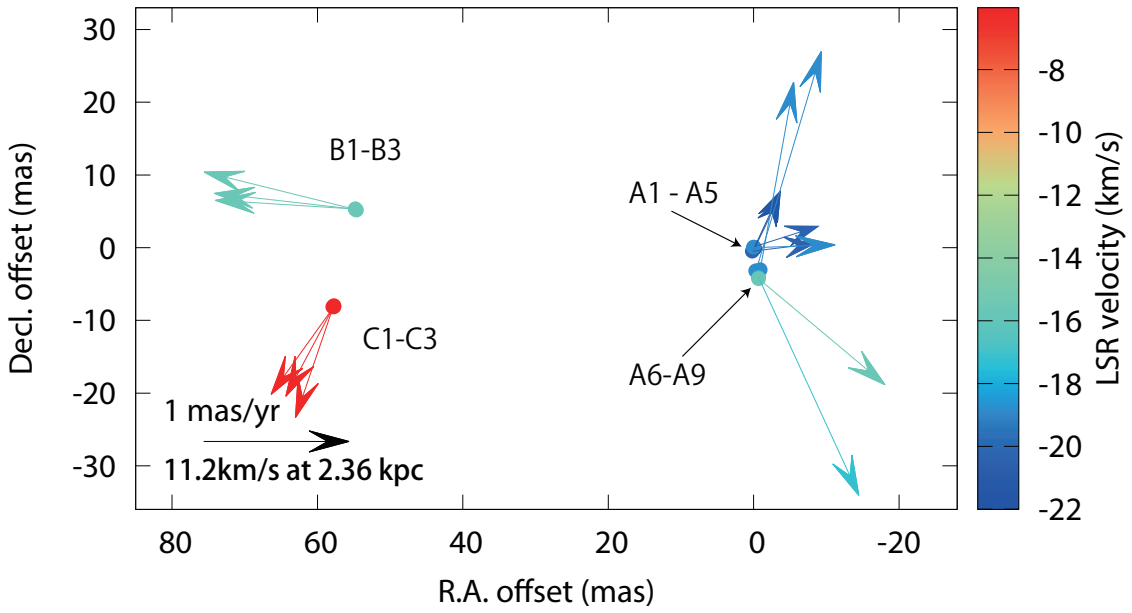

Figure 4.6: Internal motions of maser spots detected for more than three epochs. Colors of arrows represent line-of-sight velocities of maser spots. $1\,\mathrm{mas\,yr^{-1}}$ corresponds to $11.2\,\mathrm{km\,s^{-1}}$, at a distance of 2.36 kpc.

systematic proper motion is the sum of the solar motion, Galactic rotation, and non-circular motion of the source.

We converted the coordinates of the systematic proper motion to the Galactic coordinates by following the method of Reid et al. (2009), and obtained $(\mu_l \cos b, \mu_b) = (-2.86 \pm 0.30, -0.83 \pm 0.22)\,\mathrm{mas\,yr^{-1}}$. As a result, we obtained the non-circular motion of this source as $(U_s, V_s, W_s) = (-17.3 \pm 5.7, -20.5 \pm 6.4, -2.0 \pm 3.5)\,\mathrm{km\,s^{-1}}$. The errors of the non-circular motion were attributed to those of μ_l, μ_b, d, and V_{lsr}. Here, we set the error on V_{lsr} to $1.3\,\mathrm{km\,s^{-1}}$, from the standard error of the line-of-sight velocities of the maser spots in Table 4.2.

4.5.2 Location and kinematics in the Galactic scale

From the trigonometric parallax measurement, we obtained the distance of the maser source as $d = 2.36^{+0.58}_{-0.39}\,\mathrm{kpc}$. This distance suggests that the Sgr D HII region is located on the Scutum arm. Because the velocities of the water maser, CS molecular line, and H91α radio recombination line are similar (around $-16\,\mathrm{km\,s^{-1}}$), the water maser source is likely to be associated with the Sgr D HII region seen in radio continuum emissions.

Mehringer et al. (1998) argued that the Sgr D HII region is located at the far side of

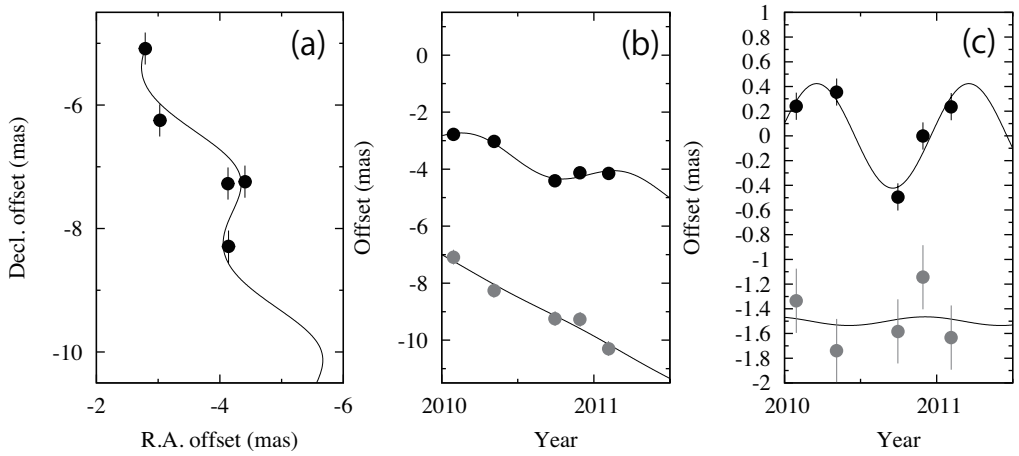

Figure 4.7: (a) Absolute proper motions of the maser feature A5 in the Sgr D HII region. Filled circles show the observed points from phase referencing. (b) Motions towards R.A. and Dec. as a function of time. Black circles show the motion in the R.A. direction, and gray circles show the motion in the Dec. direction. (c) Result of parallax fitting. Error bars are evaluated so that a χ^2 value in the model fitting becomes unity.

Table 4.4: Fitting result of parallax and proper motions for the spot A5 in the Sgr D HII region

	Best fit value	Error
Parallax	0.423 mas	0.083 mas
Proper motion (R.A.)	$-1.32\,\mathrm{mas\,yr^{-1}}$	$0.15\,\mathrm{mas\,yr^{-1}}$
Proper motion (Dec.)	$-2.86\,\mathrm{mas\,yr^{-1}}$	$0.34\,\mathrm{mas\,yr^{-1}}$

the Galactic center, by considering the H_2CO absorption feature at around $+100\,\mathrm{km\,s^{-1}}$, because the $+100\,\mathrm{km\,s^{-1}}$ cloud appears to be in the Central Molecular Zone (CMZ).

However, Sawada et al. (2009) found another SNR behind the HII region, from *Suzaku* X-ray observations. They located this SNR in or beyond the Galactic center region, through an extinction study. Mehringer et al. (1998) showed the existence of an H_2CO absorption feature from $+50\,\mathrm{km\,s^{-1}}$ to $+100\,\mathrm{km\,s^{-1}}$. This line-of-sight velocity differs from that of the Sgr D region by around $-20\,\mathrm{km\,s^{-1}}$, and corresponds to that of the GMC in the Galactic center region. In addition, Blum & Damineli (1999) argued that the Sgr D HII region is located on the near side of the Galactic center, by considering the NIR star count study. These facts suggest that continuum source inducing the H_2CO absorption is not the HII region, but rather the new SNR located on the far side of the Galactic center. If this new

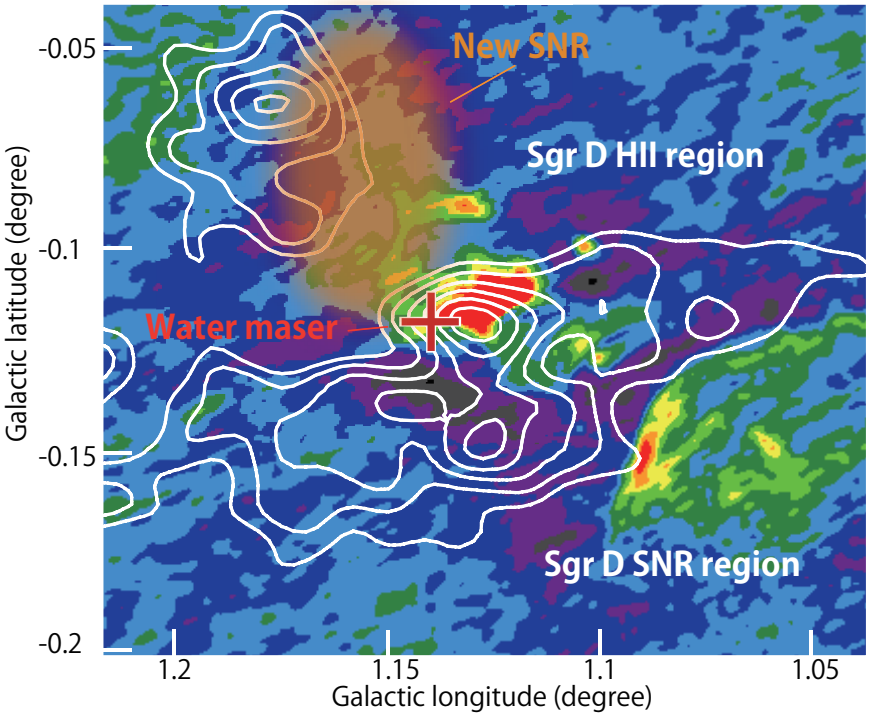

Figure 4.8: Radio continuum map around the SgrD complex taken with VLA at 6 cm (Mehringer et al. 1998). The white contours show the CS $J = 1$–0 molecular line emission at $-18\,\mathrm{km\,s^{-1}}$, observed with NRO 45m telescope (Tsuboi et al. 1999). The red cross shows the water maser source the parallax and proper motions of which we measured.

SNR is located on the far side of or in the Galactic center, it is not necessary that the Sgr D HII region is located on the far side. Note that this new SNR is not the Sgr D SNR region seen in the radio continuum map. Our result that the distance to the HII region is 2.36 kpc supports this picture.

Figure 4.8 presents a 6 cm radio continuum map taken using VLA (Mehringer et al. 1998). The white contours overlaying this map indicate CS $J = 1$–0 line emission at a $-18\,\mathrm{km\,s^{-1}}$ velocity with the NRO 45 m telescope (Tsuboi et al. 1999). The water maser position that we measured is represented by a red cross. The new SNR reported by Sawada et al. (2009) is represented by a brown ellipse.

Based on the discussion above, we propose the schematic view of the Sgr D HII region in Figure 4.9. The Sgr D HII region is located on the Scutum arm, on the near side of the Galactic center. The $+100\,\mathrm{km\,s^{-1}}$ cloud detected from CO observations is located on the CMZ in the Galactic center.

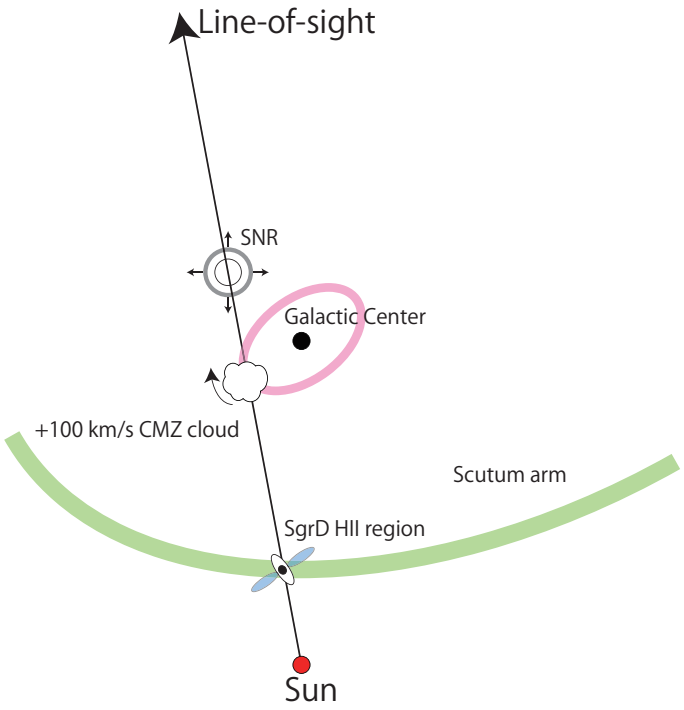

Figure 4.9: Schematic view of the Sgr D HII region.

While the peculiar motion of the water maser associated with the Sgr D HII region is directed outward from the Galactic center, other Scutum arm sources whose parallaxes and absolute proper motions have been measured have peculiar motions that are directed towards the Galactic center (Sato et al. 2014). On the other hand, the direction and magnitude of the peculiar motion of the water maser is similar to those of G005.88-00.39 in the Scutum arm (Sato et al. 2014). This source is the nearest one to Sgr D in the list given by Sato et al. (2014). The cause of the peculiar motion may be the proximity of the arm to the central bar. It is essential to accumulate sources whose parallaxes and proper motions are measured near to zero galactic longitude and negative galactic longitude in the Scutum arm in order to reveal the cause of peculiar motions, because the Scutum arm sources in Sato et al. (2014) have large dispersions on the non-circular motions $(\sigma_{Us}, \sigma_{Vs}, \sigma_{Ws}) = (16.7, 9.7, 6.0)\,\mathrm{km\,s^{-1}}$.

Another candidate source for large non-circular motion in the Sgr D HII region is the effect of the Sgr D SNR. However, the distance to the Sgr D SNR has not been measured, and it is not known for sure whether the Sgr D HII region and the SNR physically interact.

We need to investigate the environment of the Sgr D complex in further detail to clarify the relationships between each source.

4.6 Summary of chapter

We carried out an astrometric study of a water maser source associated with the Sgr D HII region, and obtained the trigonometric parallax and proper motions.

- The trigonometric distance of the maser source was 2.36 kpc. This is located on the Scutum arm. This is the first accurate distance measurement for the Sgr D HII region.
- The coincidence of the spatial position and line-of-sight velocity of the water maser with the H91α recombination line suggests that the maser source is physically associated with the Sgr D HII region.
- We demonstrated that we could distinguish the foreground source toward the Galactic center by using the inverse phase referencing observations.

Chapter 5 Astrometry of the Sgr B2 region

5.1 Introduction of the Sgr B2 complex

5.1.1 Previous studies

Sgr B2 is located at the inner 300 pc of the Galaxy referred as the Central Molecular Zone (hereafter CMZ). In 1980s, continuum observations of the Sgr B2 region with VLA depicted high resolution image of the HII region at 4885 MHz and 15, 015 MHz (Benson & Johnston 1984). Their image resolved three major components of Sgr B2 region known as Sgr B2M, N, and S associating twelve individual compact HII regions. Molecular line observations of ^{13}CO $J = 1$–0 emission detected morphological correlation between the Hole at $V_{\rm lsr} = 40$–50 km s^{-1} and the Clump at $V_{\rm lsr} = 70$–80 km s^{-1} (Hasegawa et al. 1994). They interpreted that the gas in the Hole has removed from large clouds at $V_{\rm lsr} = 40$–50 km s^{-1} by the Clump.

The position of the Sgr B2 region relative to Sgr A* is though to be near side from previous studies. Sawada et al. (2004) estimated the line-of-sight positions of molecular cloud toward the Galactic center region by using the ratio of OH 1667 MHz absorption to CO $J = 1$–0 emission. Because the Galactic center region itself is the strong continuum source at 1600 MHz band, if molecular clouds are located in front of the Galactic center, the OH spectra shows deep absorption feature. They derived the line-of-sight position of the Sgr B2 at the near side about Sgr A* by 100 pc. The orbital model proposed by Kruijssen et al. (2015) also indicated the position in front of Sgr A*. On the other hand, Molinari et al. (2011) suggested the position at the far side.

High resolution mapping toward the Sgr B2 region was conducted with VLA (De Pree et al. 2014). Figure 5.2 is the radio continuum image of the Sgr B2 complex at 22 GHz band. Sgr B2M at the center of the image and Sgr B2N located at about 45 arcsec north from Sgr B2M are sites of active massive star formation and are containing HII regions and X-ray sources. In the Sgr B2 complex, there are more than a hundred of 22 GH H_2O maser spots. Most of the maser spots are associated with the outside edge of the continuum emission from Sgr B2M and Sgr B2N at 22 GHz and 43 GHz bands (McGrath et al. 2004). They interpreted that the masers form in dense gas swept up by the stellar winds, or that the masers are associated with the molecular outflow from newly formed massive stars (Kuan & Snyder 1996, McGrath et al. 2004). Sanchez-Monge et al. (2017) shows ALMA image of

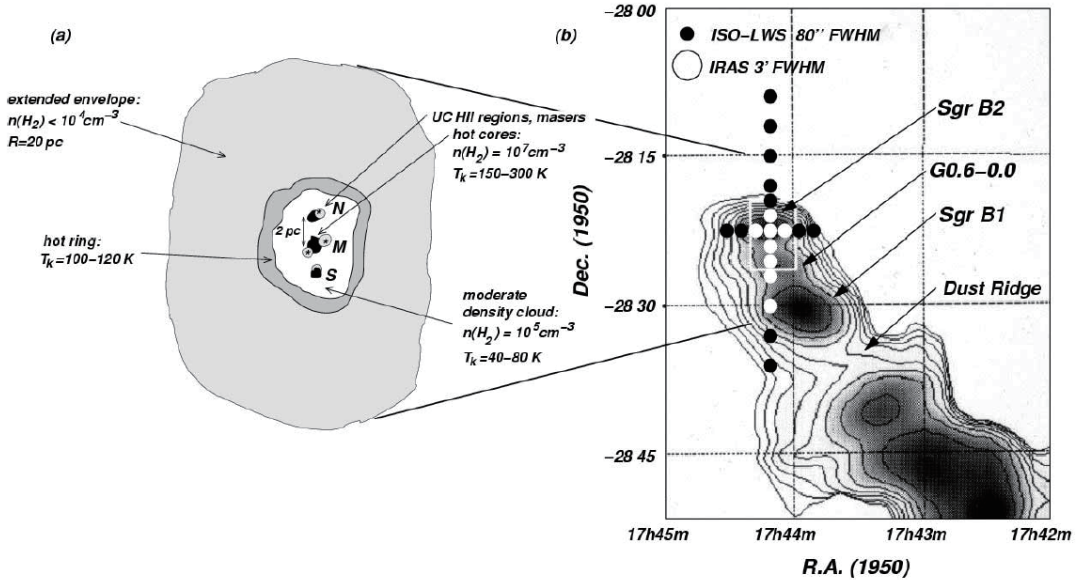

Figure 5.1: (a) Skech of the components in the Sgr B2 region. The Sgr B2 complex including Sgr B2M, N, and S are embedded in the exteded envelope. (b) Large-scale *IRAS* image at 60 μm (Gordon et al. 1993). (Fig.1 of Goicoechea et al. 2004.)

Sgr B2M and B2N at 240 GHz band. Major emission process in this band is dust continuum emission from spectral index study.

5.1.2 Trigonometric parallax measurement with VLBA

Measurement of trigonometric parallax for Sgr B2 have already conducted by VLBA observation (Reid et al. 2009). They monitored 22 GHz water maser sources in the Sgr B2N and B2M region from 2006 to 2007. Figure 5.3 shows astrometric results for Sgr B2M from Fig.2 of Reid et al. (2009). The line-of-sight velocities of the maser spots which they measured the parallaxes and proper motions are $V_{\rm lsr} = 66.4\,{\rm km\,s^{-1}}$ for Sgr B2M, and $V_{\rm lsr} = 56.7\,{\rm km\,s^{-1}}$ for Sgr B2N. Trigonometric parallaxes obtained for Sgr B2N and B2M were $\pi = 0.128 \pm 0.015\,{\rm mas}$ and $\pi = 0.130 \pm 0.012\,{\rm mas}$, respectively. They also measured absolute proper motions of these source relative to extragalactic source as $(\mu_\alpha \cos\delta, \mu_\delta) = (-0.32 \pm 0.05, -4.69 \pm 0.11)\,{\rm mas\,yr^{-1}}$ and $(\mu_\alpha \cos\delta, \mu_\delta) = (-1.23 \pm 0.04, -3.84 \pm 0.11)\,{\rm mas\,yr^{-1}}$, respectively. They estimated the distance offset along the line-of-sight from Sgr A*, $d \approx 0.13 \pm 0.06\,{\rm kpc}$ by using the measured proper motions. Here, they assumed that the distance to the Galactic center $R_0 \approx 8\,{\rm kpc}$ and the systematic line-of-sight velocity $V_{\rm lsr} \approx 62\,{\rm km\,s^{-1}}$, and that Sgr B2 belongs to a low eccentric orbit. The error of

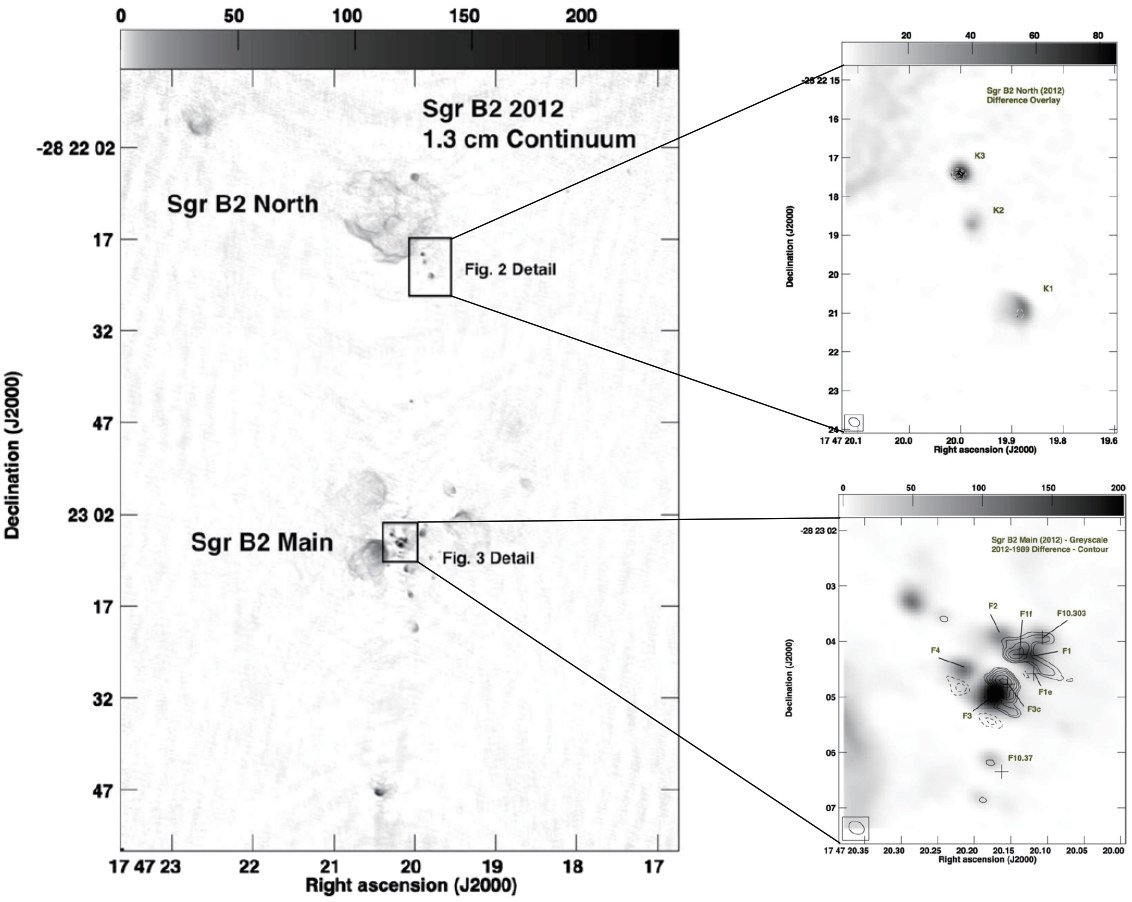

Figure 5.2: (Left) 22 GHz radio continuum image of the Sgr B2 complex from Fig. 1 of De Pree et al. (2014). (Top-right) Zoom-up image of Sgr B2N from Fig. 2 of De Pree et al. (2014). (Bottom-right) Zoom-up image of Sgr B2M from Fig.3 of De Pree et al. (2014).

d was attributed to the error associated with the proper motions of $\sim 1\,\mathrm{mas\,yr^{-1}}$ because their results didn't take account for the internal motions in the maser sources.

Thus, we have to correct the effect of internal motions of maser spot of which we measured absolute proper motions carefully to obtain the accurate position of Sgr B2 in the CMZ. The correction of the internal motions is also important for comparing predicted proper motions of Sgr B2 in the orbital models proposed by several authors (Molinari et al., Kruijssen et al. 2015).

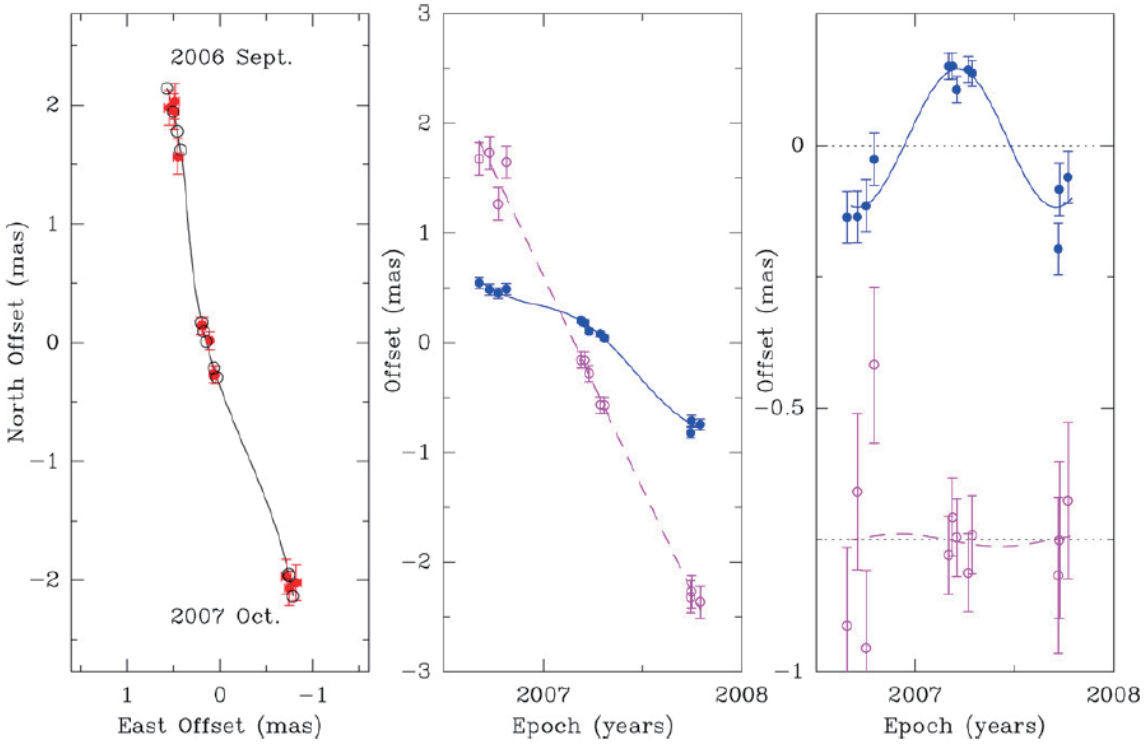

Figure 5.3: Parallax result for an H_2O maser spot of Sgr B2M at $V_{\rm lsr} = 66.4\,{\rm km\,s^{-1}}$ with VLBA (Figure 2 of Reid et al. 2009). Left: positions of the maser spot on the sky (red circles). Middle: positions in the direction of R.A.(blue) and Dec.(magenta) as a function of time. Right: same as the middle, but the linear motion has been removed.

5.2 Observations

VERA monitoring observations of 22.235080 GHz water masers in the Sgr B2 complex were made for 13 epochs between 2014 March and 2016 November. The observation dates was listed in Table 5.1. Sgr B2 was observed as the position reference maser (PRM) for G359.94-0.14 and G000.16-00.44 written in Chapter 6, therefore, the on-source time for Sgr B2 of approximately 1 hour is slightly short. Figure 5.4 shows the UV-coverage of Sgr B2. Sgr B2 and the position reference QSO, J1745-2820 whose separation angle of 0.33 deg. were simultaneously observed with the VERA dual-beam system. NRAO530 was observed for 10 min per every 90 min to calibrate group-delay residuals. The tracking center positions of Sgr B2 and J1745-2820 were $(\alpha_{\rm J2000}, \delta_{\rm J2000}) = (17^{\rm h}47^{\rm m}20\overset{\rm s}{.}18167, -28°23'3.8894'')$ and $(\alpha_{\rm J2000}, \delta_{\rm J2000}) = (17^{\rm h}45^{\rm m}52\overset{\rm s}{.}4968, -28°20'26.294'')$, respectively. We used ten epochs which is relatively good weather condition for the parallax measurement.

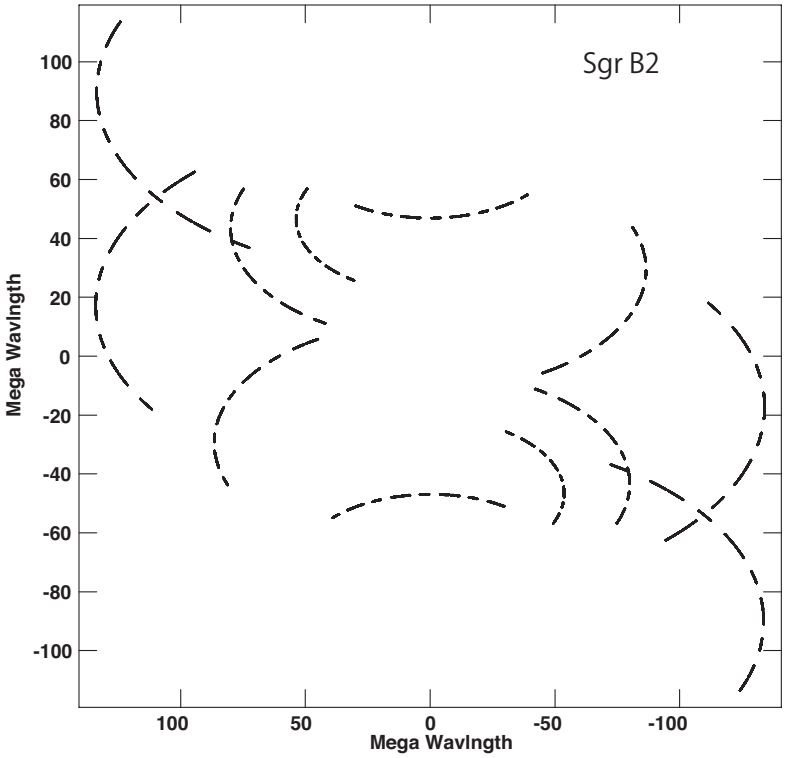

Figure 5.4: UV coverage for Sgr B2 in observations epoch 1.

Ten data was recorded at a rate of 1024 Mbps. As the recording systems, the magnetic tapes, DIR2000, was used for 2 epochs in 2014 and the hard disk, OCTADISK, was used for other 11 epochs after 2015. The correlations were carried out using the Mitaka hardware correlator for the data recorder in the magnetic tapes and the Mizusawa software correlator for data recorded in the hard disk. IF setting in the observations is the same with those of Sgr D in Chapter 4. The frequency resolution of the maser was 31.250 kHz ($0.42\,\mathrm{km\,s^{-1}}$) for first 4 epochs and 15.625 kHz ($0.21\,\mathrm{km\,s^{-1}}$) for the other 9 epochs.

5.3 Data reduction

We analyzed our VLBI data using the Astronomical Image Processing System (AIPS) developed by the National Radio Astronomical Observatory (NRAO). The process on the reduction is same between different recording systems. For the bandpass calibration, a task BPASS was used on the bright calibrator NRAO530. The instrumental delay caused by the two different paths in the dual-beam system was calibrated by continuously measuring the

Table 5.1: Summary of observations and detected features. $V_{\rm ref}$ indicates the velocity of the spot that we use as a reference spot.

Epoch	Date	$V_{\rm ref}$ ($\rm km\,s^{-1}$)
1	2014 March 29	59.58
2	2014 June 7	59.58
3	2015 March 26	59.58
4	2015 May 30	59.58
5	2016 January 16	59.58
6	2016 January 30	59.58
7	2016 April 1	59.58
8	2016 May 9	59.58
9	2016 May 10	59.58
10	2016 September 6	59.58
11	2016 September 7	59.58
12	2016 November 5	59.58
13	2016 November 19	59.58

phase difference from artificial noise sources into both beams (Honma et al. 2008). To calibrate the group delay, rate, and clock offset, a fringe search was conducted on NRAO530, and the solution was applied to both the target source and the position reference source. For the phase calibration, the solution of the fringe search for one maser spot of the target maser was applied to the position reference source (J1745-2820), because J1745-2820 was too weak ($< 100\,\rm mJy$) to detect a solution of the fringe fitting. This procedure is referred to as *inverse* phase referencing, and followed Imai et al. (2012). A spot at $59.58\,\rm km\,s^{-1}$ was used as a reference spot for all epochs.

For the single-beam imaging of the Sgr B2 complex, the same solution of the fringe fitting for the spot at $59.58\,\rm km\,s^{-1}$ was applied to all velocity channels. Thus, the relative positions of all maser spots were determined with respect to this reference spot. To estimate the relative motion of each spot, a linear-squares analysis was applied to the spot as seen at the same velocity channel.

5.4 Results

5.4.1 Maser distribution

Figure 5.5 shows the internal proper motions for each maser spot. The internal proper motions were measured for spots detected at more than four epochs by least-squares fitting. Finally, we obtained proper motions for 488 maser spots. The colors of the arrows indicate the line-of-sight velocity of each maser spot.

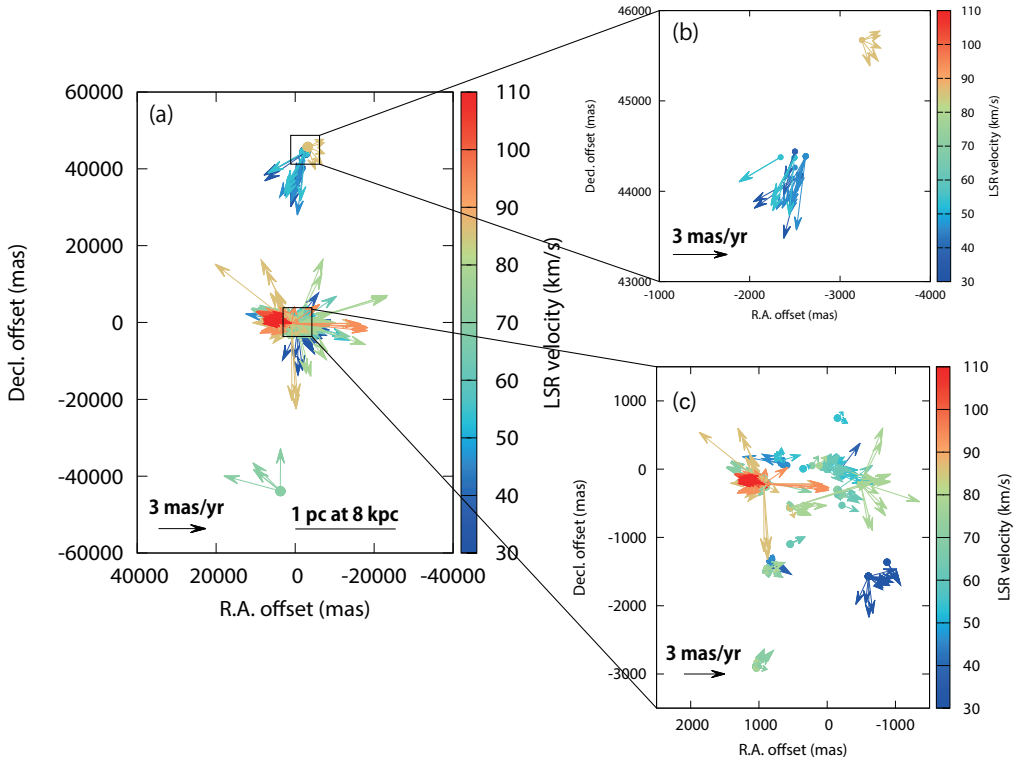

Figure 5.5: The distribution and internal motions of H_2O maser spots in the Sgr B2 complex detected for more than four epochs. Colors of arrows represent line-of-sight velocities of maser spots. $3\,\mathrm{mas\,yr^{-1}}$ is corresponding to $114\,\mathrm{km\,s^{-1}}$ when we assume the distance of the Sgr B2 complex at 8 kpc. (a) Whole distribution of water masers in the Sgr B2 complex. (b) Zoom-up of the Sgr B2N and (c) Zoom-up of the Sgr B2M.

Most of spots detected on our observations are associated with the Sgr B2M region which is located at the center of the map. In this region, maser spots extend over 2 arcsec and the line-of-sight velocities range from 30 to $110\,\mathrm{km\,s^{-1}}$. The redshifted spots are located at east side of the Sgr B2M region. These redshifted spots have relatively large internal motions of about $5\,\mathrm{mas\,yr^{-1}}$ than blueshifted spots whose internal motions is about $2\,\mathrm{mas\,yr^{-1}}$. The bluest spots are located at south-west in the map of Figure 5.5*c*. At 45 arcsec north from the Sgr B2M, we could detect maser spots associated with the Sgr B2N. In this region, maser spots are distributed in two different sites about 1 arcsec separeted with each other. The line-of-sight velocities of these spots are $80\,\mathrm{km\,s^{-1}}$ for the northern spots, and $50\,\mathrm{km\,s^{-1}}$ for the southern spots. At 45 arcsec south from the Sgr B2M, on the other hand, we detected some maser spots associated with the Sgr B2S region. These line-of-sight velocities are $70\,\mathrm{km\,s^{-1}}$. These maser spots in the Sgr B2S region could be originated from same maser

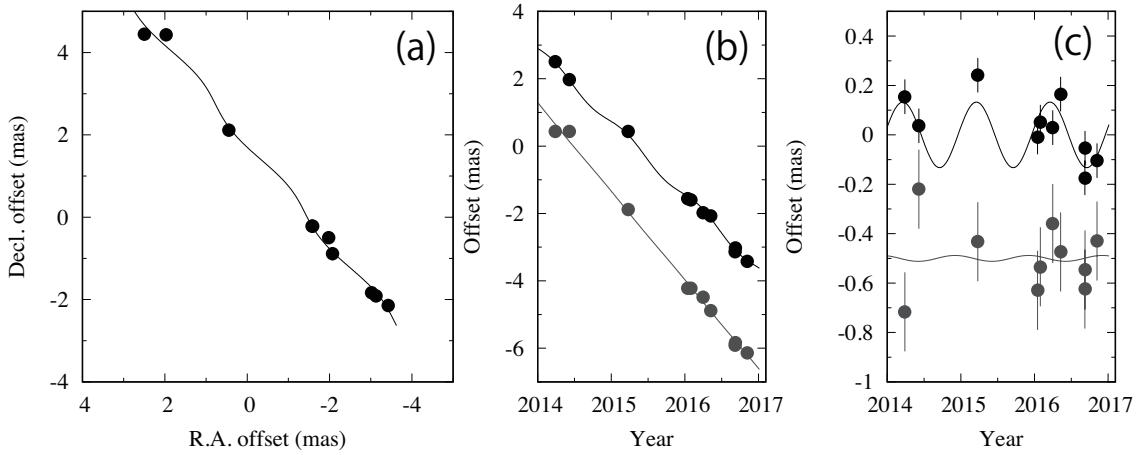

Figure 5.6: (a) Absolute proper motions of a maser spot in Sgr B2M at $V_{\rm lsr} = 59.58\,{\rm km\,s^{-1}}$. Filled circles show the observed points from phase referencing. (b) Motions towards R.A. and Dec. as a function of time. Black circles show the motion in the R.A. direction, and gray circles show the motion in the Dec. direction. (c) Result of parallax fitting. Error bars are evaluated so that a χ^2 value in the model fitting becomes unity.

feature. The positions and internal motions of the maser spots in Sgr B2M, B2N, and B2S relative to a reference spot are listed on Table 5.4, Table 5.5, and Table 5.6, respectively.

5.4.2 Annual parallax and proper motions

The parallax of Sgr B2M was obtained to be $0.133 \pm 0.038\,{\rm mas}$ ($7.52^{+3.01}_{-1.67}\,{\rm kpc}$) from the position measurement of the maser spot at $V_{\rm lsr} = 59.58\,{\rm km\,s^{-1}}$ with respect to the position reference QSO, J1745-2820. Figure 5.6 shows the positional variations of the maser spot at $V_{\rm lsr} = 59.58\,{\rm km\,s^{-1}}$ used for the parallax measurement. We can find a systematic sinusoidal motion with a period of 1 year and an amplitude of approximately 0.13 mas in the R.A. direction caused by the parallax. The positional errors of 0.07 in the R.A. and 0.16 mas in the Dec. were adjusted iteratively so as to make the reduced $\chi^2 \simeq 1$.

The parallax of Sgr B2M was also measured to be $0.130 \pm 0.012\,{\rm mas}$ by VLBA water maser astrometry (Reid et al. 2009). Our measured parallax is consistent with that of Reid et al. (2009) within the error. The error of VERA is approximately 3 times larger than that of VLBA. This would be due to the difference of the baseline length between VERA and VLBA. As shown in 2.13 in Chapter 2.1 equation, the positional error, $\Delta\theta$, the baseline length D, and the delay calibration error, $c\Delta\tau$ is $\Delta\theta = c\Delta\tau/D$. The maximum baseline length of VLBA (8,000 km) is 3.5 times longer than that of VERA (2,300 km). In the case that the delay calibration errors of VERA and VLBA are same, the positional error of

Table 5.2: Fitting result of parallax and the absolute proper motions for the spot at $59.58\,\mathrm{km\,s^{-1}}$ in the Sgr B2M region

	Best fit value	Error
Parallax	0.133 mas	0.038 mas
Proper motion (R.A.)	$-2.17\,\mathrm{mas\,yr^{-1}}$	$0.03\,\mathrm{mas\,yr^{-1}}$
Proper motion (Dec.)	$-2.63\,\mathrm{mas\,yr^{-1}}$	$0.06\,\mathrm{mas\,yr^{-1}}$

VERA is 3.5 times larger than the VLBA one.

The proper motion of the spot at $V_{\mathrm{lsr}} = 59.58\,\mathrm{km\,s^{-1}}$ with respect to J1745-2820 was obtained to be $(\mu_\alpha \cos\delta, \mu_\delta) = (-2.17 \pm 0.03, -2.63 \pm 0.06)\,\mathrm{mas\,yr^{-1}}$. This proper motion is the sum of the Galactic rotation motions of the LSR and source, the solar motion, the source peculiar motion, and the maser spot internal motion. Using this proper motion, we discuss about the location and kinematics of Sgr B2 in the Galactic center region.

5.5 Discussion

5.5.1 Location and kinematics in the Galactic scale

We converted the absolute proper motion to three-dimensional velocity with respect to the LSR by using the solar motion $(U_\odot, V_\odot, W_\odot) = (11.1, 12.24, 7.25)\,\mathrm{km\,s^{-1}}$ and the Galactic constants $(R_0, \Theta_0) = (8.34\,\mathrm{kpc}, 240\,\mathrm{km\,s^{-1}})$, based on Schönrich, Binney, and Dehnen (2010), Gillessen et al. (2009), Honma et al. (2012), and Reid et al. (2014). The absolute proper motion is the motion of the spot at $59.58\,\mathrm{km\,s^{-1}}$ with respect to the position reference source, J1745-2820, determined using dual-beam observations. The absolute proper motion consists of the solar motion, Galactic rotation, non-circular motion of the source, and internal motion of the spot. To illustrate the systematic motion of the Sgr B2M region, we subtracted the internal motion of the maser spot from the absolute proper motion that we measured. The internal motion of the reference spot at $59.58\,\mathrm{km\,s^{-1}}$ was calculated by averaging the proper motions of all maser spots including the Sgr B2M region which we measured with single-beam imaging. As a result, the internal motion of the spot at $59.58\,\mathrm{km\,s^{-1}}$ was found to be $(\mu_\alpha \cos\delta, \mu_\delta) = (-0.66 \pm 0.19, 0.81 \pm 0.13)\,\mathrm{mas\,yr^{-1}}$. The errors of the internal motion is calculated from the standard error of the proper motions for maser features associated with Sgr B2M. The standard deviation, σ, of the proper motions are $(\sigma_\alpha, \sigma_\delta) = (1.46, 0.99)\,\mathrm{mas\,yr^{-1}}$. Because the number of maser features associated with Sgr B2M is 58, the standard errors become $\sigma/\sqrt{58}$. Thus, the systematic proper motion of Sgr B2M could be obtained as $(\mu_\alpha \cos\delta, \mu_\delta) = (-1.51 \pm 0.19, -3.44 \pm 0.14)\,\mathrm{mas\,yr^{-1}}$ Here, the systematic proper motion is the sum of the solar motion, Galactic rotation, and

non-circular motion of the source. We converted the coordinates of the systematic proper motion to the Galactic coordinates by following the method of Reid et al.(2009), and obtained $(\mu_l \cos b, \mu_b) = (-3.72 \pm 0.22, -0.49 \pm 0.23)\,\mathrm{mas\,yr^{-1}}$. By subtracting the proper motion of Sgr A* by this motions, we can obtain the proper motions of Sgr B2 relative to Sgr A* as $(\mu_l \cos b, \mu_b) = (2.66 \pm 0.22, -0.29 \pm 0.23)\,\mathrm{mas\,yr^{-1}}$. Here,we used the proper motion of Sgr A* as $(\mu_l \cos b, \mu_b) = (-6.38 \pm 0.03, -0.20 \pm 0.02)\,\mathrm{mas\,yr^{-1}}$ from VLBA observations (Reid et al. 2004). The positive proper motion suggests that the Sgr B2 complex is located at the nearside of the Galactic center when we assume a low eccentric orbit of the CMZ. Adopting $R_0 \approx 8\,\mathrm{kpc}$ and $v_{\rm lsr} = 60\,\mathrm{km\,s^{-1}}$, the orbital velocity at Sgr B2 becomes $v_{\rm orb} = 132 \pm 14\,\mathrm{km\,s^{-1}}$.

Here, we compare the proper motions obtained by our VLBI observations with theoretical models. In expanding ring model, the Sgr B2 region with $V_{\rm lsr} \approx 60\,\mathrm{km\,s^{-1}}$ is located at the far side of the Galactic center (Scoville 1972). Thus, the proper motion of Sgr B2 in the direction of the Galactic longitude in this model becomes negative. This is not consistent with our results. Kruijssen et al. (2015) presented the predicted proper motions and orbital velocity of Sgr B2 in their open-orbit model as $(\mu_l \cos b, \mu_b) = (2.14^{+1.27}_{-2.08}, -0.75^{+0.45}_{-0.21})\,\mathrm{mas\,yr^{-1}}$ and $V_{\rm orb} = 124\,\mathrm{km\,s^{-1}}$, respectively. These values are quite similar to our results obtained by VLBI astrometric observations within errors. Here, note that Kruijssen et al. (2015) didn't include proper motions of Sgr B2 obtained by Reid et al. (2009) to construct their open-orbit model. In closed-orbit model proposed by Molinari et al. (2011), on the other hand, the predicted proper motions and the orbital velocities is $(\mu_l \cos b, \mu_b) = (0.57, -0.69)\,\mathrm{mas\,yr^{-1}}$, $V_{\rm orb} = 80\,\mathrm{km\,s^{-1}}$, respectively. Table 5.3 summarizes the proper motions of Sgr B2 relative to Sgr A* in our observations and orbital models. The values and errors of the open- and closed-orbit models are cited from Kruijissen et al. (2015) and Molinari et al. (2011). These values in closed-orbit model have large discrepancy from our observations and open-orbit model from Kruijssen et al. (2015). Although the predicted proper motion by Kruijssen et al. (2015) contains large errors, our results of proper motions and line-of-sight velocity with VERA prefer the large orbital velocity in the open-orbit model rather than the closed-orbit model. However, we have to observe a number of proper motions for the CMZ clouds to correctly constrain the orbital model of the CMZ.

5.6 Summary of chapter

We conducted VLBI monitoring observations of an H_2O maser source associated with the Sgr B2 complex. We succeeded to obtain the distribution and internal motions of maser

Table 5.3: Proper motions relative to the Galactic center obtained from observations and theoretical models.

	$\mu_l \cos b$	μ_b	$v_{\rm orb}$
Our observations	$2.66 \pm 0.22\,{\rm mas\,yr^{-1}}$	$-0.29 \pm 0.23\,{\rm mas\,yr^{-1}}$	$132 \pm 14\,{\rm km\,s^{-1}}$
Open-orbit model	$2.14^{+1.27}_{-2.08}\,{\rm mas\,yr^{-1}}$	$-0.75^{+0.45}_{-0.21}\,{\rm mas\,yr^{-1}}$	$124\,{\rm km\,s^{-1}}$
Closed-orbit model	$0.57\,{\rm mas\,yr^{-1}}$	$-0.69\,{\rm mas\,yr^{-1}}$	$80\,{\rm km\,s^{-1}}$

spots in detail. The positions of most of maser spots fall in the edge of HII regions detected by radio continuum observations. The internal motions tend to be directed to the outward of HII regions. This may suggest that the water masers form in the dense gas swept up by the stellar winds rather than in the molecular outflow.

We measured the parallax and proper motion of Sgr B2M as $\pi = 0.133 \pm 0.038\,{\rm mas}$ $(\mu_\alpha \cos\delta, \mu_\delta)$=$(7.52^{+3.01}_{-1.67}\,{\rm kpc})$. The positive proper motion toward the positive Galactic longitude clearly suggests the location of Sgr B2 at the nearside of the Galactic center. Our proper motions prefer the large orbital velocity in the open-orbit model rather than the closed-orbit model.

Table 5.4: Relative positions and motions of maser spots in Sgr B2M to a spot at $V_{\rm lsr} = 60.00\,{\rm km\,s^{-1}}$.

Spot	$\Delta\alpha$ (mas)	$\Delta\delta$ (mas)	μ_α (mas/yr)	$\delta\mu_\alpha$	μ_δ (mas/yr)	$\delta\mu_\delta$	$V_{\rm lsr}$ (km s^{-1})
1	−875.02	−1359.26	−0.24	0.07	−2.66	0.08	36.27
2	−875.32	−1360.21	−0.12	0.03	−2.25	0.04	36.48
3	−602.80	−1571.56	−0.44	0.06	−1.58	0.39	36.48
4	−875.25	−1359.86	−0.16	0.05	−2.39	0.13	36.69
5	−601.16	−1572.40	−1.25	0.04	−1.05	0.03	36.69
6	−602.70	−1571.70	−0.59	0.13	−1.34	0.30	36.90
7	−601.19	−1573.47	−1.34	0.03	−0.41	0.06	37.11
8	−602.64	−1571.76	−0.72	0.11	−1.16	0.33	37.32
9	−602.76	−1570.83	−0.69	0.02	−1.50	0.05	37.53
10	−602.75	−1571.56	−0.69	0.09	−1.19	0.19	37.74
11	−605.13	−1566.20	0.44	0.05	−3.70	0.09	37.95
12	−603.42	−1570.67	−0.30	0.17	−1.78	0.34	38.16
13	−605.67	−1565.81	0.73	0.08	−3.99	0.12	38.37
14	−603.44	−1570.57	−0.27	0.29	−1.94	0.17	38.58
15	−602.99	−1570.90	−1.04	0.23	−1.40	0.19	39.00
16	−606.84	−1567.69	0.99	0.08	−3.00	0.08	39.21
17	−603.24	−1570.66	−0.69	0.41	−1.64	0.19	39.42
18	−608.57	−1567.53	1.71	0.13	−3.03	0.07	39.63
19	−603.26	−1570.59	−0.77	0.44	−1.61	0.19	39.84
20	−196.42	−3.80	−0.66	0.05	0.96	0.30	40.47
21	833.00	−1345.34	−0.01	0.08	−1.49	0.10	41.10
22	833.93	−1344.99	−0.42	0.08	−1.63	0.05	41.31
23	834.30	−1344.60	−0.58	0.06	−1.80	0.05	41.52
24	834.72	−1344.18	−0.77	0.10	−1.95	0.02	41.73
25	830.46	−1349.49	0.54	0.06	−1.52	0.05	42.99
26	830.92	−1348.57	0.34	0.03	−1.48	0.03	43.20
27	830.45	−1348.90	0.54	0.02	−1.32	0.06	43.41
28	830.48	−1349.06	0.54	0.03	−1.25	0.08	43.62
29	830.69	−1348.96	0.45	0.05	−1.28	0.06	43.83
30	830.83	−1348.90	0.40	0.05	−1.28	0.06	44.04
31	830.77	−1348.77	0.43	0.02	−1.33	0.04	44.25
32	830.71	−1348.65	0.46	0.03	−1.38	0.04	44.46
33	830.77	−1349.20	0.44	0.02	−1.10	0.08	44.67
34	830.81	−1349.15	0.42	0.08	−1.09	0.07	44.88
35	830.59	−1350.35	0.58	0.08	−0.49	0.08	47.82
36	830.83	−1349.94	0.47	0.05	−0.67	0.04	48.03
37	830.76	−1350.11	0.51	0.06	−0.59	0.03	48.24
38	830.66	−1350.18	0.55	0.06	−0.57	0.04	48.45
39	589.84	57.34	2.58	0.71	−0.48	0.13	48.66
40	830.54	−1349.95	0.60	0.04	−0.67	0.03	48.66
41	830.56	−1349.84	0.60	0.03	−0.72	0.04	48.87
42	830.33	−1349.77	0.70	0.03	−0.75	0.03	49.08
43	830.58	−1349.15	0.59	0.03	−1.02	0.01	49.29
44	830.56	−1348.37	0.61	0.04	−1.36	0.01	49.50

Table 5.4: Relative positions and motions of maser spots in Sgr B2M to a spot at $V_{\rm lsr} = 60.00\,{\rm km\,s^{-1}}$.

Spot	$\Delta\alpha$ (mas)	$\Delta\delta$ (mas)	μ_α (mas/yr)	$\delta\mu_\alpha$	μ_δ (mas/yr)	$\delta\mu_\delta$	$V_{\rm lsr}$ (km s^{-1})
45	651.45	75.54	0.68	0.67	−0.49	0.02	52.02
46	644.91	75.34	3.73	0.42	−0.42	0.03	52.23
47	651.14	76.40	1.10	0.26	−0.94	0.15	52.44
48	648.53	74.87	2.27	0.07	−0.25	0.08	52.65
49	651.36	76.37	1.00	0.24	−0.99	0.19	52.86
50	677.76	124.10	1.23	0.01	−0.45	0.05	53.91
51	678.00	125.06	1.14	0.09	−0.91	0.10	54.12
52	678.24	123.78	1.05	0.01	−0.30	0.05	54.33
53	677.86	125.06	1.23	0.07	−0.87	0.13	54.54
54	679.03	123.28	0.71	0.06	−0.03	0.01	54.75
55	678.10	124.94	1.14	0.07	−0.78	0.13	54.96
56	678.99	123.83	0.76	0.05	−0.27	0.01	55.17
57	678.17	124.94	1.15	0.04	−0.78	0.12	55.38
58	678.32	124.36	1.09	0.03	−0.50	0.01	55.59
59	−220.27	−96.87	−0.22	0.03	−0.75	0.06	55.80
60	678.29	124.98	1.13	0.06	−0.80	0.13	55.80
61	−220.09	−96.15	−0.30	0.02	−1.06	0.01	56.01
62	−219.81	−96.51	−0.42	0.02	−0.88	0.07	56.22
63	685.31	123.49	−0.68	0.80	−0.57	0.15	56.22
64	−218.97	−94.99	−0.78	0.09	−1.54	0.08	56.43
65	−153.46	749.65	0.37	0.03	−0.53	0.11	56.64
66	−153.08	751.03	0.22	0.02	−1.14	0.06	56.85
67	−152.63	751.49	0.04	0.08	−1.35	0.05	57.06
68	5.60	3.96	−2.58	0.06	−1.85	0.06	57.27
69	0.92	0.06	−0.47	0.35	−0.09	0.31	57.48
70	5.89	4.63	−2.69	0.07	−2.12	0.05	57.69
71	0.53	0.16	−0.27	0.28	−0.10	0.24	57.90
72	3.34	2.33	−1.49	0.09	−1.05	0.08	58.11
73	0.23	−0.01	−0.08	0.16	0.02	0.12	58.32
74	350.12	9.68	0.69	0.09	−0.97	0.19	58.32
75	1.46	0.90	−0.63	0.06	−0.38	0.05	58.53
76	351.03	9.28	0.28	0.01	−0.77	0.06	58.53
77	0.31	0.25	−0.13	0.09	−0.10	0.10	58.74
78	350.02	9.77	0.79	0.06	−1.10	0.33	58.74
79	0.10	0.00	−0.03	0.03	0.01	0.03	58.95
80	0.22	0.17	−0.09	0.05	−0.08	0.07	59.16
81	−0.26	−0.31	0.12	0.01	0.15	0.02	59.37
82	0.09	0.06	−0.04	0.03	−0.02	0.03	59.58
83	−0.11	−0.13	0.05	0.01	0.06	0.01	59.79
84	0	0	0	0	0	0	60.00
85	0.08	0.15	−0.03	0.01	−0.07	0.01	60.21
86	−0.04	−0.07	0.02	0.03	0.04	0.04	60.42
87	0.21	0.21	−0.08	0.02	−0.09	0.01	60.63
88	0.07	−0.02	0.00	0.04	0.02	0.03	60.84

Table 5.4: Relative positions and motions of maser spots in Sgr B2M to a spot at $V_{\rm lsr} = 60.00\,{\rm km\,s^{-1}}$.

Spot	$\Delta\alpha$ (mas)	$\Delta\delta$ (mas)	μ_α (mas/yr)	$\delta\mu_\alpha$	μ_δ (mas/yr)	$\delta\mu_\delta$	$V_{\rm lsr}$ (km s^{-1})
89	0.23	0.18	−0.08	0.03	−0.07	0.01	61.05
90	0.05	0.04	0.01	0.04	−0.02	0.10	61.26
91	57.37	35.02	−0.77	0.02	−1.57	0.07	61.26
92	68.44	29.22	−1.32	0.09	−1.23	0.05	61.26
93	−0.02	−0.25	0.03	0.03	0.12	0.04	61.47
94	57.11	36.10	−0.64	0.06	−2.06	0.06	61.47
95	68.65	29.20	−1.43	0.03	−1.22	0.02	61.47
96	545.21	−1098.13	−0.33	0.07	−0.44	0.09	61.47
97	57.37	34.61	−0.75	0.03	−1.37	0.06	61.68
98	68.34	29.16	−1.31	0.02	−1.21	0.02	61.68
99	544.66	−1098.04	−0.11	0.05	−0.49	0.05	61.68
100	883.63	−202.57	1.52	0.04	−0.66	0.17	61.68
101	68.39	29.17	−1.35	0.02	−1.21	0.02	61.89
102	544.78	−1098.00	−0.17	0.04	−0.47	0.04	61.89
103	1.33	86.83	0.67	0.03	−0.66	0.13	62.10
104	68.31	29.18	−1.33	0.02	−1.24	0.01	62.10
105	544.77	−1097.82	−0.17	0.03	−0.53	0.04	62.10
106	883.69	−202.59	1.50	0.03	−0.63	0.09	62.10
107	68.06	29.12	−1.23	0.02	−1.21	0.01	62.31
108	544.83	−1097.88	−0.21	0.04	−0.48	0.05	62.31
109	−219.56	−529.17	−0.41	0.01	−1.41	0.31	62.52
110	1.36	86.70	0.63	0.04	−0.51	0.19	62.52
111	67.59	28.62	−1.04	0.02	−0.99	0.02	62.52
112	883.85	−202.75	1.39	0.06	−0.49	0.06	62.52
113	2.50	87.44	0.08	0.08	−0.70	0.04	62.73
114	884.65	−202.97	1.04	0.03	−0.38	0.07	62.73
115	1.57	86.48	0.48	0.10	−0.29	0.08	62.94
116	883.92	−202.88	1.36	0.07	−0.44	0.04	62.94
117	884.83	−202.59	0.95	0.05	−0.57	0.02	63.15
118	883.95	−202.77	1.35	0.08	−0.49	0.06	63.36
119	884.95	−202.65	0.90	0.04	−0.54	0.03	63.57
120	884.20	−202.96	1.23	0.11	−0.38	0.04	63.78
121	885.00	−202.58	0.88	0.04	−0.57	0.02	63.99
122	884.00	−203.19	1.35	0.13	−0.26	0.07	64.20
123	−164.46	−317.30	−0.44	0.06	−1.05	0.16	65.46
124	964.87	−165.03	1.32	0.13	−1.41	0.05	65.46
125	−163.82	−315.46	−0.74	0.12	−1.85	0.14	65.67
126	−163.15	−315.92	−1.04	0.04	−1.63	0.01	65.88
127	−147.69	−300.81	−1.82	0.26	0.82	0.43	65.88
128	−140.72	−305.22	0.17	0.04	−1.37	0.14	65.88
129	883.63	−206.31	1.27	0.06	−0.91	0.05	65.88
130	963.84	−165.79	2.23	0.50	−0.81	0.26	65.88
131	884.06	−207.41	1.08	0.04	−0.41	0.03	66.09
132	−155.18	−372.49	−0.66	0.10	−1.38	0.21	66.30

Table 5.4: Relative positions and motions of maser spots in Sgr B2M to a spot at $V_{\rm lsr} = 60.00\,{\rm km\,s^{-1}}$.

Spot	$\Delta\alpha$ (mas)	$\Delta\delta$ (mas)	μ_α (mas/yr)	$\delta\mu_\alpha$	μ_δ (mas/yr)	$\delta\mu_\delta$	$V_{\rm lsr}$ (km s^{-1})
133	883.57	−206.42	1.30	0.04	−0.85	0.03	66.30
134	964.34	−165.68	1.58	0.13	−0.93	0.13	66.30
135	883.90	−206.64	1.15	0.03	−0.75	0.04	66.51
136	−155.20	−372.55	−0.66	0.08	−1.18	0.16	66.72
137	−148.65	−299.69	0.52	0.16	−1.73	0.17	66.72
138	883.89	−206.00	1.16	0.05	−1.03	0.05	66.72
139	−148.61	−299.68	0.38	0.19	−1.60	0.13	67.14
140	963.36	−165.66	2.55	0.60	−1.00	0.26	67.56
141	−148.46	−299.74	0.10	0.06	−1.47	0.12	67.98
142	964.36	−165.10	1.51	0.08	−1.64	0.18	67.98
143	−148.58	−299.69	0.19	0.06	−1.51	0.09	68.40
144	964.41	−164.99	1.36	0.04	−1.82	0.20	68.40
145	976.61	−158.99	−2.96	0.79	−1.86	0.23	68.82
146	899.46	−256.46	0.97	0.04	0.01	0.04	69.03
147	898.71	−254.63	1.29	0.06	−0.80	0.12	69.24
148	899.40	−255.84	0.96	0.03	−0.24	0.04	69.45
149	898.63	−254.06	1.29	0.05	−1.05	0.19	69.66
150	899.35	−256.18	0.95	0.05	−0.05	0.05	69.87
151	219.63	52.03	0.32	0.03	−0.27	0.01	70.08
152	898.64	−253.83	1.28	0.06	−1.08	0.18	70.08
153	969.52	−160.10	3.23	0.26	−0.10	0.02	70.08
154	1007.14	−109.70	2.82	0.15	0.07	0.09	70.08
155	973.15	−159.94	1.61	0.05	−0.17	0.02	70.29
156	898.60	−253.56	1.39	0.11	−1.31	0.11	70.50
157	969.60	−160.30	3.21	0.25	−0.01	0.03	70.50
158	1007.36	−109.89	2.74	0.15	0.16	0.05	70.50
159	972.93	−159.99	1.72	0.03	−0.15	0.01	70.71
160	543.33	−559.76	0.87	0.05	−0.53	0.08	70.92
161	898.22	−251.09	1.90	0.43	−1.18	0.09	70.92
162	969.51	−160.36	3.25	0.26	0.01	0.03	70.92
163	1007.43	−109.95	2.74	0.13	0.19	0.07	70.92
164	543.75	−559.12	0.68	0.02	−0.82	0.05	71.13
165	972.74	−160.26	1.81	0.03	−0.04	0.03	71.13
166	543.88	−559.39	0.62	0.03	−0.69	0.03	71.34
167	889.35	−250.76	1.31	0.07	−1.45	0.10	71.34
168	969.37	−160.23	3.30	0.24	−0.06	0.02	71.34
169	543.80	−559.33	0.67	0.03	−0.72	0.01	71.55
170	899.07	−251.66	1.43	0.06	−1.14	0.06	71.55
171	972.92	−160.13	1.70	0.02	−0.11	0.01	71.55
172	543.68	−559.15	0.73	0.03	−0.80	0.02	71.76
173	899.35	−250.62	1.30	0.05	−1.66	0.04	71.76
174	1045.42	−2887.78	0.49	0.07	−0.92	0.14	71.76
175	543.78	−558.71	0.69	0.04	−1.01	0.02	71.97
176	973.57	−159.94	1.37	0.05	−0.22	0.02	71.97

Table 5.4: Relative positions and motions of maser spots in Sgr B2M to a spot at $V_{\rm lsr} = 60.00\,{\rm km\,s^{-1}}$.

Spot	$\Delta\alpha$ (mas)	$\Delta\delta$ (mas)	μ_α (mas/yr)	$\delta\mu_\alpha$	μ_δ (mas/yr)	$\delta\mu_\delta$	$V_{\rm lsr}$ (km s^{-1})
177	1039.38	−2898.90	0.19	0.04	0.33	0.06	71.97
178	1045.68	−2889.95	0.36	0.05	0.06	0.09	71.97
179	868.39	−1454.05	0.63	0.06	−1.28	0.09	72.18
180	973.64	−159.75	1.33	0.06	−0.31	0.02	72.18
181	1039.87	−2895.51	−0.02	0.06	−1.15	0.16	72.18
182	1045.48	−2887.71	0.44	0.05	−0.96	0.17	72.18
183	867.98	−1455.23	0.72	0.05	−0.74	0.17	72.18
184	973.65	−159.76	1.32	0.07	−0.31	0.01	72.39
185	1040.34	−2897.78	−0.20	0.07	−0.14	0.07	72.39
186	1045.76	−2889.91	0.32	0.05	0.02	0.07	72.39
187	868.30	−1454.13	0.46	0.08	−1.23	0.08	72.60
188	883.33	−1456.46	−0.39	0.15	−1.61	0.08	72.60
189	973.34	−159.98	1.46	0.07	−0.21	0.01	72.60
190	1040.05	−2895.45	−0.03	0.05	−1.14	0.15	72.60
191	868.96	−1455.84	0.11	0.09	−0.45	0.03	72.81
192	1040.60	−2897.22	−0.19	0.04	−0.29	0.08	72.81
193	872.53	−1454.93	0.69	0.21	−1.62	0.10	73.02
194	883.39	−1456.85	−0.26	0.13	−1.32	0.12	73.02
195	1038.70	−2911.39	−0.49	0.13	0.31	0.16	73.02
196	1039.55	−2895.69	0.36	0.07	−0.91	0.12	73.02
197	871.66	−1455.65	1.12	0.03	−1.30	0.02	73.23
198	883.67	−1458.41	−0.37	0.02	−0.62	0.02	73.23
199	1037.01	−2911.44	0.20	0.11	0.32	0.15	73.23
200	1040.13	−2897.21	0.14	0.02	−0.18	0.08	73.23
201	872.66	−1455.05	0.61	0.20	−1.54	0.04	73.44
202	883.31	−1457.25	−0.22	0.05	−1.12	0.09	73.44
203	1036.16	−2909.24	0.54	0.05	−0.65	0.15	73.44
204	1039.10	−2896.07	0.62	0.04	−0.67	0.13	73.44
205	872.16	−1455.33	0.82	0.06	−1.39	0.06	73.65
206	884.10	−1458.62	−0.56	0.04	−0.51	0.05	73.65
207	1036.23	−2910.67	0.51	0.08	0.00	0.08	73.65
208	117.19	52.82	0.23	0.07	−0.28	0.06	73.86
209	872.11	−1455.26	0.85	0.13	−1.39	0.05	73.86
210	883.34	−1457.29	−0.20	0.06	−1.10	0.09	73.86
211	1035.63	−2910.09	0.78	0.05	−0.28	0.07	73.86
212	883.81	−1458.46	−0.38	0.02	−0.57	0.04	74.07
213	550.10	−562.46	−5.23	0.06	0.93	0.09	74.91
214	549.93	−562.13	−5.16	0.12	0.79	0.02	75.12
215	−358.15	−49.56	−0.85	0.03	−1.47	0.01	75.33
216	549.84	−562.40	−5.19	0.32	0.94	0.16	75.33
217	−357.79	−49.47	−1.02	0.05	−1.50	0.04	75.54
218	542.53	−558.41	−1.93	0.55	−0.84	0.30	75.54
219	537.76	−557.03	−0.01	0.03	−1.36	0.04	75.75
220	539.47	−556.69	−0.71	0.52	−1.55	0.28	75.96

Table 5.4: Relative positions and motions of maser spots in Sgr B2M to a spot at $V_{\rm lsr} = 60.00\,{\rm km\,s^{-1}}$.

Spot	$\Delta\alpha$ (mas)	$\Delta\delta$ (mas)	μ_α (mas/yr)	$\delta\mu_\alpha$	μ_δ (mas/yr)	$\delta\mu_\delta$	$V_{\rm lsr}$ (km s^{-1})
221	538.89	−557.60	−0.50	0.06	−1.11	0.04	76.17
222	538.38	−556.62	−0.33	0.54	−1.56	0.09	76.38
223	539.71	−558.11	−0.85	0.09	−0.89	0.06	76.59
224	−496.16	−203.21	−0.79	0.14	−0.89	0.47	76.80
225	−486.75	−226.67	−0.88	0.20	3.19	1.01	76.80
226	538.38	−556.63	−0.33	0.58	−1.56	0.10	76.80
227	−489.04	−210.64	0.17	0.10	−4.26	0.24	77.01
228	539.97	−558.46	−0.97	0.10	−0.73	0.06	77.01
229	−496.12	−203.21	−0.83	0.11	−0.81	0.38	77.22
230	−486.87	−225.14	−0.81	0.17	2.22	1.10	77.22
231	538.43	−556.63	−0.40	0.67	−1.56	0.12	77.22
232	−488.45	−210.27	−0.12	0.10	−4.42	0.18	77.43
233	−496.11	−203.26	−0.85	0.06	−0.71	0.25	77.64
234	−487.55	−216.39	−0.53	0.10	−1.67	0.40	77.64
235	538.57	−556.74	−0.67	0.77	−1.46	0.09	77.64
236	−486.36	−212.66	−1.09	0.16	−3.32	0.25	77.85
237	951.32	−206.57	1.68	0.04	−0.04	0.03	77.85
238	−494.56	−202.78	−1.40	1.47	−0.85	0.83	78.06
239	−485.93	−219.06	−1.33	0.39	−0.34	0.63	78.06
240	951.22	−206.27	1.73	0.07	−0.17	0.05	78.06
241	−486.19	−213.82	−1.18	0.13	−2.81	0.19	78.27
242	941.74	−206.40	1.48	0.05	−0.12	0.03	78.27
243	−494.59	−202.70	−1.36	1.43	−0.92	0.90	78.48
244	−485.57	−219.44	−1.47	0.08	−0.22	0.38	78.48
245	928.00	−215.58	1.85	0.05	−0.09	0.01	78.48
246	951.48	−205.26	1.59	0.08	−0.68	0.13	78.48
247	927.82	−215.53	1.94	0.05	−0.11	0.03	78.69
248	951.60	−206.07	1.54	0.06	−0.31	0.02	78.69
249	−489.81	−199.54	−3.57	0.09	−2.36	0.08	78.90
250	927.27	−214.41	2.19	0.09	−0.62	0.07	78.90
251	951.69	−205.34	1.48	0.11	−0.68	0.13	78.90
252	928.01	−215.63	1.86	0.05	−0.08	0.05	79.11
253	951.49	−205.29	1.58	0.06	−0.67	0.01	79.11
254	927.11	−214.38	2.26	0.08	−0.64	0.10	79.32
255	928.02	−215.83	1.85	0.04	0.01	0.07	79.53
256	948.43	−209.15	1.42	0.07	−0.23	0.04	79.53
257	927.12	−214.26	2.25	0.10	−0.70	0.11	79.74
258	947.80	−208.34	1.70	0.07	−0.60	0.05	79.74
259	928.29	−215.79	1.72	0.03	−0.01	0.07	79.95
260	948.43	−209.21	1.42	0.07	−0.21	0.03	79.95
261	926.83	−214.04	2.38	0.15	−0.80	0.11	80.16
262	947.83	−208.33	1.68	0.06	−0.62	0.07	80.16
263	928.68	−215.44	1.55	0.02	−0.18	0.07	80.37
264	947.75	−209.36	1.70	0.07	−0.16	0.04	80.37

Table 5.4: Relative positions and motions of maser spots in Sgr B2M to a spot at $V_{\rm lsr} = 60.00\,{\rm km\,s^{-1}}$.

Spot	$\Delta\alpha$ (mas)	$\Delta\delta$ (mas)	μ_α (mas/yr)	$\delta\mu_\alpha$	μ_δ (mas/yr)	$\delta\mu_\delta$	$V_{\rm lsr}$ (km s^{-1})
265	926.82	−214.13	2.40	0.13	−0.76	0.11	80.58
266	948.29	−209.04	1.45	0.09	−0.30	0.02	80.58
267	928.35	−216.99	1.71	0.04	0.54	0.03	80.79
268	538.64	−556.92	0.48	0.11	−1.72	0.19	81.00
269	926.77	−214.27	2.44	0.12	−0.67	0.20	81.00
270	928.22	−218.01	1.78	0.04	1.01	0.03	81.21
271	926.83	−214.53	2.42	0.18	−0.57	0.30	81.42
272	928.29	−218.28	1.74	0.04	1.15	0.02	81.63
273	926.86	−214.71	2.40	0.21	−0.49	0.35	81.84
274	927.45	−217.97	2.11	0.05	1.01	0.12	82.05
275	926.71	−214.94	2.44	0.24	−0.42	0.39	82.26
276	926.12	−222.95	2.68	0.08	3.15	0.33	82.47
277	927.07	−214.49	2.19	0.27	−0.93	0.88	82.68
278	926.76	−221.95	2.35	0.34	2.49	1.03	82.89
279	927.47	−213.56	1.90	0.26	−1.68	0.62	83.10
280	931.07	−203.98	0.38	0.31	−5.88	0.46	83.31
281	927.45	−212.33	1.92	0.25	−2.25	0.63	83.52
282	930.70	−202.58	0.47	0.04	−6.56	0.10	83.73
283	927.16	−212.68	2.11	0.31	−1.97	0.68	83.94
284	930.19	−203.65	0.74	0.30	−6.00	0.42	84.15
285	926.46	−215.39	2.55	0.10	−0.38	0.37	84.36
286	925.02	−214.33	3.21	0.10	−0.93	0.17	84.57
287	926.45	−215.44	2.59	0.11	−0.39	0.46	84.78
288	907.52	−231.27	5.60	0.16	2.88	0.04	84.99
289	919.68	−221.54	1.69	0.69	−1.70	0.60	85.20
290	916.37	−224.44	1.30	0.04	−0.44	0.10	85.20
291	915.34	−223.45	1.77	0.04	−0.88	0.03	85.41
292	937.61	−211.21	1.84	0.05	−0.36	0.07	85.41
293	918.60	−222.67	2.77	0.10	−0.65	0.33	85.62
294	915.29	−222.95	1.79	0.03	−1.11	0.03	85.62
295	938.17	−211.10	1.60	0.05	−0.43	0.05	85.62
296	914.88	−222.57	1.98	0.04	−1.30	0.05	85.83
297	938.73	−211.43	1.34	0.04	−0.27	0.02	85.83
298	918.68	−222.57	2.52	0.09	−0.84	0.29	86.04
299	914.76	−222.82	2.03	0.04	−1.18	0.02	86.04
300	938.85	−211.24	1.29	0.07	−0.36	0.03	86.04
301	914.17	−222.43	2.29	0.07	−1.36	0.05	86.25
302	939.41	−211.35	1.01	0.09	−0.32	0.02	86.25
303	920.67	−221.84	−0.29	1.18	−1.58	0.31	86.46
304	940.12	−210.98	0.66	0.10	−0.49	0.02	86.46
305	940.46	−210.89	0.48	0.10	−0.54	0.02	86.67
306	918.57	−223.07	2.29	0.29	−0.67	0.36	86.88
307	940.17	−210.65	0.59	0.10	−0.65	0.04	86.88
308	938.80	−215.38	−3.44	0.56	−0.96	0.14	87.09

Table 5.4: Relative positions and motions of maser spots in Sgr B2M to a spot at $V_{\rm lsr} = 60.00\,{\rm km\,s^{-1}}$.

Spot	$\Delta\alpha$ (mas)	$\Delta\delta$ (mas)	μ_α (mas/yr)	$\delta\mu_\alpha$	μ_δ (mas/yr)	$\delta\mu_\delta$	$V_{\rm lsr}$ (km s^{-1})
309	939.73	−211.06	0.78	0.09	−0.47	0.01	87.09
310	919.64	−223.49	0.33	1.42	−0.84	0.26	87.30
311	939.26	−215.37	−3.63	0.56	−0.99	0.12	87.30
312	940.24	−212.41	0.56	0.12	0.10	0.03	87.30
313	939.89	−214.85	−4.09	0.40	−1.26	0.08	87.51
314	918.86	−222.53	1.48	0.30	−1.56	0.73	87.72
315	939.60	−215.02	−3.96	0.39	−1.18	0.08	87.72
316	918.91	−226.01	1.49	0.09	0.06	0.08	87.93
317	939.81	−214.38	−4.05	0.39	−1.44	0.11	87.93
318	918.10	−223.54	1.87	0.17	−1.10	0.24	88.14
319	933.37	−218.15	−1.04	1.06	0.26	0.24	88.14
320	917.81	−223.21	2.01	0.36	−1.70	0.29	88.56
321	917.15	−223.08	2.76	0.63	−1.61	0.42	89.82
322	917.13	−223.11	2.67	0.58	−1.48	0.37	90.24
323	913.03	−225.74	2.78	0.10	−0.14	0.10	92.13
324	912.73	−225.65	2.89	0.05	−0.20	0.03	92.34
325	913.96	−226.10	2.34	0.07	0.01	0.02	92.55
326	914.12	−224.73	2.28	0.08	−0.62	0.03	92.76
327	914.41	−225.97	2.13	0.06	−0.10	0.07	92.97
328	916.39	−224.41	1.32	0.26	−0.78	0.11	93.18
329	916.35	−224.47	1.46	0.28	−0.74	0.13	93.60
330	916.29	−224.46	1.53	0.29	−0.75	0.16	94.02
331	916.35	−224.43	1.39	0.34	−0.82	0.13	94.44
332	916.29	−224.43	1.30	0.21	−0.85	0.10	94.86
333	913.61	−225.83	2.47	0.07	−0.23	0.03	95.07
334	915.96	−224.17	1.43	0.30	−1.00	0.18	95.28
335	914.26	−225.18	2.19	0.04	−0.52	0.08	95.49
336	912.35	−225.88	3.01	0.07	−0.22	0.04	95.70
337	912.79	−225.69	2.81	0.06	−0.31	0.04	95.91
338	912.53	−225.97	2.91	0.09	−0.18	0.06	96.12
339	913.19	−225.86	2.64	0.17	−0.25	0.06	96.33
340	945.32	−204.62	2.49	0.03	−0.97	0.02	103.68
341	945.31	−204.49	2.49	0.01	−1.01	0.09	104.10
342	911.73	−227.89	1.92	0.08	−0.20	0.02	104.94
343	911.47	−227.39	2.05	0.09	−0.45	0.05	105.15
344	911.49	−227.26	2.02	0.10	−0.50	0.08	105.36
345	945.42	−204.63	2.38	0.10	−0.95	0.09	105.36
346	911.94	−227.23	1.82	0.08	−0.52	0.03	105.57
347	946.11	−204.80	2.09	0.12	−0.88	0.03	105.57
348	911.09	−226.72	2.22	0.07	−0.76	0.06	105.78
349	945.32	−204.79	2.45	0.10	−0.87	0.13	105.78
350	945.90	−205.50	2.19	0.07	−0.56	0.03	105.99
351	945.26	−205.05	2.47	0.08	−0.76	0.09	106.20
352	946.07	−205.57	2.11	0.07	−0.53	0.03	106.41

Table 5.4: Relative positions and motions of maser spots in Sgr B2M to a spot at $V_{\rm lsr} = 60.00\,{\rm km\,s^{-1}}$.

Spot	$\Delta\alpha$ (mas)	$\Delta\delta$ (mas)	μ_α (mas/yr)	$\delta\mu_\alpha$	μ_δ (mas/yr)	$\delta\mu_\delta$	$V_{\rm lsr}$ (km s^{-1})
353	945.33	−205.06	2.45	0.10	−0.75	0.06	106.62
354	946.10	−205.83	2.09	0.06	−0.41	0.03	106.83
355	945.30	−205.56	2.45	0.08	−0.52	0.02	107.04
356	946.12	−205.72	2.09	0.06	−0.45	0.06	107.25
357	945.26	−205.21	2.49	0.19	−0.68	0.13	107.46

Table 5.5: Relative positions and motions of maser spots in Sgr B2N to a spot at $V_{\rm lsr} = 60.00\,{\rm km\,s^{-1}}$ in Sgr B2M.

Spot	$\Delta\alpha$ (mas)	$\Delta\delta$ (mas)	μ_α (mas/yr)	$\delta\mu_\alpha$	μ_δ (mas/yr)	$\delta\mu_\delta$	$V_{\rm lsr}$ (km s^{-1})
1	−2559.48	44180.13	1.67	0.10	−4.47	0.98	33.54
2	−2562.91	44176.58	3.32	1.06	−2.79	1.46	33.96
3	−2563.45	44175.05	3.38	0.16	−2.43	1.42	34.38
4	−2501.36	44438.96	1.32	0.07	−2.55	0.95	42.78
5	−2501.34	44438.97	1.32	0.11	−2.51	0.93	43.20
6	−2501.36	44438.99	1.33	0.09	−2.50	0.92	43.62
7	−2501.41	44441.06	1.39	0.08	−3.43	1.00	44.04
8	−2620.21	44385.84	1.27	0.07	−2.60	0.86	46.56
9	−2620.10	44386.51	1.20	0.04	−2.81	0.79	46.98
10	−2620.18	44386.61	1.24	0.21	−2.86	0.79	47.40
11	−2620.80	44387.69	1.59	0.14	−3.43	0.77	47.82
12	−2620.62	44388.54	1.63	0.07	−3.97	1.01	48.24
13	−2619.64	44390.60	1.27	0.07	−5.07	1.06	48.66
14	−2620.17	44388.18	1.66	0.09	−4.18	1.01	49.08
15	−2621.76	44387.55	2.39	0.34	−3.90	0.84	49.50
16	−2621.57	44387.45	2.07	0.44	−3.84	0.83	49.92
17	−2621.21	44387.22	1.65	0.50	−3.78	0.86	50.34
18	−2621.12	44386.98	1.58	0.41	−3.68	0.89	50.76
19	−2621.21	44386.89	1.62	0.35	−3.66	0.86	51.18
20	−2621.78	44386.44	1.85	0.11	−3.54	1.08	51.60
21	−2499.28	44261.82	1.08	0.09	−1.70	1.89	52.86
22	−2494.21	44372.30	1.05	0.57	−4.17	1.06	54.12
23	−2494.04	44371.93	1.95	0.12	−3.90	0.79	54.54
24	−2341.68	44378.01	3.06	0.14	−2.34	0.90	55.80
25	−2393.97	44371.27	1.93	0.08	−3.11	0.74	56.22
26	−2341.60	44377.86	3.02	0.16	−2.30	0.90	56.22
27	−2494.10	44371.57	2.04	0.10	−3.55	0.61	56.64
28	−2493.95	44371.32	2.05	0.07	−3.62	0.88	57.06
29	−3241.82	45673.44	0.31	0.31	−2.41	1.27	81.84
30	−3241.21	45670.95	−0.22	0.21	−0.47	0.55	82.68

Table 5.5: Relative positions and motions of maser spots in Sgr B2N to a spot at $V_{\rm lsr} = 60.00\,{\rm km\,s^{-1}}$ in Sgr B2M.

Spot	$\Delta\alpha$ (mas)	$\Delta\delta$ (mas)	μ_α (mas/yr)	$\delta\mu_\alpha$	μ_δ (mas/yr)	$\delta\mu_\delta$	$V_{\rm lsr}$ (km s^{-1})
31	−3241.20	45671.37	−0.25	0.11	−0.70	0.57	83.10
32	−3241.20	45672.76	−0.13	0.21	−2.11	0.96	83.94
33	−3240.89	45671.77	−0.28	0.03	−1.40	1.01	83.36

Table 5.6: Relative positions and motions of maser spots in Sgr B2S to a spot at $V_{\rm lsr} = 60.00\,{\rm km\,s^{-1}}$ in Sgr B2M.

Spot	$\Delta\alpha$ (mas)	$\Delta\delta$ (mas)	μ_α (mas/yr)	$\delta\mu_\alpha$	μ_δ (mas/yr)	$\delta\mu_\delta$	$V_{\rm lsr}$ (km s^{-1})
1	3775.70	−43826.46	4.33	0.34	0.01	0.68	68.40
2	3784.62	−43829.46	0.74	0.92	1.79	0.72	68.82
3	3778.19	−43827.06	2.43	0.13	0.40	0.89	69.24
4	3778.17	−43827.16	2.45	0.13	0.44	0.91	69.66
5	3778.12	−43827.72	2.49	0.18	0.85	0.89	70.08

Chapter 6 Triangle phase-reference technique to the Galactic center source

6.1 Other water maser sources toward the Galactic center

In Chapter 4 and 5, we showed astrometric results of the water maser sources associated with Sgr D HII region and Sgr B2 region using the inverse phase referencing technique. As mentioned in Chapter 2, however, we have to observe a larger number of proper motions and parallaxes for maser sources toward the Galactic center region to distinguish wether the maser sources are actually located at central part of the Galaxy and to reveal the three dimensional kinematics of the CMZ. Thus, we developed the triangle phase referencing technique which can measure the absolute position of target weak maser sources by using another strong maser source around the targets in Chapter 3.

Large survey of water maser had been conducted by HOPS (H_2O southern Galactic Plane Survey) project using the Australia Telescope Compact Array (Walsh et al. 2011). In this survey, they detected a number of water masers. Intensities for most of masers were less than 10 Jy. Thus, we could not conduct astrometric observation toward these sources using the inverse phase referencing because we need more than 10 Jy to obtain fringe solutions for masers. By using the triangle phase referencing technique introduced in Chapter 3, we can conduct the astrometric observations for weaker maser source down to approximately 1 Jy.

As we mentioned on Section 3.1, the required conditions for the triangle phase referencing is following :

- An intense source (PRM) which can be detected within the coherence time of water vapor ($\sim$ 100sec at 22 GHz) is located close to a TM and PRQ in the projected sky.
- The separation angles between the PRM–TM and PRM–PRQ pairs should be within the range from 0.3° to 2.2° which is the range of the separation angle of the dual-beam system on VERA.
- The flux density of PRM has to have more than about 10 Jy if we assume the typical system noise temperature, $T_{\rm sys} = 200$ K, and on-source time of 2–3 hours.

When we apply the triangle phase referencing to the Galactic center direction, a water maser source associated with the Sgr B2M region is the best candidate of the PRM. Using

the Sgr B2M as a PRM, we can conduct the triangle phase referencing observations within the range of ($-1.53^\circ < l < 0.37^\circ$) and ($0.97^\circ < l < 2.87^\circ$) along the Galactic longitude because the Sgr B2M is located at $l = 0.67^\circ$. Thus, weak maser sources distributed over the CMZ can be detected and measured the parallaxes and proper motions when we conduct the triangle phase referencing using the Sgr B2M as a PRM.

One of the purposes of this chapter is to test the utility of the triangle phase referencing for the situation that both the PRQ and TM are weak to detect the signal within the coherent time toward the Galactic center because test observations for W3OH described in Chapter 3 used intense sources for the TM and PRQ as well as the PRM. Another purpose is to distinguish the foreground and the Galactic center sources for such a weak TMs by measuring trigonometric parallaxes and proper motions with the triangle phase referencing.

6.2 Sources

Here, we conducted monitor observations for two sources toward the Galactic center with triangle phase reference technique introduced in Chapter 3.

G359.94-0.14 is located at very vicinity of Sgr A*, the central radio source in the Galaxy. In the discovery, G359.94-0.14 identified as OH/IR star from the emission of 1612 GHz OH maser (Lindqvist et al. 1992). However, Sjouwerman et al. (2002) re-identified this source as Young stellar object (YSO) from the H_2O maser line spectrum. G359.94-0.14 should be a good candidate to measure the proper motion around the Sgr A* if this source is located at the Galactic center.

G000.16-00.44 is a star-forming region in which 6.7 GHz methanol maser is also detected (Caswell et al. 2010). The systematic line-of-sight velocity of $13.8\,\mathrm{km\,s^{-1}}$ suggested that G000.16-00.44 is located at the inner Galacxy ($R < 3\,\mathrm{kpc}$; Caswell et al. 2010). Due to large offset of the galactic latitude $b = -0.44^\circ$, this source is apart from the spatial distribution of dust and molecular gas in the CMZ. The range of the galactic latitude of the CMZ is about $-0.2^\circ < b < 0.2^\circ$ (See Figure 7.1). Thus, G000.16-00.44 probably does not associate with main stream of the CMZ. However, since water maser source in G000.16-0.44 had moderate flux density of a few Jy at the time of planning the observations, this source was suitable to test the availability of the triangle phase referencing observations toward the Galactic center region.

6.3 Observational information

Monitoring observations have been conducted for water maser sources associated with G359.94-0.14 and G000.16-00.44 at a rest frequency of 22.235080 GHz using VERA. These

Table 6.1: Summary of observations and detected features for G359.94-0.14. $V_{\rm ref}$ indicates the velocity of the spot that we use as a reference spot for the Sgr B2.

Epoch	Date	Detected features	$V_{\rm ref}$ ($\rm km\,s^{-1}$) of PRM
1	2014 March 29	A, B, C	59.58
2	2014 June 7	A, B ,C	59.58
3	2015 March 26	A	59.58
4	2015 May 30	–	59.58
5	2016 January 16	A, B, C	59.58
6	2016 April 1	B	59.58
7	2016 May 10	–	59.58
8	2016 September 7	C	59.58
9	2016 November 19	C	59.58

Table 6.2: Summary of observations and detected features for G000.16-00.44. $V_{\rm ref}$ indicates the velocity of the spot that we use as a reference spot for the Sgr B2.

Epoch	Date	Detected features	$V_{\rm ref}$ ($\rm km\,s^{-1}$) of PRM
1	2016 January 30	C	59.58
2	2016 May 9	C	59.58
3	2016 September 6	C	59.58
4	2016 November 5	A, B, C	59.58
5	2017 January 18	A, B	59.58
6	2017 February 9	A, B	59.58
7	2017 May 5	A, B	59.58

two sources were observed by using triangle phase reference technique introduced in Chapter 3. The observation dates for G359.94-0.14 and G000.16-00.44 are summarized on Table 6.1 and Table 6.2, respectively. Last columns of these tables represent the line-of-sight velocity of the reference spot for Sgr B2. In all observations, we used a maser spot at $V_{\rm ref} = 59.58\,\rm km\,s^{-1}$. This spots is the same spot used for astrometric observations of the Sgr B2 region described in Chapter 5.

The numbers of observation epochs were nine for G359.94-00.14, and seven for G000.16-00.44. G359.94-00.14 and G000.16-00.44 are observed as TM1 and TM2 which we want to measure the absolute position. PRM was Sgr B2, and PRQ was J1745-2820. In each epoch, the on-source time of the PRM–TM pair was 2 hour, while that for the PRM–PRQ was 1 hour 45 min.

NRAO530 was also observed for 10 min per every 90 min, to calibrate group-delay

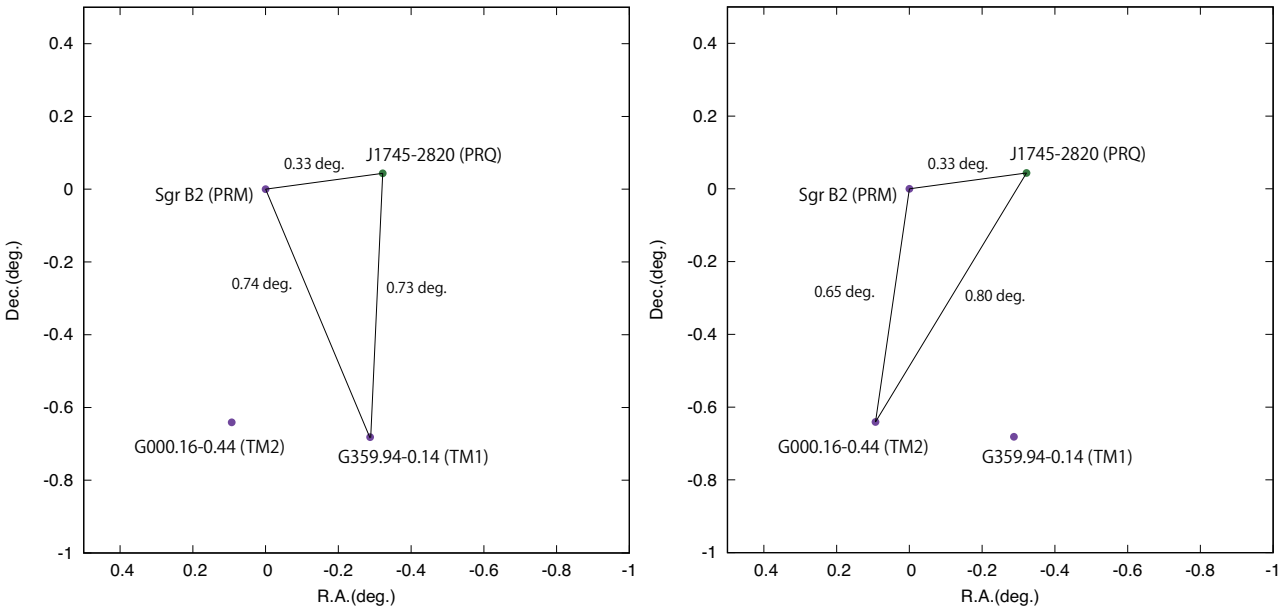

Figure 6.1: Relative position of the water maser sources and position reference QSO, Sgr B2 (PRM), G359.94-0.14 (TM1), G000.16-0.44 (TM2), and J1745-2820 (PRQ).

residuals. The tracking center positions for G359.94-0.14, G000.16-00.44, Sgr B2 and J1745-2820 were set as $(\alpha_{\rm J2000}, \delta_{\rm J2000}) = (17^{\rm h}46^{\rm m}1\overset{\rm s}{.}9227, -29^\circ3'58.787524'')$, $(\alpha_{\rm J2000}, \delta_{\rm J2000}) = (17^{\rm h}47^{\rm m}45\overset{\rm s}{.}4600, -29^\circ1'29.556000'')$, $(\alpha_{\rm J2000}, \delta_{\rm J2000}) = (17^{\rm h}47^{\rm m}20\overset{\rm s}{.}1182, -28^\circ23'3.795040'')$, $(\alpha_{\rm J2000}, \delta_{\rm J2000}) = (17^{\rm h}45^{\rm m}52\overset{\rm s}{.}49680, -28^\circ20'26.294000'')$, respectively. Table 6.3 lists the sources in these observatios. In Figure 6.1, we showed the relative positions and separation angles of these sources. J1745-2820 (PRQ) is 0.33 degree west from Sgr B2 (PRM). G359.94-0.14 (TM1) and G000.16-0.44 (TM2) are located at about 0.8 degree south from these PRQ and PRQ.

6.4 Results

6.4.1 G359.94-00.14

Figure 6.2 shows the results of astrometric observations for a maser spot in G359.94-00.14 at $V_{\rm lsr} = -19.8\,{\rm km\,s^{-1}}$ which is detected for four epochs. Unfortunately, the emission of H_2O maser from G359.94-00.14 has fade at early 2016. Thus, we fitted only absolute proper motion of the maser spot with fixed parallax of $\pi = 0.546$ mas and 0.125 mas. The value of parallax $\pi = 0.546\,{\rm mas}$ corresponding to 1.83 kpc was adopted from statistical parallax which we estimated at Section 6.5.1 ,while $\pi = 0.125\,{\rm mas}$ is corresponding to 8 kpc which is the distance to the Galactic center region. We conducted the fitting only for this

Table 6.3: The coordinates of sources in test observations.

Source	R.A. position	Dec. position	description	Separation angle
Sgr B2	17h47m20.1182s	-28d23m3.795040s	Reference maser	–
G359.94-00.14	17h46m1.9227s	-29d03m58.787524 s	Target maser 1	0.74 deg.
J1745-2820	17h45m52.4968s	-28d20m26.29400s	Position reference QSO	0.73 deg.
Sgr B2	17h47m20.1182s	-28d23m3.795040s	Reference maser	–
G000.16-00.44	17h47m45.600s	-29d01m29.556000 s	Target maser 2	0.65 deg.
J1745-2820	17h45m52.4968s	-28d20m26.29400s	Position reference QSO	0.80 deg.

Table 6.4: Positions and proper motions of water masers in G359.94-00.15 relative to the reference spot of Sgr B2M at $V_{\rm lsr} = 59.58\,{\rm km\,s^{-1}}$.

Spot	$\Delta\alpha$ (mas)	$\Delta\delta$ (mas)	μ_α (mas/yr)	$\delta\mu_\alpha$	μ_δ (mas/yr)	$\delta\mu_\delta$	V_r (km s^{-1})
A1	−33.20	90.79	0.18	0.31	1.83	0.29	−25.68
A2	−33.82	89.93	0.52	0.12	2.33	0.18	−24.00
B1	−15.74	117.96	0.80	0.12	1.91	0.31	−19.80
B2	−15.73	118.12	0.79	0.04	1.97	0.07	−19.38
C1	0.37	1.73	0.59	0.01	−1.67	0.57	8.76
C2	0.33	1.67	0.59	0.30	−1.68	0.65	8.34

spot because other five spots were detected only for three epochs. The measured absolute proper motion for this spot was $(\mu_{\rm RA}, \mu_{\rm Dec}) = (-1.67 \pm 0.20, -0.41 \pm 0.36)\,{\rm mas\,yr^{-1}}$ and $(\mu_{\rm RA}, \mu_{\rm Dec}) = (-1.69 \pm 0.26, -0.37 \pm 0.30)\,{\rm mas\,yr^{-1}}$ for $\pi = 0.546\,{\rm mas}$ and $\pi = 0.125\,{\rm mas}$, respectively. The error bars of Figure 6.2*a* and *b* are $(\sigma_\alpha, \sigma_\delta) = (0.27, 0.44)\,{\rm mas}$ and $(\sigma_\alpha, \sigma_\delta) = (0.38, 0.43)\,{\rm mas}$.

In Figure 6.3, we show the distribution and relative proper motions of water masers in G359.94-00.14. Water masers associated with G359.94-00.14 had substantial flux density, approximately 10 Jy, until early 2016. After mid 2016, the flux had decreased to about 1 Jy. With such weak flux, we cannot draw one-beam map which uses a strong maser spot as a phase reference spot. Thus, we measured the distribution and internal motions of maser spots in G359.94-00.14 by conducting phase-referencing from a maser spot at $V_{\rm lsr} = 59.58\,{\rm km\,s^{-1}}$ in the Sgr B2M region. The relative proper motions are calculated by least-squared fitting for spot detected over three epochs. We succeeded to detect the internal motions of three maser features. One maser feature with $V_{\rm lsr} = 8\,{\rm km\,s^{-1}}$ is located at south of the map, while two features around $V_{\rm lsr} = -20\,{\rm km\,s^{-1}}$ is located at 100 mas

Table 6.5: Parallax fitting results for G359.94-00.14 by triangle phase-referencing observations.

Source	Parallax (mas)	Proper motion $\mathrm{mas\,yr^{-1}}$		$V_{\rm lsr}$ ($\mathrm{km\,s^{-1}}$)
G359.94-00.14	0.546 (fixed)	-1.67 ± 0.20	-0.41 ± 0.36	-19.8
	0.125 (fixed)	-1.69 ± 0.26	-0.37 ± 0.30	-19.8

north from $5\,\mathrm{km\,s^{-1}}$ spot. Table 6.4 summarizes the positions and internal motions. The redder feature and bluer features are moving away with each other with internal motions of about $2\,\mathrm{mas\,yr^{-1}}$.

6.4.2 G000.16-00.44

Figure 6.4 is the astrometric results for G000.16-00.44 at 10.65 and $11.91\,\mathrm{km\,s^{-1}}$. Similar to the astrometric results for G359.94-00.14, relative positions of G000.16-0.44 were measured by subtraction of positions obtained from Sgr B2M(PRM) and J1745-2820(PRQ) pair by those from G000.16-00.44(TM) and J1745-2820(PRQ) pair. We could measure parallax and proper motions for eight maser spots associated with maser group A for which we could detected the maser spots for more than four epochs. Parallax was obtained by conducting combined fitting for all maser spots. Thus, one parallax value was calculated from eight spots datasets. The fitted parallax for G000.16-0.44 was $0.645 \pm 0.074\,\mathrm{mas}$. This is corresponding to $1.55^{+0.20}_{-0.16}\,\mathrm{kpc}$. Table 6.7 summarized the positions of maser spots and proper motions relative to PRQ. The maser positions were calculated by extrapolating the position at the begining of 2016 from the fitted parallax and proper motions. The errors of positions and proper motions are $(0.13, 0.15)\,\mathrm{mas}$ for the position errors and $(0.44, 0.48)\,\mathrm{mas\,yr^{-1}}$ for the errors of proper motions, respectively. These errors are common for all spots if we assume that the systematic error is dominant source of errors. As a example, we check this for a maser spot at $V_{\rm lsr} = 11.91\,\mathrm{km\,s^{-1}}$ at epoch 6. For this spot, the peak intensity obtained from phase-referenced image of Sgr B2 and G000.16-00.44 pair was $17\,\mathrm{Jy\,beam^{-1}}$ with rms noise level of $0.8\,\mathrm{Jy\,beam^{-1}}$. Then, the thermal error contained in this phase-referenced position is about $24\,\mu$as. On the other hand, thermal error associated with phase-referencing between Sgr B2 and J1745-2820 is $20\,\mu$as because the peak intensity and noise level are $36\,\mathrm{mJy\,beam^{-1}}$ and $1.8\,\mathrm{mJy\,beam^{-1}}$, respectively. According to discussion about thermal errors associated with triangle phase-referencing described on Chapter 2, the thermal errors of the position of G000.16-00.44 relative to J1745-2820 is $31\,\mu$as. Thus, dominant source of errors is systematic error common for all epochs because the thermal error is sufficiently small relative the systematic one.

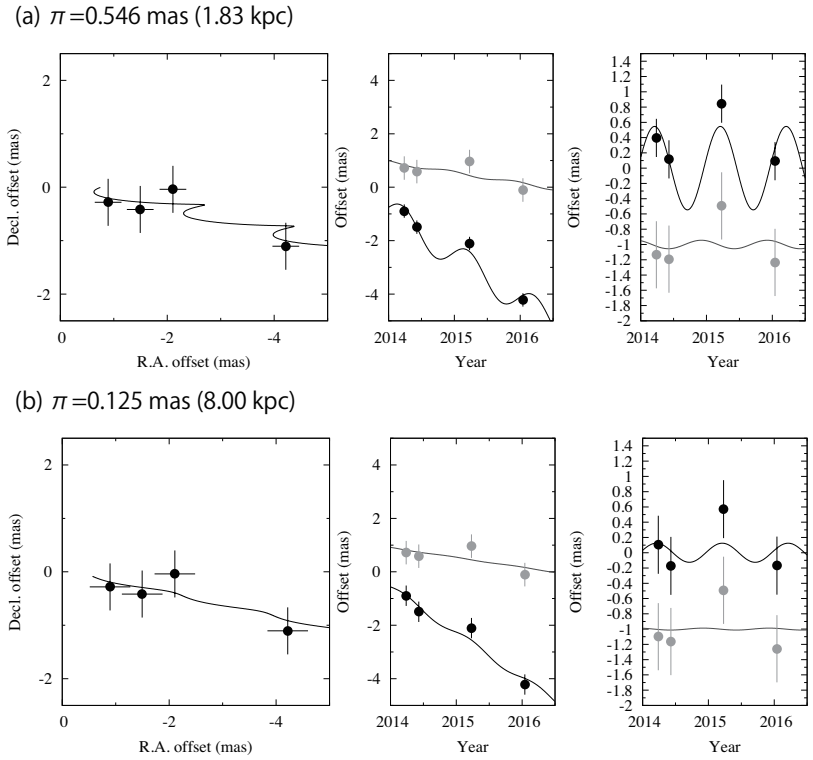

Figure 6.2: (a) and (b) are astrometric results of a water maser spot in G359.94-0.14 at $V_{\rm lsr} = -19.8\,{\rm km\,s^{-1}}$. (Left) Absolute proper motions of the maser feature in G359.94-00.14. Filled circles show the observed points from phase referencing. (Middle) Motions towards R.A. and Dec. as a function of time. Black circles show the motion in the R.A. direction, and gray circles show the motion in the Dec. direction. (Right) Result of parallax fitting. Error bars are evaluated so that a χ^2 value in the model fitting becomes unity.

Figure 6.5 shows the distribution and relative proper motions of water masers in G000.16-00.44. We measured the position and internal motions of maser spots in G000.16-00.44 by conducting phase-referencing from a maser spot at $V_{\rm lsr} = 59.58\,{\rm km\,s^{-1}}$ in the Sgr B2M region. The internal motions are calculated by least-squared fitting for spot detected over three epochs same way as the reduction for G359.94-0.14. We detected the relative proper motions of twelve maser spots associated with three two features. The line-of-sight velocities of maser spots are distributed from 10 to $13\,{\rm km\,s^{-1}}$. All spots are moving in the direction of east relative to the Sgr B2M. Average proper motion was $2.58\,{\rm mas\,yr^{-1}}$ and $0.56\,{\rm mas\,yr^{-1}}$ toward the direction of R.A. and Dec., respectively. Table 6.6 summarizes the positions and internal motions.

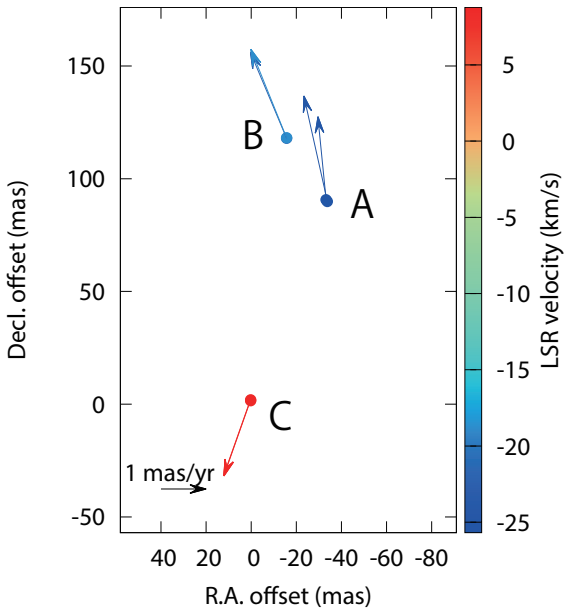

Figure 6.3: Proper motions of maser spots detected for more than three epochs in G359.94-00.14. Colors of arrows represent line-of-sight velocities of maser spots.

6.5 Discussion

Because the measured proper motion for spot B1 consists of the solar motion, Galactic rotation, non-circular motion of the source, and internal motion of the spot, we have to subtract the effect of internal motion. Proper motions listed in Table 6.4 is the motions relative to a spot in the Sgr B2. Thus, we estimated the motion of the dynamical center of G359.94-00.14 with respect to Sgr B2 by averaging the motions for each maser feature as $(\mu_{\rm RA}, \mu_{\rm Dec}) = (0.58 \pm 0.08, 0.78 \pm 0.16)\,{\rm mas\,yr^{-1}}$.

Thus, the internal motion of maser spot B1 at $-19.80\,{\rm km\,s^{-1}}$ is calculated as $(0.22 \pm 0.14, 1.13 \pm 0.35)\,{\rm mas\,yr^{-1}}$ by subtracting the motion of dynamical center from relative proper motion of spot B1 listed on Table 6.4. Then, the systematic proper motion, which is the sum of the solar motion, Galactic rotation, and non-circular motion of the maser source, is $(\mu_{\rm RA}, \mu_{\rm Dec}) = (-1.89 \pm 0.24, -1.54 \pm 0.50)\,{\rm mas\,yr^{-1}}$. When we convert this systematic proper motion in equatorial coordinate to the Galactic coordinate by the manner of Reid et al. (2009), we obtain $(\mu_l \cos b, \mu_b) = (-2.30 \pm 0.55, 0.81 \pm 0.47)\,{\rm mas\,yr^{-1}}$.

As mentioned on Section 6.4.1, we could not obtain sufficient data to measure the parallax of G359.94-00.14. Here, we discuss the proper motion and distance in the case of two candidates of distances. First candidate of distance can be estimated by using

Table 6.6: Positions and proper motions of water masers in G359.94-00.14 relative to the reference spot of Sgr B2M at $V_{\rm lsr} = 59.58\,{\rm km\,s^{-1}}$.

Spot	$\Delta\alpha$ (mas)	$\Delta\delta$ (mas)	μ_α (mas/yr)	$\delta\mu_\alpha$	μ_δ (mas/yr)	$\delta\mu_\delta$	V_r (km s^{-1})
A1	−1.61	1.01	3.05	0.06	−0.55	0.13	10.23
A2	−1.22	−0.06	2.67	0.07	0.37	0.18	10.44
A3	−0.98	−0.18	2.45	0.10	0.55	0.17	10.65
A4	−1.15	−0.16	2.59	0.10	0.51	0.16	10.86
A5	−1.22	−0.36	2.68	0.08	0.70	0.17	11.07
A6	−1.35	−0.43	2.81	0.08	0.78	0.18	11.28
A7	−1.54	−0.46	3.06	0.05	0.80	0.31	11.49
B1	−2.43	−0.29	2.70	0.22	0.34	0.21	11.70
B2	−2.40	−0.43	2.66	0.18	0.48	0.18	11.91
C1	11.58	−6.43	1.45	0.06	1.26	0.25	11.91
B3	−2.33	−0.63	2.60	0.18	0.68	0.17	12.12
B4	−2.11	−0.66	2.28	0.04	0.77	0.17	12.33

statistical parallax method (Genzel et al. 1981). This method estimates the distance D by the equation

$$D = \frac{\sigma_{v_z}}{\sigma_\mu} \qquad (6.1)$$

when we assume all the maser spots expands spherically with constant velocity. Here, σ_{v_z} and σ_{v_μ} is the velocity dispersion for the radial velocity and the dispersion of the proper motions, respectively. According to the velocities of water masers which we detected and OH masers in Lindqvist et al. (1992), we set the systematic radial velocity as $-12.0\,{\rm km\,s^{-1}}$. Then, the radial velocity dispersion of water masers is $15.3\,{\rm kms^{-1}}$. The dispersion of the proper motions is calculated as $1.76\,{\rm mas\,yr^{-1}}$ by using proper motions on Table 6.4 and the motion of the dynamical center. The estimated distance by statistical parallax is $1.83 \pm 0.65\,{\rm kpc}$. This statistical parallax and its errors are calculated based on Schneps et al. (1981). This distance is corresponding to the Sagittarius arm of the Galaxy. When we assume this distance, the non-circular motion can be calculated as $(U_s, V_s, W_s) = (-19.7 \pm 0.42, -7.71 \pm 4.79, 14.4 \pm 4.05)\,{\rm km\,s^{-1}}$. Here, we used the solar motion $(U_\odot, V_\odot, W_\odot) = (11.1, 12.24, 7.25)\,{\rm km\,s^{-1}}$ and the Galactic constants $(R_0, \Theta_0) = (8.34\,{\rm kpc}, 240\,{\rm km\,s^{-1}})$ (Gillessen et al. 2009, Reid et al. 2014). The errors were attributed to those of μ_l, μ_b and $V_{\rm lsr}$. The error of V_{lsr} is applied as $0.42\,{\rm km\,s^{-1}}$ from the range of velocities of the maser spot.

Second distance is 8 kpc which is the distance to the Galactic center. We could not rule

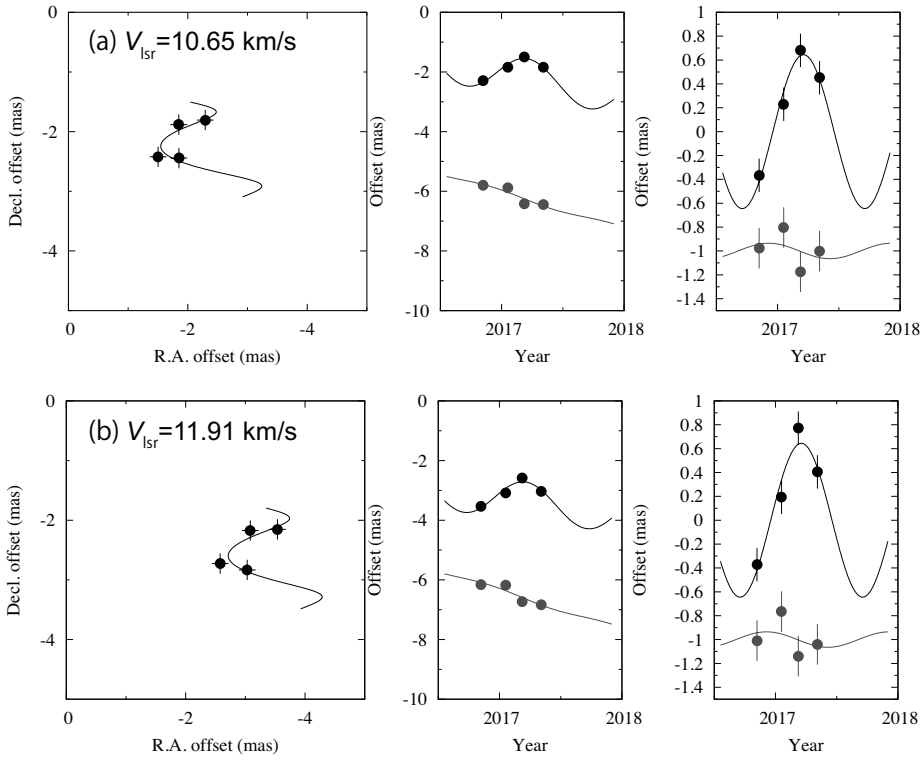

Figure 6.4: The astrometric results of water maser obtained from triangle phase-referencing observations in G000.16-00.44. (a) Results for a maser spot at $V_{\rm lsr} = 10.65\,{\rm km\,s^{-1}}$. (Left) : the position of G000.16-00.44 on the projected sky. (Center) : position of right ascension and declination as a function of time. (Right) : same as the middle but with the linear proper motion subtracted. (b) Similar results for a maser spot at $V_{\rm lsr} = 11.91\,{\rm km\,s^{-1}}$.

out this distance because the projected position of G359.94-0.14 is very close to the center of the CMZ, and because the systematic proper motion is directing along the Galactic plane. The non-circular motion can be calculated by the same manner of discussion on Section 4.5. The obtained non-circular motion is $(U_s, V_s, W_s) = (-15.7 \pm 0.80, -74.7 \pm 20.89, 38.1 \pm 17.89)\,{\rm km\,s^{-1}}$ if we assume the distance of the source as 8 kpc.

Similarly to G359.94-00.14, we calculated the non-circular motion of G000.16-00.44. The systematic proper motion of the source is $(\mu_{\rm RA}, \mu_{\rm Dec}) = (-0.51 \pm 0.13, -0.77 \pm 0.15)\,{\rm mas\,yr^{-1}}$. When the distance $D = 1.55\,{\rm kpc}$, the non-circular motion of the source becomes $(U_s, V_s, W_s) = (11.11 \pm 0.30, 8.49 \pm 1.98, 1.58 \pm 2.31)\,{\rm km\,s^{-1}}$

Here, we compare non-circular motions of G359.94-00.14 and G000.16-00.44 with sources in the Sagittarius arm whose parallaxes and proper motions are measured by VLBI observations (Wu et al. 2014) if we adopt the distance of G359.94-00.14 as 1.83 kpc. Figure 6.6

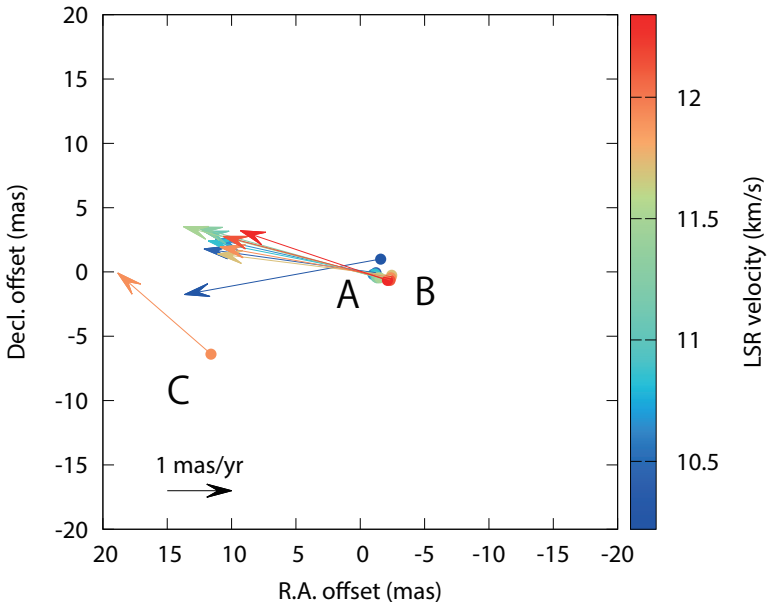

Figure 6.5: Proper motions of maser spots detected for more than three epochsin G000.16-0.44. Colors of arrows represent line-of-sight velocities of maser spots.

shows the noncircular motions of G359.94-00.14 and G000.16-00.44 with motions measured with Wu et al. (2014) as a function of β. Here, β is galactocentric azimuth ($\beta = 0$ deg. is defined toward the Sun and increasing to positive galactic longitude). Small errors of U_s for our sources are attributed to small galactic longitudes of our sources because the values and errors of U_s toward near zero galactic longitude are mostly attributed to those of $V_{\rm lsr}$. For G359.94-0.14, value of U_s and W_s are slightly displaced from other nearby sources within -10 deg. $< \beta <$ 10 deg. while V_s is similar to these sources within errors. Non-circular motion of G000.16-00.44 is similar to these nearby sources. G000.16-00.44 should be located at the Sagittarius spiral arm from the parallax and proper motion measurement. For G359.94-00.14, however, it is necessary to conduct astrometric observations again when the water maser source becomes intense to make conclusion about the distance.

We have to mention how the triangle phase referencing technique is important to conduct the astrometric observations for these sources. Figure 6.7 shows the variation of the flux of the maser spot which we used for the parallax fitting of G000.16-0.44. We can see that the triangle phase referencing technique enables us to detect weak maser spots which cannot be detected by using the inverse phase referencing at the observational epochs of 4 and 7 on Table 6.2. Thus, We could measure the parallax and distinguish this foreground source

Table 6.7: Fitting results of parallax and proper motion for G000.16-00.44 by triangle phase-referencing observations.

Spot	Position offset (mas)		Proper motion ($\mathrm{mas\,yr^{-1}}$)		V_{lsr} ($\mathrm{km\,s^{-1}}$)
	R.A.	Dec.	R.A.		Dec.
A2	-1.97	-1.86	0.35	-1.46	10.44
A3	-1.93	-1.83	-0.76	0.44	10.65
A4	-1.97	-1.84	-0.62	-1.28	10.86
A5	-1.97	-1.88	-0.53	-1.09	11.07
A6	-1.82	-1.88	-0.61	-1.01	11.28
B1	-3.16	-2.11	-0.51	0.44	11.70
B2	-3.15	-2.17	-0.61	-1.11	11.91
B3	-3.17	-2.14	-0.55	-1.32	12.12

in the direction of the Galactic center by using the triangle phase referencing for the first time.

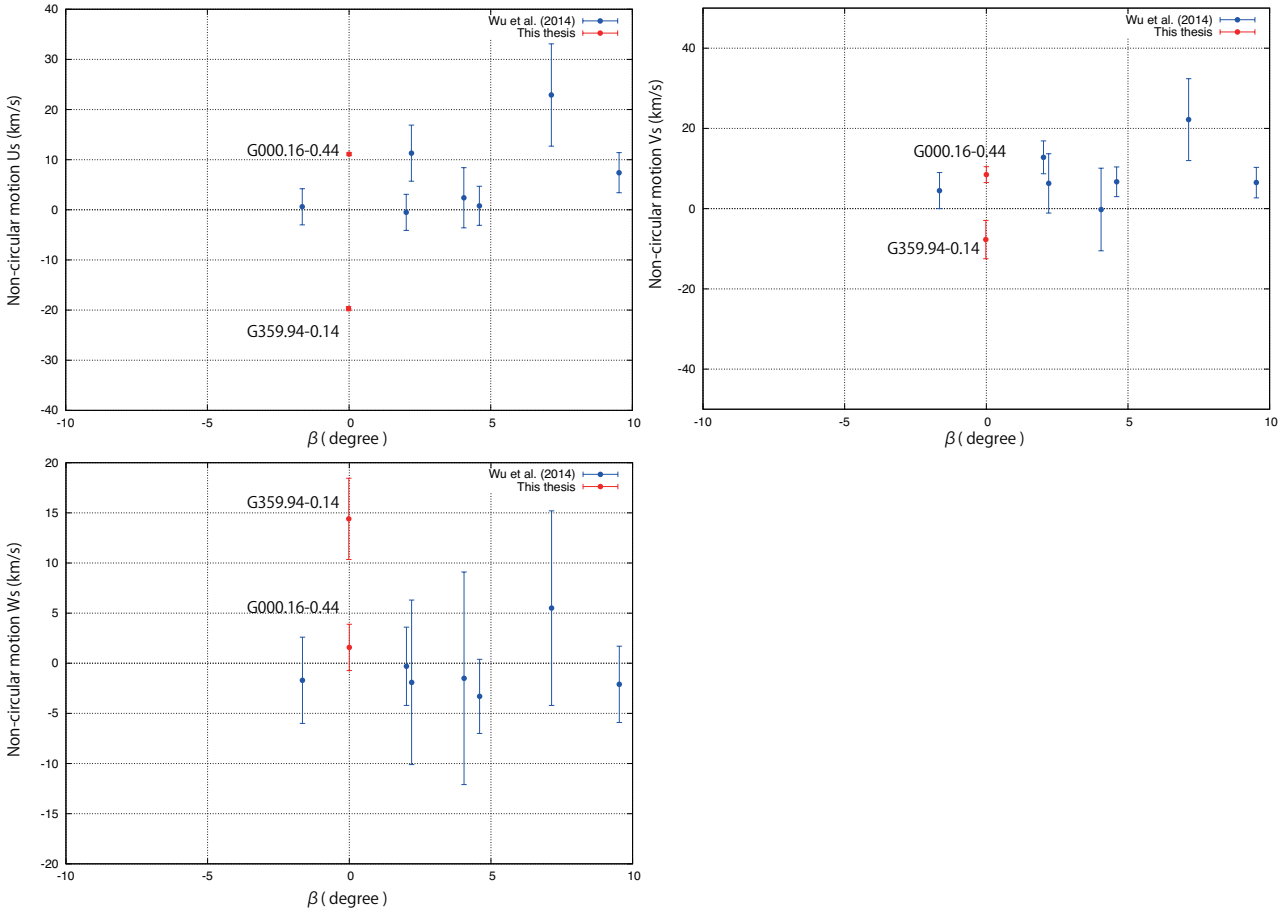

Figure 6.6: Non-circular motions of water maser sources in the Sagittarius spiral arm detected in this thesis (red) and in Wu et al. (2014).

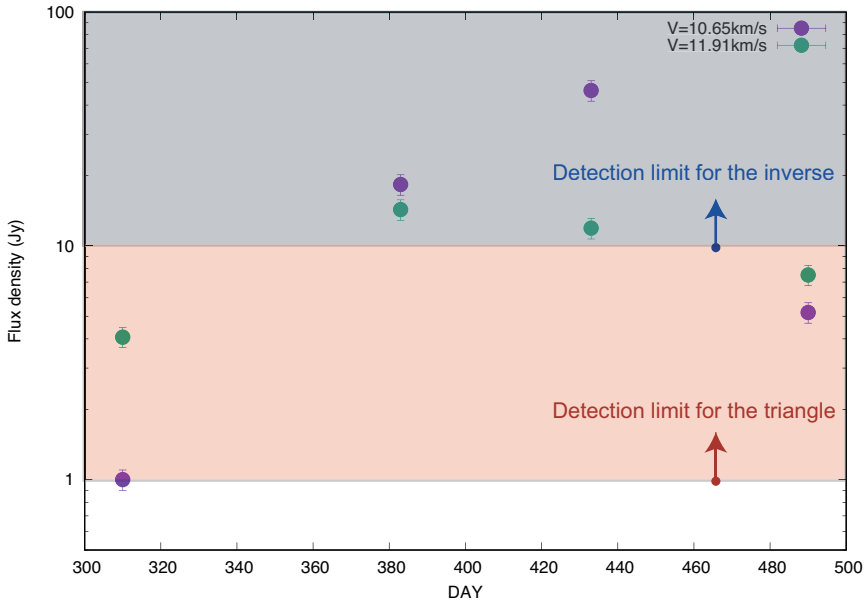

Figure 6.7: Time variation of the flux densities of the maser spots detected at G000.16-0.44. Purple and green filled circle indicate the fluxes for the spot at $V_{\rm lsr} = 10.65\,{\rm km\,s^{-1}}$ and $11.91\,{\rm km\,s^{-1}}$, respectively. The vertical axis is plotted on a logarithmic scale. The blue shadowed area indicates the flux that the inverse phase referencing can detect while the orange area indicates that for the triangle phase referencing.

Chapter 7 Conclusions and future prospects

In this thesis, we present astrometric study of water maser sources toward the Galactic center region with the VLBI Exploration of Radio Astrometry (VERA). The central 300 pc of the Galaxy, which is called as the Central molecular zone (CMZ), has a remarkable non-circular motion compared with the Galactic disk. To explain the origin of the non-circular motion, a number of kinematic models are proposed using spectroscopic observations of interstellar medium. However, most of these models are constructed on line-of-sight velocity observations, and the proper motion measurement with VLBI astrometry can directly constrain these models. As a step before constraining the kinematics of the CMZ, we have to distinguish the foreground sources and the Galactic center sources existing along the same line-of-sight direction by measuring parallaxes and proper motions for a number of maser sources toward the Galactic center.

7.1 Conclusions

7.1.1 Development of the triangle phase referencing technique (Chapter 3)

We developed a new observation technique, the triangle phase referencing observations, which enable us to detect weak maser sources which cannot be detected by the standard phase referencing technique. The triangle phase referencing uses a strong phase reference maser (PRM) in addition to a position reference QSO (PRQ) and a target maser (TM) of which we want to obtain the parallax and proper motion. We conducted test observations of the triangle phase referencing for W3OH region to evaluate the accuracy of astrometric results obtained by this technique. As a result, we obtained the systematic position error in the triangle phase referencing technique of 36 μas. This is smaller than the position error caused by the thermal noise (38–95 μas). Thus, the triangle phase referencing can be applied for the weak sources without significant error increase, which can't use for the normal phase referencing. It makes possible to measure the proper motions and to distinguish between nearby source and the Galactic center source by parallax measurement.

7.1.2 Astrometric observations for the Sgr D and Sgr B2 (Chapter 4 and 5)

We conduct astrometric observations for water maser sources associated with the Sgr D HII region and the Sgr B2 complex, respectively. These two sources have relatively strong flux densities toward the Galactic center region, and the triangle phase referencing is not

required. We obtained the parallax of Sgr D as $\pi = 0.423 \pm 0.083$ mas, corresponding to $d = 2.36^{+0.58}_{-0.39}$ kpc. Our results are the first accurate distance measurement of the Sgr D HII region, suggesting that the Sgr D HII region is located at the foreground of the Galactic center and the Scutum arm of the Galaxy. For the Sgr B2 complex, we measured detailed 3- dimentional motions of water masers associated with Sgr B2M, N, and S in the Sgr B2 complex for the first time. Our results of parallax and proper motions, $\pi = 0.133 \pm 0.038$ mas and $(\mu_l \cos b, \mu_b) = (-3.72 \pm 0.22, -0.49 \pm 0.23)$ mas/yr prefer open-obit model of the CMZ.

7.1.3 Astrometric observations for the Galactic center sources with the triangle phase referencing (Chapter 6)

We conduct the triangle phase referencing observations for weak maser sources toward the Galactic center region. As a phase reference maser (PRM) we used a strong maser spot in Sgr B2M. The target masers are water maser sources associated with G359.94-00.14 and G000.16-00.44. G359.94-00.14 is Young stellar object (YSO) located at very vicinity of Sgr A* in projection, and G000.16-00.44 is a star-forming region. Both of water maser sources are so weak that we cannot detect the maser spot with the standard phase referencing technique. Using the triangle phase-reference, we succeeded to detected masers, and measured their absolute positions. For G000.16-00.44, we measured the parallax and proper motions as $\pi = 0.645 \pm 0.074$ mas, $(\mu_l \cos b, \mu_b) = (-0.51 \pm 0.13, -0.77 \pm 0.15)$ mas/yr, and it suggested that G000.16-00.44 is located at the Sagittarius arm. For G359.94-00.14, unfortunately, the flux of the maser source decreased under the detection limit of the triangle phase referencing (< 1 Jy) after mid 2016, but we could obtain proper motions as $(\mu_{\rm RA}, \mu_{\rm Dec}) = (-1.89 \pm 0.24, -1.54 \pm 0.50)$ mas/yr. Although the statistical parallax suggests that G359.94-00.14 is also located at the Sagittarius arm, the peculiar motion from the Galactic rotation is displaced from that of other sources located at the Sagittarius arm measured by VLBA.

In summary, we obtained parallaxes and proper motions of water maser sources toward the Galactic center with VLBI observations. A new astrometric observation technique which we developed in this thesis successfully detected weak maser sources which we could not detect with the standard phase referencing. Our works in this thesis demonstrate that the future VLBI observations toward the Galactic center enable to constrain the kinematics model of the CMZ.

7.2 Future prospects

In this thesis, we demonstrated that our new observational technique, the triangle phase referencing, can measure the parallax and proper motions of weak maser sources down to

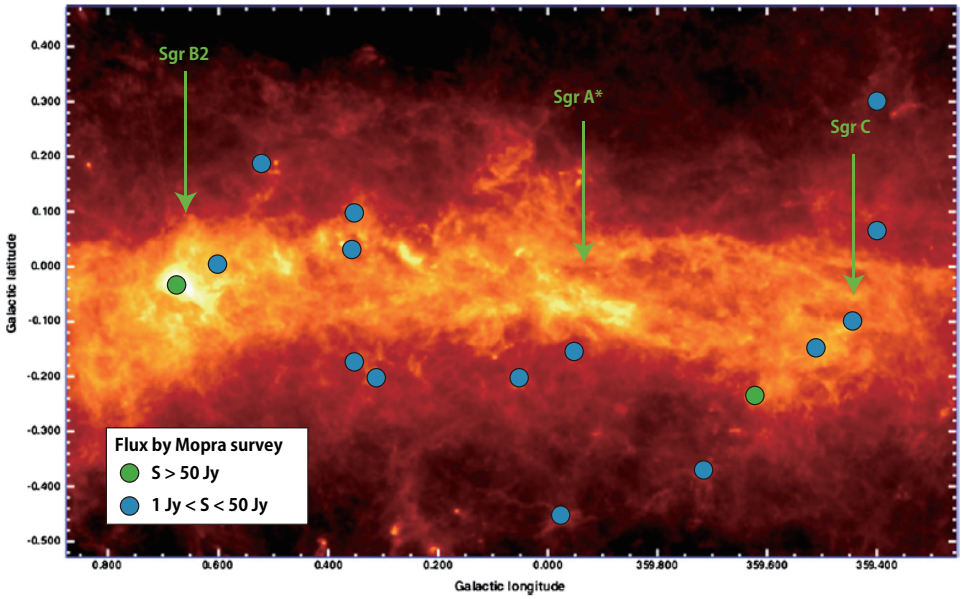

Figure 7.1: The distribution of 22 GHz water maser sources in the Galactic center region superposed on *Herschel* SPIRE 250 μm image (Molinari et al. 2011). Green filled-circle is strong ($S > 50$ Jy), and blue filled-cicle is relatively weak (1 Jy $< S <$ 50 Jy).

about 1 Jy, which could not detect using the normal phase referencing technique. It enabled us to distinguish between the nearby and the Galactic center sources located at the same line-of-sight direction. Figure 7.1 shows the water maser sources which we can detect by using the triangle phase referencing technique from HOPS water maser survey (Walsh et al. 2011). Especially, sources expressed by blue plots in Figure 7.1 have fluxes ranging from 1 Jy to a few tens Jy which is not stably detected until the triangle phase referencing is adopted.

First, we measure the parallaxes and proper motions for these sources, and investigate which sources are actually located at the Galactic center region. A water maser survey conducted with ATCA (Caswell et al. 2011) also detected 27 water maser source down to 0.2 Jy which may be detected using international combined VLBI arrays like East Asia VLBI Network (EAVN) which includes large diameter telescopes up to 65 m. Other maser species associated with star-forming regions like 6.7 GHz methanol maser also can be target sources to constrain the kinematic model of the CMZ.

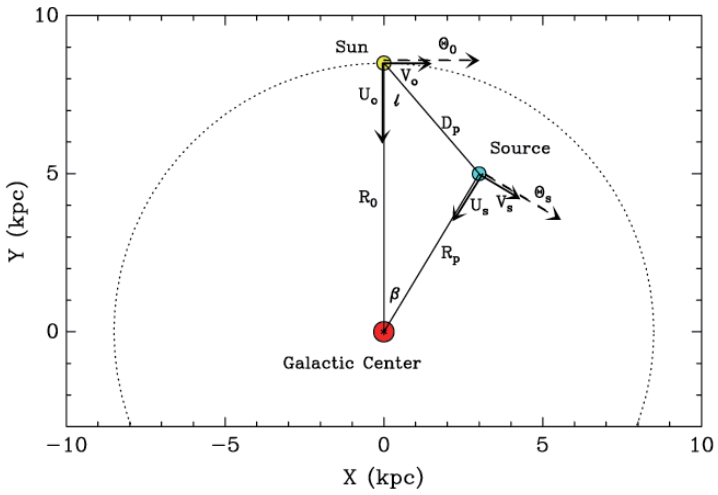

Figure .2: Schematic depiction of Galactic parameters. Figure 8 of Reid et al. (2009)

A The definition of non-circular motions

Through this thesis, we calculated non-circular motions of water maser sources by using proper motions and line-of-sight velocities. Here, we summarize the definition and calculation process of these non-circular motions. This calculation process is followed to appendix of Reid et al. (2009).

As shown in Figure .2, non-circular motions of a source (U_s, V_s, W_s) is defined in a Cartesian Galactocentric frame. U_s is the motion toward the Galactic center from the source, V_s is toward the Galactic rotation, and W_s is toward the north of Galactic pole (toward readers).

From VLBI observations, we can measure proper motions of sources. Then, if we know its distance, or can measure the parallax, we can convert the proper motions in Galactic coordinates (μ_l, μ_b) to linear speeds (v_l, v_b) as

$$v_l = D\mu_l \cos b \quad (.1)$$

$$v_b = D\mu_b, \quad (.2)$$

where D is the distance, and (l, b) is the position of the source in Galactic coordinates. Next, we convert the linear speeds in spherical coordinates to those in Cartesian Galactic coordinates.

$$U_1 = (v_{\rm Helio} \cos b - v_b \sin b) \cos l - v_l \sin l \quad (.3)$$

$$
\begin{aligned}
V_1 &= (v_{\rm Helio}\cos b - v_b \sin b)\sin l + v_l \cos l \\
W_1 &= v_b \cos b + v_{\rm Helio}\sin b. \qquad (.4)
\end{aligned}
$$

$$(.5)$$

$v_{\rm Helio}$ is the heliocentric radial velocity of the source.

Then, the solar motion $(U_\odot, V_\odot, W_\odot)$ and the circular motion of the Galaxy at the Sun Θ_0 is added to (U_1, V_1, W_1).

$$
\begin{aligned}
U_2 &= U_1 + U_\odot \qquad (.6)\\
V_2 &= V_1 + V_\odot + \Theta_0 \\
W_2 &= W_1 + W_\odot. \qquad (.7)
\end{aligned}
$$

Finally, we can obtain non-circular components of the source (U_s, V_s, W_s) by rotating through the angle β and removing circular rotation at the source :

$$
\begin{aligned}
U_s &= U_2 \cos\beta + V_2 \sin\beta \qquad (.8)\\
V_s &= V_2 + \cos\beta + U_2 \sin\beta - \Theta_s \\
W_s &= W_2. \qquad (.9)
\end{aligned}
$$

β is the angle bet ween the Sun and the source increasing to positive galactic longitude.

In this thesis, we used the solar motion $(U_\odot, V_\odot, W_\odot) = (11.1, 12.24, 7.25)\,{\rm km\,s^{-1}}$ and the Galactic constants $(R_0, \Theta_0) = (8.34\,{\rm kpc}, 240\,{\rm km\,s^{-1}})$ (Reid et al. 2014).

Acknowlegement

First of all, I would like to express my deepest gratitude to Dr. Mareki Honma in Mizusawa VLBI Observatory at National Astronomical Observatory of Japan (NAOJ). I have learned a lot of things related with astrophysics as well as important things to become a good researcher. I also express my sincere appreciation to Dr. Hideyuki Kobayashi, my supervisor, who gives sincere comments and supports on my work during the Ph.D. program. I deeply appreciate to Dr. Tomoaki Oyama and Dr. Takumi Nagayama for giving me helpful advises and comments about data reduction of VERA observations. I give my acknowledge to all staff members of Mizusawa VLBI observatory at NAOJ. I thank to the referees of this thesis, Dr. Masato Tsuboi, Dr. Naoteru Gouda, Dr. Kenta Fujisawa, Dr. Ken Ebisawa, and Dr. Hiroshi Imai.

This study was supported by a Grant-in-Aid for Research Fellow from Japan Society for the Promotion of Science (16J01752). I would like to express my gratitude to my colleagues and friends in NAOJ and the University of Tokyo. Finally, I thank my family continuously supporting me through my Ph.D. program.

Bibliography

Anantharamaiah, K. R., & Yusef-Zadeh, F. 1989, The Center of the Galaxy, 136, 159

Anantharamaiah, K. R., Ekers, R. D., Radhakrishnan, V., Cornwell, T. J., & Goss, W. M. 1989, Synthesis Imaging in Radio Astronomy, 6, 431

Bally, J., Stark, A. A., Wilson, R. W., & Henkel, C. 1987, ApJS, 65, 13

Bally, J., Stark, A. A., Wilson, R. W., & Henkel, C. 1988, ApJ, 324, 223

Benson, J. M., & Johnston, K. J. 1984, ApJ, 277, 181

Binney, J., Gerhard, O. E., Stark, A. A., Bally, J., & Uchida, K. I. 1991, MNRAS, 252, 210

Blum, R. D., & Damineli, A. 1999, ApJ, 512, 237

Chuard, D., Terrier, R., Goldwurm, A., et al. 2017, The Multi-Messenger Astrophysics of the Galactic Centre, 322, 208

Contopoulos, G., & Mertzanides, C. 1977, A&A, 61, 477

De Pree, C. G., Peters, T., Mac Low, M.-M., et al. 2014, ApJL, 781, L36

Downes, D., & Maxwell, A. 1966, ApJ, 146, 653

Genzel, R., Reid, M. J., Moran, J. M., & Downes, D. 1981, ApJ, 244, 884

Gillessen, S., Eisenhauer, F., Trippe, S., et al. 2009, ApJ, 692, 1075

Goicoechea, J. R., Rodríguez-Fernández, N. J., & Cernicharo, J. 2004, ApJ, 600, 214

Gordon, M. A., Berkermann, U., Mezger, P. G., et al. 1993, A&A, 280, 208

Güsten, R., & Downes, D. 1980, A& A, 87, 6

Güsten, R. 1989, The Center of the Galaxy, 136, 89

Hasegawa, T., Sato, F., Whiteoak, J. B., & Miyawaki, R. 1994, ApJL, 429, L77

Hirota, T., Bushimata, T., Choi, Y. K., et al. 2007, PASJ, 59, 897

Honma, M., Kijima, M., Suda, H., et al. 2008, PASJ, 60, 935

Honma, M., Nagayama, T., Ando, K., et al. 2012, PASJ, 64,

Imai, H., Sakai, N., Nakanishi, H., et al. 2012, PASJ, 64, 142

Jones, P. A., Burton, M. G., Cunningham, M. R., et al. 2008, MNRAS, 386, 117

Kaifu, N., Kato, T., & Iguchi, T. 1972, Nature Physical Science, 238, 105

Kazes, I., & Aubry, D. 1973, A& A, 22, 413

Kenney, J. D. P., & Lord, S. D. 1991, ApJ, 381, 118

Koyama, K., Hyodo, Y., Inui, T., et al. 2007, PASJ, 59, 245

Kruijssen, J. M. D., Dale, J. E., & Longmore, S. N. 2015, MNRAS, 447, 1059

Kuan, Y.-J., & Snyder, L. E. 1996, ApJ, 470, 981

LaRosa, T. N., Kassim, N. E., Lazio, T. J. W., & Hyman, S. D. 2000, AJ, 119, 207

Launhardt, R., Zylka, R., & Mezger, P. G. 2002, A&A, 384, 112

Lis, D. C. 1991, ApJL, 379, L53

Liszt, H. S. 1992, ApJS, 82, 495

Lindqvist, M., Winnberg, A., Habing, H. J., & Matthews, H. E. 1992, A&AS, 92, 43

McGrath, E. J., Goss, W. M., & De Pree, C. G. 2004, ApJS, 155, 577

Mehringer, D. M., Goss, W. M., Lis, D. C., Palmer, P., & Menten, K. M. 1998, ApJ, 493, 274

Mills, E. A. C., & Morris, M. R. 2013, ApJ, 772, 105

Morris, M., Polish, N., Zuckerman, B., & Kaifu, N. 1983, AJ, 88, 1228

Morris, M., & Serabyn, E. 1996, ARAA, 34, 645

Nobukawa, M., Ryu, S. G., Tsuru, T. G., & Koyama, K. 2011, ApJL, 739, L52

Ponti, G., Terrier, R., Goldwurm, A., Belanger, G., & Trap, G. 2010, ApJ, 714, 732

Reid, M. J., & Brunthaler, A. 2004, ApJ, 616, 872

Reid, M. J., Menten, K. M., Zheng, X. W., et al. 2009, ApJ, 700, 137-148

Reid, M. J., & Honma, M. 2014, Annual Review of Astronomy and Astrophysics, 52, 339

Reid, M. J., Menten, K. M., Brunthaler, A., et al. 2014, ApJ, 783, 130

Rybicki, G. B., & Lightman, A. P. 1979, Astronomy Quarterly, 3, 199

Ryu, S. G., Koyama, K., Nobukawa, M., Fukuoka, R., & Tsuru, T. G. 2009, PASJ, 61, 751

Ryu, S. G., Nobukawa, M., Nakashima, S., et al. 2013, PASJ, 65, 33

Sánchez-Monge, Á., Schilke, P., Schmiedeke, A., et al. 2017, A&A, 604, A6

Sato, M., Wu, Y. W., Immer, K., et al. 2014, ApJ, 793, 72

Sawada, M., Tsujimoto, M., Koyama, K., et al. 2009, PASJ, 61, 209

Schödel, R., Ott, T., Genzel, R., et al. 2002, Nature, 419, 694

Schneps, M. H., Lane, A. P., Downes, D., et al. 1981, ApJ, 249, 124

Schönrich, R., Binney, J., & Dehnen, W. 2010, MNRAS, 403, 1829

Schwarzschild, M. 1979, ApJ, 232, 236

Scoville, N. Z. 1972, ApJL, 175, L127

Shibata, K. M., Kameno, S., Inoue, M., & Kobayashi, H. 1998, IAU Colloq. 164: Radio Emission from Galactic and Extragalactic Compact Sources, 144, 413

Sjouwerman, L. O., Lindqvist, M., van Langevelde, H. J., & Diamond, P. J. 2002, A&A, 391, 967

Sofue, Y. 1995, PASJ, 47, 551

Su, M., Slatyer, T. R., & Finkbeiner, D. P. 2010, ApJ, 724, 1044

Terrier, R., Ponti, G., Bélanger, G., et al. 2010, ApJ, 719, 143

Thompson, A. R., Moran, J. M., & Swenson, G. W., Jr. 2017, Interferometry and Synthesis in Radio Astronomy, by A. Richard Thompson, James M. Moran, and George W. Swenson, Jr. 3rd ed. Springer, 2017.,

Tsuboi, M., Handa, T., Inoue, M., Inatani, J., & Ukita, N. 1989, The Center of the Galaxy, 136, 135

Tsuboi, M., Handa, T., & Ukita, N. 1999, ApJS, 120, 1

Whiteoak, J. B., & Gardner, F. F. 1974, A& A, 37, 389

Wilson, T. L., Ruf, K., Walmsley, C. M., et al. 1982, A& A, 115, 185

Wu, Y. W., Sato, M., Reid, M. J., et al. 2014, A&A, 566, A17

Yusef-Zadeh, F. 2003, ApJ, 598, 325